Precision mass measurements on neutron-rich Zn isotopes and their consequences on the astrophysical r-process

Inaguraldissertation
zur
Erlangung des akademischen Grades
doctor rerum naturalium (Dr. rer. nat.)
an der Mathematisch-Naturwissenschaftlichen Fakultät
der
Ernst-Moritz-Arndt-Universität Greifswald

vorgelegt von

Sudarshan Baruah

geboren 1. Feb. 1980
in Darrang, Indien

Greifswald, July 2008

Dekan: Prof. Dr. K. Fesser

1. Gutachter: Prof. Dr. L. Schweikhard

2. Gutachter: Prof. Dr. G. Werth

Tag der Promotion: 17.10.2008

Abstract

The rapid neutron-capture or the r-process is responsible for the origin of about half of the neutron-rich atomic nuclei in the universe heavier than iron. For the calculation of the abundances of those nuclei, atomic masses are required as one of the input parameters with very high precision. In the present work, the masses of the neutron-rich Zn isotopes ($A = 71$ to 81) lying in the r-process path have been measured in the ISOLTRAP experiment at ISOLDE/CERN. The mass of ^{81}Zn has been measured directly for the first time. The half-lives of the nuclides ranged from 46.5 h (^{72}Zn) down to 290 ms (^{81}Zn). In case of all the nuclides, the relative mass uncertainty ($\Delta m/m$) achieved was in the order of 10^{-8} corresponding to a 100-fold improvement in precision over previous measurements.

Contents

Abstract **v**

1 Introduction **1**

2 The r-process in nucleosynthesis and precision mass measurements **3**

2.1 Nucleosynthesis 3

2.2 The r-process 9

2.2.1 Introduction 9

2.2.2 Theory of the classical r-process 10

2.2.3 Need for experimental data for r-process calculation 15

3 Trapping of charged particles: The Penning trap **19**

3.1 Types of ion traps 19

3.2 Equations of motion of a charged particle in a Penning trap 20

3.3 Manipulation of ion motion 23

3.3.1 Dipolar excitation 23

3.3.2 Quadrupolar excitation 26

3.3.3 Time-of-flight cyclotron resonance 28

3.3.4 Cooling of trapped ions 30

4 The ISOLTRAP experiment **33**

4.1 The online isotope separator ISOLDE 33

4.2 The ISOLTRAP setup 34

4.2.1 The reference ion-source 35

4.2.2 The RFQ cooler and buncher 36

4.2.3 The carbon cluster ion source 37

4.2.4 The Preparation Penning trap 37

4.2.5 The Precision Penning trap 39

5 Simulation of octupolar excitation 43
5.1 Simulation of the octupolar excitation 44
5.2 Results and discussion 45
5.2.1 Influence of octupolar excitation on the ion motion 45
5.2.2 Octupolar resonance profile 48
5.2.3 Line-shape and FWHM of the resonance profile 52
5.3 Outlook 53

6 Mass measurements of neutron-rich Zn isotopes 55
6.1 Production of the Zn isotopes 55
6.2 The method for data analysis 58
6.2.1 Atomic Mass Evaluation 58
6.2.2 Data analysis procedure 59
6.3 Results and discussion 62
6.3.1 Mass measurements on the n-rich Zn nuclides 63
6.3.2 Final results of the evaluation 70
6.3.3 Discussion of the results 71

7 Conclusion and outlook 75

A Calculation of confidence band for linear regression 77

B Cyclotron resonances of the Zn nuclides (^{71}Zn to ^{81}Zn) 83

Bibliography 91

List of Figures

2.1 The neutron-capture processes of nucleosynthesis starting from the seed nuclide ^{56}Fe 5
2.2 Flow of the p-process nuclei through photodisintegration reactions interspersed with β^{+}-emission 7
2.3 Path of the rp-process in a section of the nuclear chart 8
2.4 Schematic diagram of the rapid neutron-capture process. 10
2.5 Comparison of the observed solar r-abundances with the predictions from the classical r-process model. 14
2.6 Comparison of the neutron shell gap values (Δ_n) calculated from different mass models at $N_0 = 50$. 16

3.1 Typical geometry of Paul and Penning traps. 20
3.2 The motion of a charged particle in a Penning trap. 22
3.3 Electrode geometry for dipolar, quadrupolar and octupolar excitation. . 23
3.4 Evolution of the cyclotron and the magnetron radii of an ion as a function of time under the dipolar excitation 25
3.5 Conversion between the two radial motions under the quadrupolar excitation. 27
3.6 Theoretical line-shape of a time-of-flight cyclotron resonance for a Fourier-limited quadrupolar excitation signal. 29
3.7 Trajectory of an ion under quadrupolar excitation in presence of a buffer gas. 30

4.1 Sketch of the experiment-hall of the ISOLDE facility. 34
4.2 Sketch of the ISOLTRAP setup. 35
4.3 Sketch of the ion beam cooler and buncher. 36
4.4 Sketch of the cooler Penning trap. 38

4.5 Sketch of the Precision Penning trap. 39
4.6 The spatial variation of the magnetic field between the Precision trap and the Channeltron detector. 40
4.7 The ion TOF signal for $^{85}Rb^+$ and the corresponding resonance with a fit. 41

5.1 Configuration of the eight segments of the ring electrode for applying octupolar excitation. 45
5.2 Evolution of the magnetron and the cyclotron radii as a function of time for the octupolar excitation. 46
5.3 The beat frequency and the initial magnetron radius. 47
5.4 Cyclotron radius r_+ as a function of the frequency ν_{rf} and the phase ϕ_{rf} of the excitation field. 48
5.5 Cyclotron radius as a function of the excitation frequency averaged over the rf phases. 49
5.6 Cyclotron radius as a function of the detuning from $2\nu_c$ for different excitation times. 51
5.7 Contor plot of the cyclotron radius r_+ as a function of the frequency ν_{exc} and the phase ϕ_{exc} of the excitation. 52

6.1 Excitation scheme for resonant laser ionization of Zn. 56
6.2 Yields (filled symbols) and estimated in-target production rates (open symbols) of Zn and Ga isotopes. 57
6.3 Histogram showing the number of events (y_j) with respect to the corresponding ion counts (x_j). 60
6.4 A typical time-of-flight cyclotron resonance curve for ^{76}Zn$^+$. 61
6.5 Comparison of the measured mass-excess values with the AME 2003 values. 65
6.6 Mass-excess values of ^{73}Zn from AME2003 and from ISOLTRAP measurement in comparison to those predicted by different mass models. . . 66
6.7 Comparison of mass-excess values from previous measurements with the ISOLTRAP result for ^{75}Zn. 67
6.8 Comparison of the mass-excess values of $^{71-81}Zn$ nuclides measured at ISOLTRAP with those predicted by different mass models. 71
6.9 Comparison of the two-neutron separation energies of the Zn isotopes with the AME values 73

A.1 Probability density curve of t distribution. 79

A.2 Confidence band for linear regression. 81

B.1 - B.7 Cyclotron resonances of the Zn nuclides with fits. 84

List of Tables

6.1 The cyclotron frequency ratios of the reference nuclide and the investigated nuclides . . . 63

6.2 Mass-excess values of the nuclides $^{71-81}Zn$. . . . 70

List of Symbols

A	Atomic mass number
a_d, a_q, a_o	Correction factors for the dipolar, quadrupolar and octupolar excitations, respectively
B	Magnetic field strength
$B(N,Z)$	Binding energy of the nucleus (N,Z)
Δ_n	Neutron shell-gap energy
E	Electric field strength
$G(A,Z)$	Partition function of (A,Z)
m	Atomic mass
$\mu_{y\|x}$	Mean response of linear regression at x
$n(A,Z)$	Abundance of nuclide (A,Z)
$n(Z)$	Elemental abundance
N	Number of neutrons
N_0	Magic number
n_n	Neutron number density
ν_c	Cyclotron frequency
ν_-	Magnetron frequency
ν_+	Reduced cyclotron frequency
ν_{rf}	Frequency of rf excitation
ϕ_{rf}	Phase of rf excitation
q	Electronic charge
r_0	Minimum distance between the trap center and the ring electrode of the Penning trap
r_-	Magnetron radius
r_+	Cyclotron radius

s	Standard deviation of linear regression
S	Sample standard deviation
S_n	Neutron separation energy
S_{2n}	Two-neutron separation energy
ψ	Degrees of freedom
σ	Uncertainty
$T_{1/2}$	Half-life of a radionuclide
T_{rf}	Time of rf excitation
τ	Neutron irradiation time in r-process
τ_n	Neutron capture time
τ_β	β-decay life-time
u	Atomic mass unit
U_0	Trapping potential
U_d, U_q, U_o	Amplitude of dipolar, quadrupolar and octupolar excitations
V_0	Amplitude of excitation potential
Z	Number of protons
z_0	Minimum distance between the trap center and the endcap

Chapter 1

Introduction

The binding energy of the nucleus is very small compared to the mass equivalent of the whole nucleus. So, only precise measurement of nuclear mass can give information about the binding energies of the nuclides. There are both direct and indirect techniques, one can resort to. Indirect techniques are mainly based on the determination of the Q-value of nuclear reactions. But the measurements to determine the Q-value of long decay chains give rise to huge systematic errors. In addition, one needs to know the nuclear level schemes of the parent nucleus as well as all the daughter nuclei of the decay chain to calculate Q. Direct techniques, on the other hand, are based on time-of-flight measurement through magnetic spectrometer (SPEG at GANIL [Bianchi1989]) or cyclotron frequency determination using a Penning trap (ISOLTRAP at ISOLDE [Bollen2001], Canadian Penning Trap (CPT) at Argonne [Savard2001], JYFLTRAP in Jyväskylä [Kolhinen2004], LEBIT at Michigan State University [Bollen2004], TITAN at TRIUMF at Vancouver [Dilling2003]), storage ring (ESR at GSI [Radon2000]) or RF spectrometer (MISTRAL at ISOLDE [Lunney2000]) [Schweikhard2006]. Among all these methods, the highest accuracy in mass measurement of short-lived nuclides is achieved with the cyclotron-frequency determination technique [Blaum2006].

The ISOLTRAP experiment [Bollen2001] at present has a maximum resolving power of 10^7, and mass measurements can be performed with a relative uncertainty as low as 1×10^{-8}. Masses of more than 200 radionuclides have been measured at ISOLTRAP so far since its installation in the late 1980s. Major technical improvements of the setup in the recent years have enabled to access a wide range of nuclei for mass measurement [Blaum2003, Herlert2006]. Radionuclides with a half-life as short as 65 ms (^{74}Rb) have been investigated[Herfurth2002].

The main part of this work consists of the mass measurements on the Zn nuclides from $A = 71$ to 81, which range in half-lives from 46.5 h (^{72}Zn) down to 290 ms (^{81}Zn). A huge improvement of the accuracy of the mass values has been achieved as compared to the present literature values [Audi2003]. The result of the measurement is of particular importance for nuclear astrophysics as ^{80}Zn is one of the three most important *waiting-point* nuclides of the r-process path [Cowan1991].

An overview of the r-process nucleosynthesis is given in Chapter 2. Chapter 3 gives an introduction to the techniques of trapping of charged particles followed by the experimental setup and mass measurement principle at ISOLTRAP in Chapter 4. Chapter 5 gives an account of the analytical simulation on a new excitation technique which can improve the resolving power in the mass measurement. The procedures and results of the mass measurement on the neutron-rich Zn isotopes are described in Chapter 6.

Chapter 2

The r-process in nucleosynthesis and precision mass measurements

The study of the neutron-rich (*n*-rich) nuclei has drawn increasing attention because of the interest in understanding of the synthesis of the nuclides heavier than Fe [Burbidge1957, Sneden2003]. Two distinct neutron-capture processes are attributed to the production of those nuclides in the universe - one at a high neutron density and the other at a low neutron density. The first type of neutron capture takes place on a short time-scale compared to the competitive β-decay, and hence it is known as the *rapid* process or the r-process. The other type of neutron capture occurs on a longer time-scale in comparison to the time-scale of the competitive β-decay and is known as the *slow* process or the s-process.

The calculation of the neutron-capture processes demands, among other data, precise mass values of the nuclides involved. Of special importance are the mass values of the so-called *waiting-point* nuclides. To this end, the mass of ^{80}Zn, which is one among the three most important waiting-point nuclides of the r-process- ^{80}Zn, ^{130}Cd and ^{195}Tm, has been measured at ISOLTRAP/CERN. The theory and the main points of the r-process nucleosynthesis will be described in this chapter.

2.1 Nucleosynthesis

The production of elements in the nuclear fusion processes in stars is limited to those upto iron. ^{56}Fe has a binding energy per nucleon of 8790.36(3) keV [Fewell1995]. The binding energy per nucleon decreases with increasing A for nuclides beyond Fe[i]. The group of these elements with high binding energy around mass number $A = 60$ is typically called *the iron group* elements in astrophysics [Lang1999]. Since the binding energy per nucleon decreases with increasing A for nuclides beyond $A \approx 60$, they are not likely to be formed by fusion processes. The heavier nuclides with $A \geq 60$ are formed from the nucleons (protons and neutrons) and the pre-existing nuclides via certain processes, which were identified by Burbidge *et al.* [Burbidge1957] and Cameron [Cameron1957] independently in 1957. Those were: the slow neutron-capture or s-process, the rapid neutron-capture or r-process and the proton or p-process. In 1981, Wallace *et al.* proposed another nucleosynthesis process which was termed the rapid proton-capture or rp-process [Wallace1981] in analogy with the rapid neutron-capture process. Among these four processes, only the s-process occurs in a normal stellar environment, while the other three processes occur in an explosive environment such as a supernova explosion.

In a neutron-capture or (n, γ) process, a nuclide ${}^{A}_{Z}X$ of an element X is transformed into a more massive nuclide by successive capture of neutrons,

$$ {}^{A}_{Z}X + n \rightarrow^{A+1}_{Z} X + \gamma, \tag{2.1}$$

along an isotopic chain until it is hindered by photodisintegration (γ, n) reaction:

$$ {}^{A}_{Z}X + \gamma \rightarrow^{A-1}_{Z} X + n. \tag{2.2}$$

The heaviest nucleus formed by the neutron-capture process before the process is hindered can undergo a β-decay and produce another nuclide with a higher Z:

$$ {}^{A+1}_{Z}X \rightarrow^{A+1}_{Z+1} Y + e^{-} + \bar{\nu}. \tag{2.3}$$

The nucleus ${}^{A+1}_{Z+1}Y$ can continue capturing neutrons again and thus the process goes on. Out of the two neutron-capture processes, the slow neutron-capture or s-process occurs at comparatively lower neutron density ($n_n \approx 10^8$ cm^{-3}) and lower temperature ($T \approx 3 - 4 \times 10^8$ K) [Käppeler1989]. In this case, the life-time for β-decay τ_β is shorter than the competing neutron capture time τ_n ($\approx$ 100 - 1000 years), *i.e.*, $\tau_\beta \leq \tau_n$. This prevents the s-process from capturing more neutrons before undergoing β-decay. That is why the s-process produces nuclei by following a path along the bottom of the valley of stability. On the other hand, the r-process takes place in a high neutron density ($n_n \approx 10^{20} - 10^{25}$ cm^{-3}) and high temperature ($T \approx 1 - 3 \times 10^9$ K) [Norman1979] environment. In this case, the life-time for β-decay τ_β is higher than the neutron capture time τ_n ($\approx$ 0.01 - 0.1 s), *i.e.*, $\tau_\beta >> \tau_n$. This allows the r-process to go on capturing neutrons along an isotopic chain before finally undergoing a β-decay at a highly neutron-rich nuclide. Hence, the process produces very neutron rich and unstable nuclei which are far off the valley of β-stability.

---

[i] The nuclide ^{62}Ni has the highest binding energy per nucleon followed by ^{58}Fe and ^{56}Fe [Fewell1995]. However, the abundance of ^{56}Fe is an order of magnitude higher than that of ^{62}Ni because of the greater photodisintegration rate for ^{62}Ni in stellar interiors [Fewell1995].

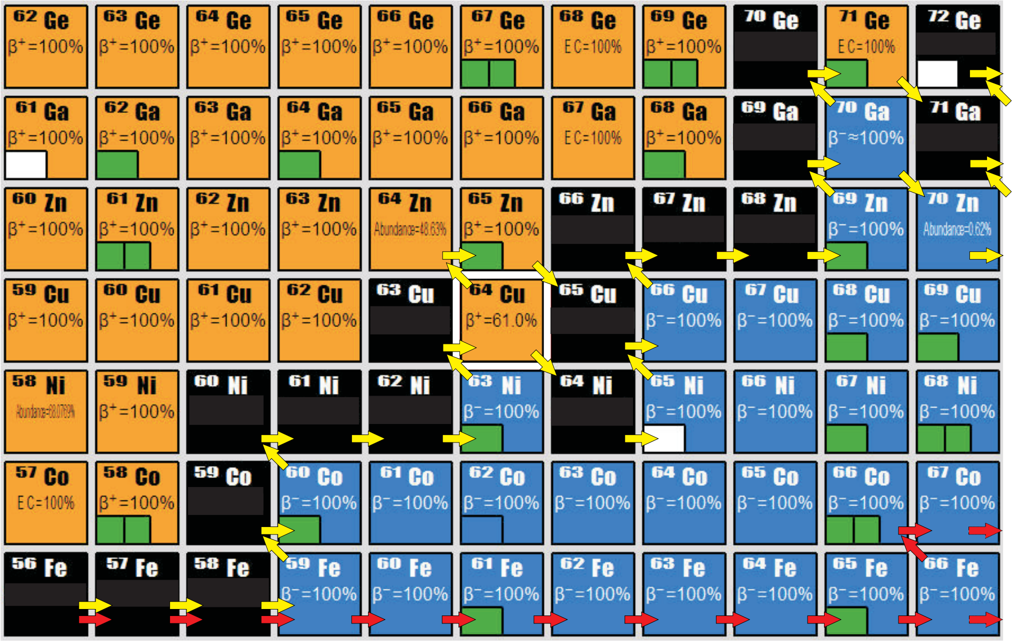

62 Ge β+=100%	63 Ge β+=100%	64 Ge β+=100%	65 Ge β+=100%	66 Ge β+=100%	67 Ge β+=100%	68 Ge EC=100%	69 Ge β+=100%	70 Ge	71 Ge EC=100%	72 Ge
61 Ga β+=100%	62 Ga β+=100%	63 Ga β+=100%	64 Ga β+=100%	65 Ga β+=100%	66 Ga β+=100%	67 Ga EC=100%	68 Ga β+=100%	69 Ga	70 Ga β−≈100%	71 Ga
60 Zn β+=100%	61 Zn β+=100%	62 Zn β+=100%	63 Zn β+=100%	64 Zn Abundance=48.63%	65 Zn β+=100%	66 Zn	67 Zn	68 Zn	69 Zn β−=100%	70 Zn Abundance=0.62%
59 Cu β+=100%	60 Cu β+=100%	61 Cu β+=100%	62 Cu β+=100%	63 Cu	64 Cu β+=61.0%	65 Cu	66 Cu β−=100%	67 Cu β−=100%	68 Cu β−=100%	69 Cu β−=100%
58 Ni Abundance=68.0769%	59 Ni β+=100%	60 Ni	61 Ni	62 Ni	63 Ni β−=100%	64 Ni	65 Ni β−=100%	66 Ni β−=100%	67 Ni β−=100%	68 Ni β−=100%
57 Co EC=100%	58 Co β+=100%	59 Co	60 Co β−=100%	61 Co β−=100%	62 Co β−=100%	63 Co β−=100%	64 Co β−=100%	65 Co β−=100%	66 Co β−=100%	67 Co β−=100%
56 Fe	57 Fe	58 Fe	59 Fe β−=100%	60 Fe β−=100%	61 Fe β−=100%	62 Fe β−=100%	63 Fe β−=100%	64 Fe β−=100%	65 Fe β−=100%	66 Fe β−=100%

Figure 2.1: The neutron-capture processes of nucleosynthesis starting from the seed nuclide ^{56}Fe. The s-process follows a path along the bottom of the valley of β-stability as shown by the yellow arrows. The r-process, on the other hand, extends to the very neutron-rich region far away from the valley of β-stability as indicated by the red arrows [Basdevant2005].

Figure 2.1 illustrates how the s- and r-processes evolve from the progenitor, called the *seed nuclide*, ^{56}Fe and produces different nuclides. The stable nuclide ^{56}Fe goes on capturing neutrons and produces the β-unstable nucleus ^{59}Fe ($T_{1/2} = 44.5$ days) when the process can evolve in either *slow* fashion or the *rapid* fashion depending on whether

$\tau_n \geq \tau_\beta$ or $\tau_n << \tau_\beta$, respectively as explained above.

The other two nucleosynthesis processes, namely, the p- and the rp-processes, account for the production of the proton-rich nuclides in the universe. Cameron [Cameron1957] and Burbidge *et al.* [Burbidge1957] proposed a combination of (p, γ), and (γ, n) reactions as the mechanism of the p-process nucleosynthesis which operate on the nuclides already produced by the r- and s-processes. The term p-process indicates the proton-capture reaction (p, γ) involved:

$$^{A}_{Z}X + p \rightarrow ^{A+1}_{Z+1} Y + \gamma. \tag{2.4}$$

The nuclei produced by this process are collectively known as the p-process nuclei or the p-nuclei. There are about 30 p-nuclei. They are the isotopes from ^{74}Se to ^{196}Hg, which are bypassed by the neutron-capture processes (s- and r-processes) and are located on the proton-rich side of the valley of β-stability in the nuclear chart [Lambert1992].

It was later proposed that the proton-capture reaction is not likely to occur for the production of these nuclei [Woosley1978, Meyer1994]. Instead, a series of photodisintegration reactions - (γ, n), (γ, p) and (γ, α) were proposed for the production of these nuclei [Woosley1978].

The stable elements produced by the r- and s- processes undergo (γ, n) reaction:

$$^{A}_{Z}X + \gamma \rightarrow ^{A-1}_{Z} X + n. \tag{2.5}$$

Once the nuclei become sufficiently proton-rich after successive (γ, n) reactions, they undergo proton or α-particle emission depending on whether they are odd nuclei or even nuclei, respectively [Woosley1978]:

$$^{A}_{Z}X + \gamma \rightarrow ^{A-1}_{Z-1} Y + p \tag{2.6}$$

and

$$^{A}_{Z}X + \gamma \rightarrow ^{A-4}_{Z-2} Y + \alpha. \tag{2.7}$$

The flow of nuclei climbing down toward iron in this process is shown in Fig. 2.2. For nuclei with a closed neutron or proton shell near the end of the isotopic chains, the photodisintegration life-time is unusually long favoring positron (β^+)-emission. The positron emission from these nuclei result in the build-up of the p-nuclei.

As evident from above, although the process for the synthesis of the p-nuclei, termed as the γ-process by Woosley and Howard [Woosley1978], involves only photodisintegration reactions, the process is still generally known as the p-process for historical reasons.

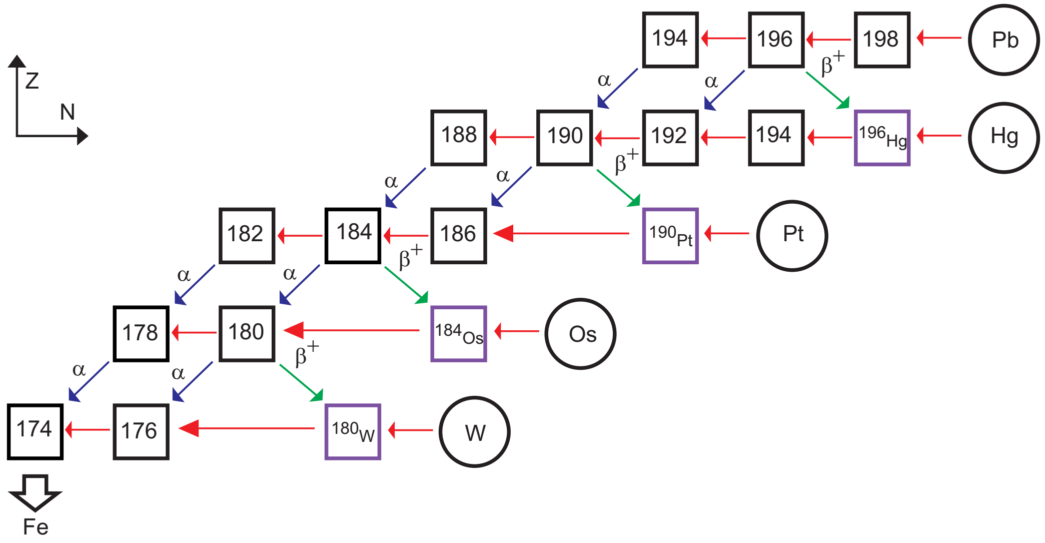

Figure 2.2: Flow of the p-process nuclei through photodisintegration reactions interspersed with β^+-emission. The flow can be compared to a stream with several tributaries, each having a different source (seed nucleus). The circles represent all the stable isotopes of the given element, and the squares in violet represent the p-nuclei. The red, dark blue and green arrows indicate the (γ, n), (γ, α) and β^+-emission processes, respectively. (Figure adopted from [Woosley1978].)

Like the p-process, the rp-process also occurs on the proton-rich side of the valley of β-stability. The process goes on by a series of rapid proton-captures (p, γ) onto a progenitor nuclide producing heavier nuclides in an isotonic chain as shown in Eq. (2.4), until it is hindered by photodisintegration. The nuclide then undergoes a β^+-decay:

$$ {}^A_Z X \rightarrow {}^A_{Z-1} Y + e^+ + \nu \tag{2.8}$$

to come to a isotonic chain with higher N before continuing proton-capture again to produce still heavier nuclides as shown in Fig. 2.3. The progenitors in the process, (*i.e., the seed nuclei*) are believed to be formed in the hot CNO cycle [Schatz1998, Wallace1981].

The rp-process requires a high-temperature ($T \approx 10^9$ K) and hydrogen-rich environment. Low-mass black holes and neutron stars have been suggested as the possible sites for the process. The rp-process can produce heavy nuclides up to and beyond the Fe group. Alpha-decay puts an upper limit on the end point of the rp-process at ^{105}Te, as ^{105}Te is the lightest nucleus to undergo α-decay. Recent works have reported that the process cannot go beyond Te in the neutron stars [Schatz2001].

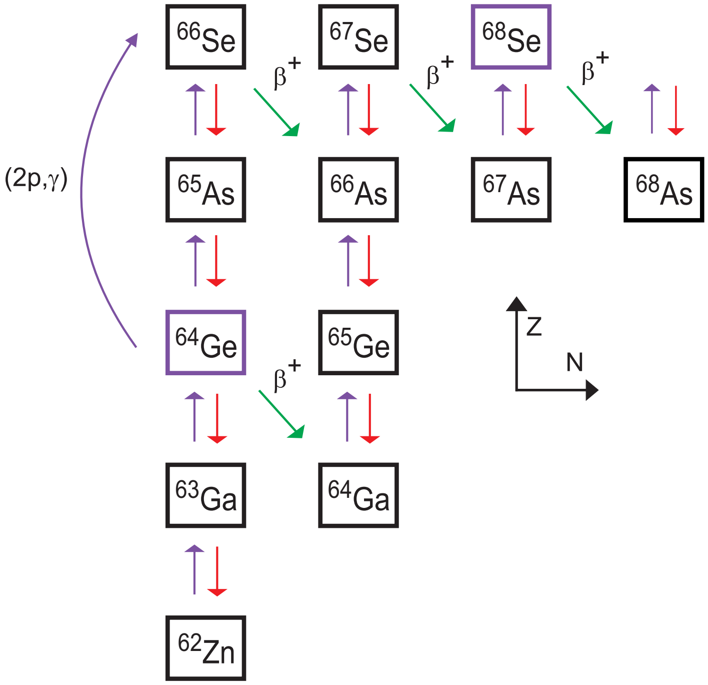

Figure 2.3: Path of the rp-process in a section of the nuclear chart. The violet, red and green arrows indicate the proton-capture (p, γ), photodisintegration (γ, p) and β^+-decay processes, respectively. The violet squares represent the *waiting points*, where the capture process halts momentarily, as the rates of the proton capture and the photodisintegration reactions become comparable. Such a nucleus then either captures two protons successively or decays by β^+-emission depending on the reaction environment. The resulting nucleus will again continue proton-capture until it is hindered by photodisintegration [Clark2005, Schatz1998].

Among the nucleosynthesis processes explained above, only the s-process occur in the stellar environment. The other 3 processes take place in the explosive environment.

In the following section, the main points of the theory of the r-process will be discussed.

2.2 The r-process

2.2.1 Introduction

The model of the r-process, proposed by Burbidge *et al.* [Burbidge1957], is referred to as the *classical* r-process. It is the simplest and most widely used model of the r-process. According to this scenario, production of heavy nuclides via neutron-capture depends on the following mechanisms: (n, γ) and (γ, n) reactions, β^--decay, and neutron-induced fission. It proposes that in presence of high neutron flux and at high temperature, heavy nuclides can be formed via successive neutron-capture (n, γ) process by pre-existing nuclides until the capture process is stopped by the counteracting photodisintegration (γ, n) reaction, when the nuclide may undergo β^--decay before it continues capturing neutrons again.

The classical r-process model is based on the following assumptions:
(1) the neutron density n_n is high enough ($n_n \approx 10^{20} - 10^{25}$ cm^{-3}) so that the rates of the (n, γ) reactions overcome the β^--decay rates of the corresponding nuclides;
(2) the temperature T is high enough ($T \approx 1 - 3 \times 10^9$ K) so that the rates of the (γ, n) reactions overcome the β^--decay rates of the corresponding nuclides;
(3) both n_n and T remain constant throughout the process;
(4) initially pure ^{56}Fe is irradiated with the neutron flux;
(5) the equilibrium condition $(n, \gamma) \rightleftharpoons (\gamma, n)$ is attained in each isotopic chain;
(6) the neutron flux is available for a very short duration τ (*e.g.*, 10 s for type II supernova), after which the neutron capture reactions cease abruptly (referred to as the *freeze-out* [Qian2003]). At the end of the irradiation, the nuclides produced will undergo β-decay toward the bottom of the valley of β-stability.

The process is illustrated schematically in Fig. 2.4. Under the assumption of $(n, \gamma) \rightleftharpoons (\gamma, n)$, the nucleus (A, Z) goes on capturing neutrons competing over the photodisintegration reaction (γ, n) until the reaction rates become comparable. The capture process then *waits* for a β^--decay after which the nuclide starts capturing neutrons again. This assumption is commonly known as the *waiting-point approximation* of the classical r-process, and the nuclide at which the process waits is called the *waiting-point* nuclide.

Another model of the r-process, called the *dynamical* r-process, does not consider temperature and neutron density as constants [Cowan1983]. In this model, the $(n,\gamma) \rightleftharpoons (\gamma,n)$ equilibrium is not assumed. The neutron-capture rate is calculated for each nucleus as a function of the varying temperature, number density of the nucleus and neutron number density. If the neutron-capture rate at a certain temperature is higher than the β-decay rate, then a neutron-capture will take place. Otherwise, the nucleus will undergo a β-decay. In the following description, only the classical r-process theory will be considered.

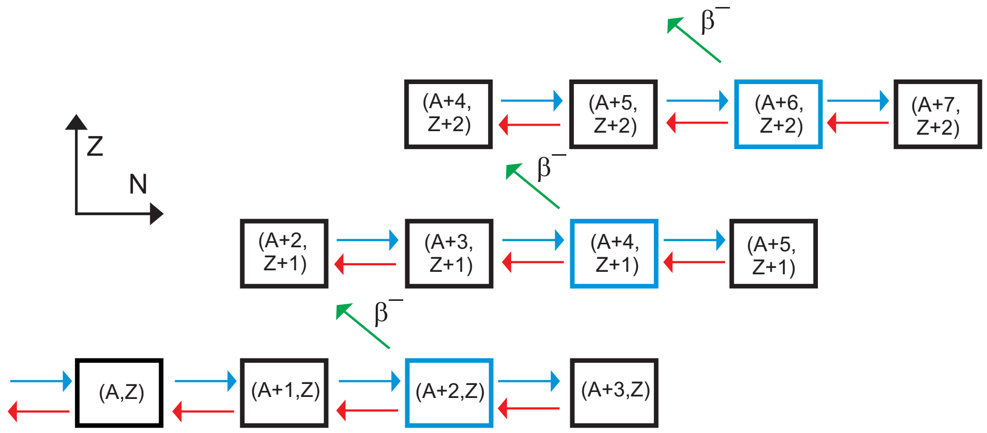

Figure 2.4: Schematic diagram of the rapid neutron-capture process (r-process). The blue, red and green arrows indicate the neutron-capture (n,γ), photodisintegration (γ,n) and β^--decay processes, respectively. The blue squares represent the waiting-point nuclei of the r-process.

2.2.2 Theory of the classical r-process

The general theory of the classical r-process can be described by the (n,γ), (γ,n) and β^--decay reactions for nuclides with $A < 260$[ii]. According to this theory, ^{56}Fe seed nuclei are subjected to a neutron irradiation for a duration of $t = \tau$, and both the neutron density n_n and the temperature T remain constant during the irradiation time.

[ii] The probability of β-delayed fission is 100% for the nuclei with mass numbers $A \approx 260$, which leads to the termination of the r-process beyond $A \approx 260$ [Panov2005, Thielemann1983].

In addition, the temperature has to be high enough for a $(n,\gamma) \rightleftharpoons (\gamma,n)$ equilibrium to be established for each isotopic chain.

Neglecting fission, the derivative of the abundance $n(A,Z)$ of the nuclide (A,Z) undergoing the r-process can be written as [Burbidge1957]

$$\begin{aligned}\frac{d}{dt}\,n(A,Z) &= \lambda_n(A-1,Z)\,n(A-1,Z) - \lambda_n(A,Z)\,n(A,Z)\\ &\quad+\lambda_\beta(A,Z-1)\,n(A,Z-1) - \lambda_\beta(A,Z)\,n(A,Z)\\ &\quad+\lambda_\gamma(A+1,Z)\,n(A+1,Z) - \lambda_\gamma(A,Z)\,n(A,Z), \qquad (2.9)\end{aligned}$$

where, λ_n, λ_γ and λ_β are the rates of the (n,γ), (γ,n) and β^--decay reactions, respectively.

In an isotopic chain, the build-up of the isotopes will continue as long as $\lambda_n \geq \lambda_\beta$. The rate of (n,γ) reaction, λ_n, will continuously decrease as the process goes further and further in the isotopic chain until it reaches

$$\lambda_n(A,Z) \approx \lambda_\gamma(A+1,Z).$$

At this point, the nuclide (A,Z) cannot capture any more neutron, and it *waits* before it undergoes β^--decay producing another nuclide $(A,Z+1)$ which can afterward continue capturing neutrons again. For this reason, the assumption of the $(n,\gamma) \rightleftharpoons (\gamma,n)$ equilibrium condition is referred to as the *waiting-point approximation*.

If successive neutrons are being added to a nucleus, the binding energy of the daughter nuclei gradually falls to zero, and this sets a limit to neutron addition to a nucleus. However, in the r-process, that limit is not attained since (γ,n) reaction will break-up the nucleus when its binding energy falls below a threshold.

Under the $(n,\gamma) \rightleftharpoons (\gamma,n)$ equilibrium along an isotopic chain, the abundance ratio of two nuclides (A,Z) and $(A+1,Z)$ of the isotopic chain can be obtained as [Kratz1988]

$$\frac{n(A+1,Z)}{n(A,Z)} = n_n\,\frac{G(A+1,Z)}{2G(A,Z)}\left(\frac{A+1}{A}\right)^{3/2}\left(\frac{2\pi\hbar^2}{ukT}\right)^{3/2} e^{S_n(A+1,Z)/kT}, \qquad (2.10)$$

where, $n(A,Z)$ is the abundance of the nuclide (A,Z), n_n is the neutron number density, $G(A,Z)$ is the partition function of the nuclide (A,Z), $S_n(A+1,Z)$ is the neutron separation energy of the nuclide $(A+1,Z)$, T is the temperature, u is the atomic mass unit, $\hbar$ is the Planck constant and k is the Boltzmann constant.

It is evident from Eq. (2.10) that the abundance ratio depends mainly on the neutron separation energy S_n, and it is a function of the temperature T and the neutron density n_n. Neglecting the relatively small differences in $G(A, Z)$ and A for the nuclides in the same isotopic chain, the neutron separation energy of the most abundant nuclei in the chain can be expressed as [Qian2003]

$$S_n^0 \approx kT\, ln \left[\frac{2}{n_n} \left(\frac{ukT}{2\pi\hbar^2} \right)^{3/2} \right]. \tag{2.11}$$

It follows from Eq. (2.11) that S_n^0 depends only on n_n and T. Therefore, for a particular set of n_n and T, the abundance maxima will occur at approximately the same neutron separation energy for different isotopic chains.

Due to the odd-even effect caused by pairing [Iliadis2007], nuclides with even N have higher S_n values than the nuclides with odd N. As a consequence, the most abundant nuclide in an isotopic chain always has an even N.

The flow of matter from one isotopic chain to the next takes place via β-decay. The derivative of the total abundance $n(Z)$ of an isotopic chain with the proton number Z can be expressed as

$$\frac{d\, n(Z)}{dt} = n(Z-1)\lambda_\beta(Z-1) - n(Z)\lambda_\beta(Z), \tag{2.12}$$

where,

$$n(Z) = \sum_A n(A, Z), \tag{2.13}$$

$$\lambda_\beta(Z) = \sum_A \lambda_\beta(A, Z) \frac{n(A, Z)}{n(Z)}, \tag{2.14}$$

and $\lambda_\beta(A, Z)$ is the β-decay rate of the nuclide (A, Z).

The term $n(A, Z)/n(Z)$ in Eq. (2.14) representing the individual population coefficient, denoted by $P(A, Z)$, is obtained from Eq. (2.10). The first term in Eq. (2.12) describes the creation of the element Z via β-decay from the element $Z - 1$, while the second term describes the destruction of the element Z via β-decay to the element $Z + 1$. Equation (2.12) determines the elemental abundance of an isotopic chain, while Eq. (2.10) determines the abundances of the isotopes belonging to a particular isotopic chain.

Assuming that initially all nuclides belong to a specific isotopic chain with the proton number Z_0, the boundary conditions for Eq. (2.12) can be given by

$$n(Z)_{t=0} = N_0 \quad \text{for } Z = Z_0 \tag{2.15}$$

and

$$n(Z)_{t=0} = 0 \quad \text{for } Z \neq Z_0. \tag{2.16}$$

The general solutions of the differential equation (2.12) with the above boundary conditions are given by [Iliadis2007]

$$n(Z_0)_t = N_0\, e^{-\lambda_\beta(Z_0)t} \tag{2.17}$$

and

$$n(Z)_t = N_0 \sum_{i=Z_0}^{Z} e^{-\lambda_\beta(i)t}\, \frac{\lambda_\beta(i)}{\lambda_\beta(Z)} \prod_{j=Z_0, j\neq i} \frac{\lambda_\beta(j)}{\lambda_\beta(j)-\lambda_\beta(i)} \quad (\text{for } Z \neq Z_0). \tag{2.18}$$

It follows from Eq. (2.18) that the total abundance $n(z)$ of an isotopic chain at time t is inversely proportional to the corresponding total β-decay rate $\lambda_\beta(Z)$.

If it is assumed that after a sufficient time t of the r-process ($t < \tau$), the rate of change of $n(Z)$ is zero, *i.e.*,

$$\frac{d\, n(Z)}{dt} = 0, \tag{2.19}$$

then,

$$n(Z)\, \lambda_\beta(Z) = \text{ constant.} \tag{2.20}$$

This assumption is referred to as the *steady flow approximation.* If the steady flow approximation is considered while the r-process is already in the $(n,\gamma) \rightleftharpoons (\gamma,n)$ equilibrium, the steady flow is referred to as the *steady β-flow* [Qian2003]. In this case, all the matter from an isotopic chain to the next is carried by only one or, in some instances, two nuclides with $S_n \approx S_n^0$ (waiting-point nuclides). The steady β-flow can take place only when the time t of the r-process is larger than the longest β-decay half-life [Freiburghaus1999]. As evident from Eq. (2.20), the abundance of a waiting-point nuclide in the steady β-flow is inversely proportional to its β-decay rate $\lambda_\beta(A,Z)$.

Under the steady β-flow approximation, assumption of an abundance $n(Z_{min})$ corresponding to the minimum Z (Z_{min}), is sufficient to calculate the r-process abundances (Eq. (2.20)) [Kratz1993]. The population coefficients $P(A, Z) = n(A, Z)/n(Z)$ for determining $\lambda_\beta(Z)$ can be calculated using Eq. (2.10). Thus, under the assumption of steady β-flow, knowing the neutron separation energies $S_n(A, Z)$ and the β-decay half-lives $T_{1/2}(A, Z) = ln\ 2/\lambda_\beta(A, Z)$, the whole abundance pattern for the r-process can be calculated for a given set of environment parameters n_n and T.

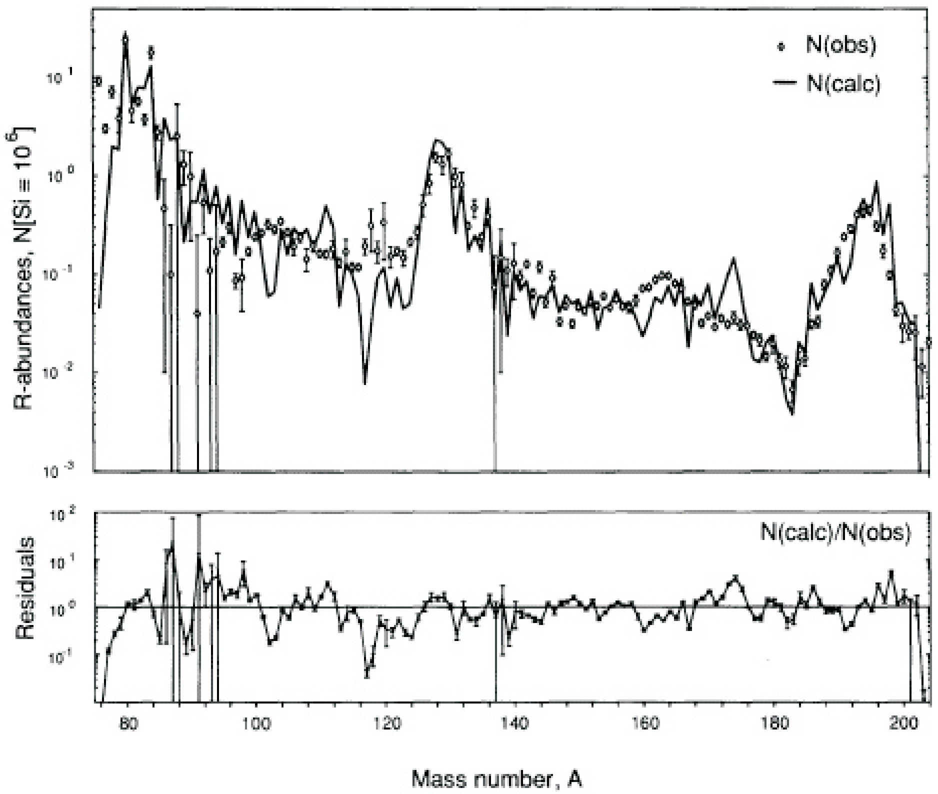

Figure 2.5: *Top:* Comparison of the observed solar r-abundances (data points) with the predictions from the classical r-process model (solid line). The 3 prominent peaks, each at $A \approx$ 80, 130 and 195, correspond to the magic neutron numbers $N = 50$, 82 and 126, respectively. The r-abundances are normalized so that the elemental abundance of Si is 10^6 [Anders1989, Suess1957]. *Bottom:* Residuals in terms of the ratio between the predicted and the observed abundances. (Figure taken from [Kratz1993].)

The nuclides with the neutron magic numbers[iii] are particularly important in the r-process. Due to their closed neutron shells, the half-lives of these nuclides are particularly longer ($T_{1/2} \approx 0.1-0.5$ s) than the other nuclides in the r-process ($T_{1/2} \approx 0.01-0.05$ s). As a result, the r-process encounters a sequence of waiting points at the same magic neutron number and the path moves vertically upward along Z. Because of the longer half-lives, the flow of abundance at a magic neutron number becomes slower, and the corresponding nuclides build up to relatively large abundances.

[iii] The magic numbers for nucleons (either protons or neutrons) are 2, 8, 20, 28, 50, 82 and 126. In

Figure 2.5 shows the distribution of the observed solar abundances due to the r-process in comparison to the predictions of the classical r-process model [Kratz1993]. Three prominent peaks, each at $A \approx 80$, 130 and 195 corresponding to the magic neutron numbers $N = 50$, 82 and 126, can be seen. A global steady β-flow approximation or a global time-dependent model failed to reproduce the observed abundances. The predicted abundance pattern is a superposition of 3 time-dependent components, each with different (T, n_n, t) parameters. The (T, n_n, t) parameters for the 3 components are $(1.35 \times 10^9,\ 3 \times 10^{20},\ 1.5)$, $(1.20 \times 10^9,\ 3 \times 10^{21},\ 1.7)$ and $(1.20 \times 10^9,\ 3 \times 10^{22},\ 2.5)$, respectively, where the temperature T is in K, the neutron density n_n is in cm^{-3} and the time scale t is in s. It is believed that different r-process events or different zones representing different conditions are responsible for the observed abundance pattern [Kratz1993].

The advantage of the waiting-point approximation is that knowledge of the neutron-capture cross-section is not required to calculate the individual abundance of the nuclides. However, it is valid only if either the temperature or the neutron number density is very high [Cameron1983]. If not, only a fraction of the flow of nuclei can reach the waiting point, since the flow will be steadily depleted by β-decay when it proceeds along an isotopic chain. Goriely *et al.* [Goriely1992] calculated that for a temperature of $T = 2 \times 10^9$ K, the approximation is valid when the neutron density, n_n is 10^{20} cm^{-3} or more. On the other hand, they found that the approximation is valid at $T = 1 \times 10^9$ K, only when the neutron number density n_n is more than 10^{28} cm^{-3}.

2.2.3 Need for experimental data for r-process calculation

The major difficulty in the calculation of the r-process abundances is the lack of nuclear data for the thousands of nuclei far from the valley of β-stability. The nuclear data required for the r-process prediction mainly include neutron separation energies (S_n), β-decay half-lives and branching for β-delayed neutron emission [Kratz1993]. While

---

the context of the r-process, the relevant neutron magic numbers are $N_0 = 50$, 82 and 126 [Iliadis2007].

β-decay rates determine the time-scale and abundance pattern, neutron separation energies play a major role in the $(n,\gamma) \rightleftharpoons (\gamma,n)$ equilibrium.

The lack of experimental nuclear data required in the r-process calculation at present is filled by the theoretical predictions from various mass models [Kratz1998]. Several models are widely used in the r-process calculations, among which HFB-14 [Goriely2007], FRDM [Möller1995] and KTUY [Koura2005] cover a wide range in the neutron-rich region of the nuclear chart. The HFB-14 (Hartree, Fock, Bogoliubov) model produced an rms error of 0.729 MeV when fitted to the 2149 measured masses obtained from the 2003 compilation of the Atomic Mass Evaluation (AME) [Audi2003]. The FRDM (Finite-Range Droplet Model) and the KTUY (Koura, Tachibana, Uno, Yamada) mass models produced an rms error of 0.678 MeV and 0.680 MeV respectively, when fitted to the measured masses from the earlier compilation of the AME [Audi1995].

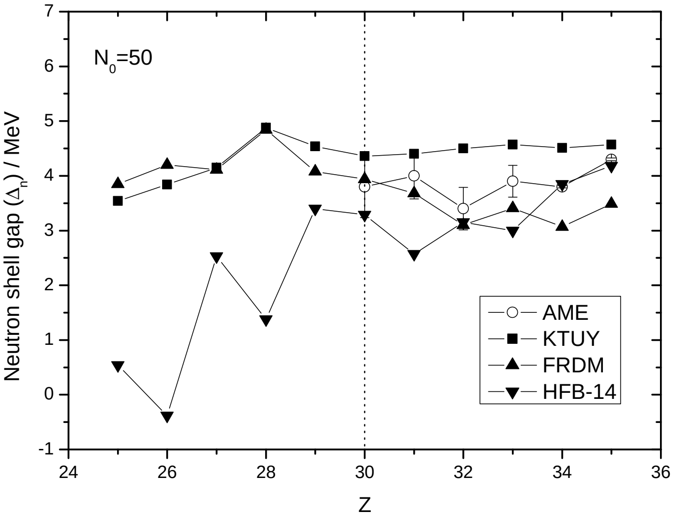

Figure 2.6: Comparison of the neutron shell-gap values (Δ_n) at the magic neutron number N_0=50 calculated from different mass models. The vertical line at $Z = 30$ highlights the values for ^{80}Zn from those models. Note the shell gap values calculated from the mass data obtained from the AME [Audi2003].

The differences of mass values predicted by different mass models are conveniently expressed in terms of either the proton shell gaps (for the proton-rich region) or the neutron shell gaps (for the neutron-rich region) [Lunney2003]. The neutron shell gap

Δ_n at the magic neutron number N_0 is defined by

$$\Delta_n(N_0, Z) = S_{2n}(N_0, Z) - S_{2n}(N_0 + 2, Z), \tag{2.21}$$

where, S_{2n} represents the two-neutron separation energy of the corresponding nucleus.

Figure 2.6 shows predictions of nuclear masses by different models in terms of the neutron shell gap energy (Δ_n) for the neutron magic number $N_0 = 50$. The difference of the Δ_n values predicted by the HFB-14 and the KTUY models, for example, at Z=30 (${}^{80}_{50}Zn_{30}$) is about 1 MeV. From the trend of the neutron shell gap, it is evident that as one goes away from the valley of β-stability, the difference in predictions from the different mass models increases. This can cause severe deviations in the calculated abundances [Qian2005, Freiburghaus1999]. Such deviations can be resolved only by experimental data.

Although progress has been made in the field of mass measurement of unstable nuclei, very few masses in the neutron-rich region have been measured so far which are involved in the r-process sequence. The β-decay half-lives of about 25 r-process nuclei have been measured including the waiting-point nuclei ^{80}Zn [Gill1986] and ^{130}Cd [Kratz1986]. Currently, in many Radioactive Ion Beam (RIB) facilities around the world including ISOLDE/Cern, GANIL, NSCL, Studsvik/OSIRIS, CPT/ANL and GSI, decay studies as well as mass measurement of the r-process nuclei are performed. In 2005, a major milestone was achieved at the ISOLTRAP experiment in ISOLDE with the measurement of mass of ^{80}Zn as part of this thesis. Masses of several other r-process nuclei in different mass ranges have been measured in Los Alamos Meson Physics Facility (LAMPF) [Seifert1994] and GSI [Stadlmann2004]. The efforts are continued to access more and more neutron–rich region for nuclear astrophysics studies at several laboratories world-wide including ISOLDE/CERN and GSI [Kratz2004, Kelic2006].

Chapter 3

Trapping of charged particles: The Penning trap

Ion traps have found considerable interest in the field of physics, chemistry and biology. From experiments such as test of $E = mc^2$ [Rainville2005] to mass-spectrometric analysis of biomolecules [Domon2006], ion traps have got vast range of applications. The 1989 Nobel prize for physics to Wolfgang Paul and Hans Dehmelt for their pioneering works was a recognition of the potential of this field.

3.1 Types of ion traps

Ion traps are three-dimensional trapping devices for charged particles. Primarily they can be divided into two broad categories: the ones which make use of a magnetic field for particle confinement (e.g. the Penning trap) and the others which use a radiofrequency electric field instead (e.g. the Paul trap). A typical trap consists of two hyperbolic endcaps with a ring electrode, the inner surface of which is the revolution of a hyperbola. In case of a Paul trap, between the ring and the endcap electrodes, a combination of a DC voltage (U_0) and an AC voltage (V_0) is applied. In the case of a Penning trap, instead of the AC electric field, a homogeneous magnetic field (B) is applied as shown in Fig. 3.1. In addition to the hyperbolic geometry, the linear variation of the Paul trap and the cylindrical variation of the Penning trap have proved useful in particle confinement and manipulation.

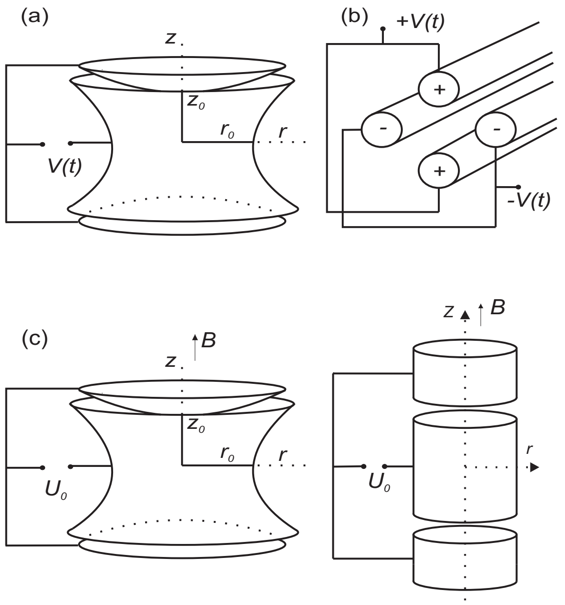

Figure 3.1: Typical geometry of the Paul trap (a), the linear rf trap (b), and the Penning trap with a hyperbolical (c, left) and cylindrical (c, right) configurations.

3.2 Equations of motion of a charged particle in a Penning trap

The confinement of charged particle in a Penning trap is achieved by the superposition of a homogeneous magnetic field $\vec{B} = B\hat{z}$ and a static quadrupolar electric potential with the form

$$\Phi = \frac{U_0}{4d^2}(2z^2 - x^2 - y^2), \tag{3.1}$$

where

$$d^2 = \frac{1}{2}\left(z_0^2 + \frac{r_0^2}{2}\right), \tag{3.2}$$

the so-called trap parameter, which is determined by the minimum distances r_0 and z_0 from the trap center to the ring electrode and to the endcaps, respectively. U_0 is the potential difference between the ring electrode and the endcaps. A charged particle under the influence of this combined electric and magnetic field will experience a Lorentz force and the equation of motion of the particle can be written as [Brown1986]

$$\frac{d^2\vec{x}}{dt^2} = \frac{q}{m}\left(\vec{E} + \frac{d\vec{x}}{dt} \times \vec{B}\right). \tag{3.3}$$

Setting

$$\omega_z = \sqrt{\frac{qU_0}{md^2}} \tag{3.4}$$

and

$$\omega_c = \frac{qB}{m}, \tag{3.5}$$

we can write,

$$\frac{d^2x}{dt^2} - \frac{\omega_z^2}{2}x - \omega_c\frac{dy}{dt} = 0, \tag{3.6}$$

$$\frac{d^2y}{dt^2} - \frac{\omega_z^2}{2}y - \omega_c\frac{dx}{dt} = 0, \tag{3.7}$$

$$\frac{d^2x}{dt^2} + \omega_z^2 z = 0. \tag{3.8}$$

The above equations show that the x and y motions are decoupled from the z motion of the particle, *i.e.*, the radial and the axial motions of the particle are independent. The axial motion is a simple harmonic oscillation with frequency ω_z:

$$z = A_z cos(\omega_z t - \phi_z), \tag{3.9}$$

where A_z and ϕ_z are respectively the amplitude and the phase which are determined by the initial conditions.

The solutions for the radial motion of the particle can be derived as

$$x = r_- cos(\omega_- t - \phi_-) + r_+ cos(\omega_+ t - \phi_+), \tag{3.10}$$

$$y = -r_- sin(\omega_- t - \phi_-) - r_+ sin(\omega_+ t - \phi_+), \tag{3.11}$$

where,

$$\omega_{\pm} = \frac{1}{2}\left(\omega_c \pm \sqrt{\omega_c^2 - 2\omega_z^2}\right). \tag{3.12}$$

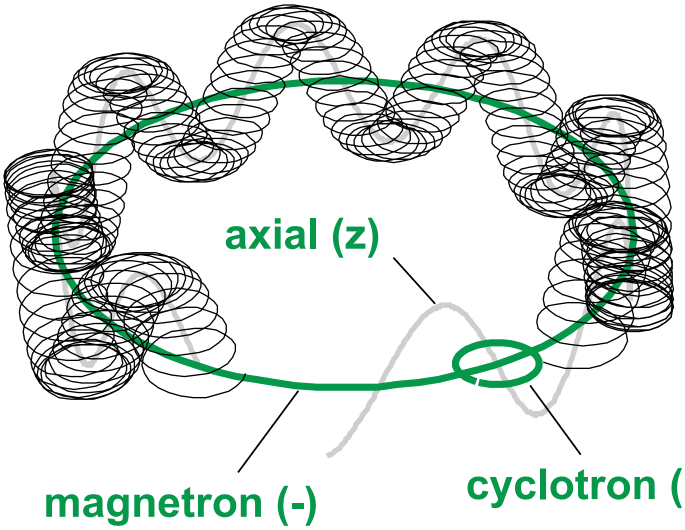

Figure 3.2: The motion of a charge particle in a Penning trap consists of 3 independent oscillations- the magnetron motion with frequency ω_-, the modified cyclotron motion with frequency ω_+ and the axial motion with frequency ω_z [Blaum2006].

The radial motion with the frequency ω_+ is called the cyclotron motion and the one with the frequency ω_- is called the magnetron motion. The two motions are circular with constant radii r_+ and r_-, respectively. Thus, the ion in a Penning trap possesses three independent modes of oscillations with frequencies ω_+, ω_- (both radial) and ω_z (axial) as shown in Fig. 3.2. The magnetron frequency, ω_-, can be approximated as independent of the mass and charge of the particle for typical operating conditions with a weak electrostatic potential ($\approx$ 10 V) and a strong magnetic field ($\approx$ 5 Tesla). The two radial frequencies are related by the following equation:

$$\omega_+ + \omega_- = \omega_c. \tag{3.13}$$

This relation is the working principle of the mass measurement and the buffer-gas cooling technique at ISOLTRAP.

3.3 Manipulation of ion motion

The motion of a charged particle can be manipulated by the application of an external time-varying electric field. Two configurations which are widely used for the application of the azimuthal electric rf field are the dipolar and the quadrupolar configurations (Fig. 3.3 *left* and *middle*). The figure shows cuts of the ring electrode in the azimuthal plane, which is segmented into 2 or 4 parts. Another configuration, namely, the octupolar configuration is currently studied for a possible deployment in the ion-motion manipulation (Fig. 3.3 *right*) (see Chapter 5).

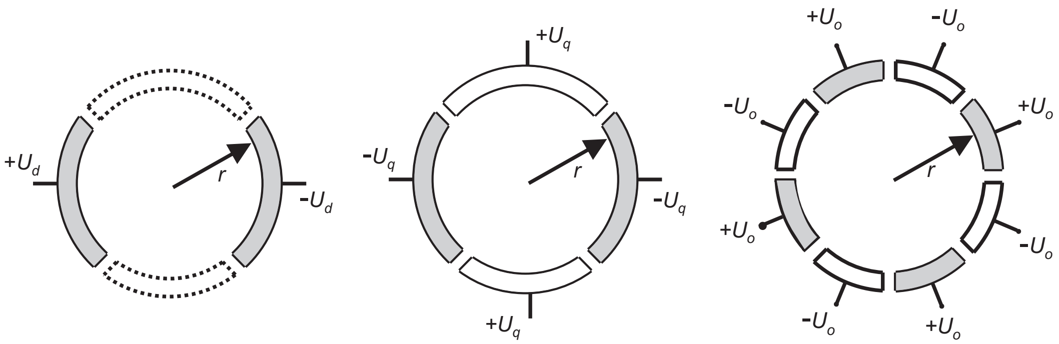

Figure 3.3: Electrode geometry for the application of the dipolar, quadrupolar and the octupolar electric field in the azimuthal plane. The ring electrode is segmented into 2, 4 or 8 parts in order to apply the dipolar, quadrupolar or the octupolar excitation field, respectively.

3.3.1 Dipolar excitation

Dipolar configuration for excitation is achieved by applying two rf voltages with a phase difference of π to two opposing ring segments as shown in Fig. 3.3 (left). The resulting dipolar potential can be written as

$$\Phi_d = a_d \frac{U_d}{r_0} cos(\omega_d t - \phi_d) \times x, \tag{3.14}$$

where U_d, ω_d and ϕ_d are the amplitude, frequency and phase of the rf voltages. The term a_d is a geometrical factor which corrects the strength of the dipolar term of the multipole expansion of the potential. The electric field can thus be expressed as

$$\vec{E_d} = -\vec{\nabla}\ \Phi_d = -a_d \frac{U_d}{r_0} cos(\omega_d t - \phi_d)\hat{x}. \tag{3.15}$$

The equations of motion of the charged particle in the trap under the excitation now take the form:

$$\ddot{x} - \frac{\omega_z^2}{2}x - \omega_c \dot{y} = -k_0 cos(\omega_d t - \phi_d), \tag{3.16}$$

$$\ddot{y} - \frac{\omega_z^2}{2}y + \omega_c \dot{x} = 0, \tag{3.17}$$

and

$$\ddot{z} + \omega_z^2 z = 0, \tag{3.18}$$

where

$$k_0 = a_d \frac{q}{m}\frac{U_d}{r_0}. \tag{3.19}$$

From the above set of equations it is clear that the axial part of the motion is uneffected and only the radial part will be influenced by the excitation. The radial parts of the equations can be expressed in complex notation by

$$\ddot{u} - \frac{\omega_z^2}{2}u + i\omega_c \dot{u} = -k_0 cos(\omega_d t - \phi_d), \tag{3.20}$$

where $u = x + iy$.

The solutions of these equations can be written as

$$x = r_-(t)cos(\omega_- t - \phi_-) + r_+(t)cos(\omega_+ t - \phi_+), \tag{3.21}$$

$$y = -r_-(t)sin(\omega_- t - \phi_-) - r_+(t)cos(\omega_+ t - \phi_+). \tag{3.22}$$

If the excitation rf voltage is applied exactly at the magnetron or the reduced cyclotron frequency, *i.e.* in resonance, the following expression for the radius of the respective motion can be derived [König1995]:

$$r_{\pm}(t) = \sqrt{r_{\pm}^2(0) + \frac{k_0^2 t^2}{4(\omega_+ - \omega_-)^2} \mp \frac{r_{\pm}(0) k_0 t sin(\phi_d - \phi_+)}{\omega_+ - \omega_-}} \tag{3.23}$$

In the above equation, if the phase difference, $\phi_d - \phi_+$, is equal to $\frac{3\pi}{2}$ (when excitation is applied at the reduced cyclotron frequency) or $\frac{\pi}{2}$ (when excitation is applied at the magnetron frequency), the expression can be written as

$$r_{\pm}(t) = r_{\pm}(0) + \frac{k_0}{2(\omega_+ - \omega_-)} t. \tag{3.24}$$

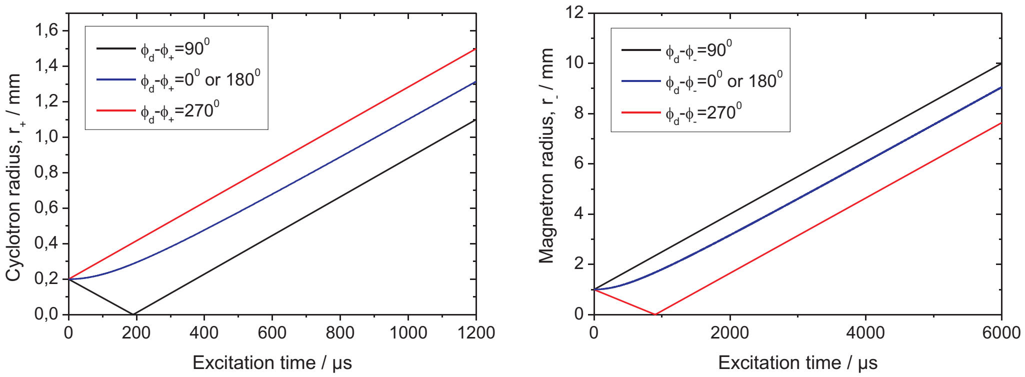

Figure 3.4: Evolution of the cyclotron and the magnetron radii (*left* and *right*, respectively) of an ion as a function of time under the dipolar excitation at different phases of excitation. For the case of the excitation at ω_+ (*left*), r_+ is directly proportional to t when $\phi_d - \phi_+ = 3\pi/2$, while for the case of the excitation at ω_- (*right*), r_- is directly proportional to t when $\phi_d - \phi_- = \pi/2$ [Blaum2003].

Figure 3.4 shows the behavior of r_+ and r_- as a function of the excitation time t at different $\phi_d - \phi_{\pm}$. For the case of the dipolar excitation at ω_+, r_+ is directly proportional to t when $\phi_d - \phi_+ = 3\pi/2$. Similarly, for the case of the excitation at ω_-, r_- is directly proportional to t when $\phi_d - \phi_- = \pi/2$. This technique is commonly used to increase the magnetron radius of the trapped ions to a defined value in the Penning trap.

3.3.2 Quadrupolar excitation

The electrode configuration for the quadrupolar excitation is shown in Fig. 3.3 (*middle*). The quadrupolar potential can be written as

$$\Phi_q = a_q \frac{U_q}{r_0^2} cos(\omega_q t - \phi_q) \times (x^2 - y^2), \tag{3.25}$$

where a_q is a geometric factor arising due to the shape of the ring electrode segments. The components of the corresponding electric field can be written as

$$E_{q,x} = -\vec{\nabla}\ \Phi_q = -2a_q \frac{U_q}{r_0^2} cos(\omega_q t - \phi_q) \cdot x, \tag{3.26}$$

$$E_{q,y} = -\vec{\nabla}\ \Phi_q = 2a_q \frac{U_q}{r_0^2} cos(\omega_q t - \phi_q) \cdot y, \tag{3.27}$$

$$E_{q,z} = 0. \tag{3.28}$$

The equations of motion of the particle under the excitation can thus be obtained as

$$\ddot{x} - \omega_c \dot{y} - \left[\frac{\omega_z^2}{2} - 2k_0 cos(\omega_q t - \phi_q)\right] x = 0, \tag{3.29}$$

$$\ddot{y} + \omega_c \dot{x} - \left[\frac{\omega_z^2}{2} + 2k_0 cos(\omega_q t - \phi_q)\right] y = 0, \tag{3.30}$$

and

$$\ddot{z} + \omega_z^2 z = 0, \tag{3.31}$$

where

$$k_0 = a_q \frac{q}{m} \frac{U_q}{r_0^2}. \tag{3.32}$$

Equations (3.29 - 3.31) show that the axial part of the motion is uneffected by this excitation, too. The radial equations of motion can again be solved in the same way as in the case of dipolar excitation. In the case when the frequency of the exciting field is equal to the sum of the frequencies of the radial motion, *i.e.* in resonance, $\omega_q = \omega_+ + \omega_-$, the term $r_\pm(t)$ takes the following form [König1995]:

$$r_\pm(t) = r_\pm(0)cos\left(\frac{\omega_{conv}}{2}t\right) \mp r_\mp(0)sin\left(\frac{\omega_{conv}}{2}t\right)cos(\phi_q - \phi_+ - \phi_-), \tag{3.33}$$

where

$$\omega_{conv} = \frac{k_0}{2(\omega_+ - \omega_-)}. \tag{3.34}$$

If the phase difference between the exciting field and the radial motions, $\phi_q - \phi_+ - \phi_-$, is equal to π, $r_\pm(t)$ can be obtained as

$$r_\pm(t) = r_\pm(0)cos\left(\frac{\omega_{conv}}{2}t\right) \pm r_\mp(0)sin\left(\frac{\omega_{conv}}{2}t\right). \tag{3.35}$$

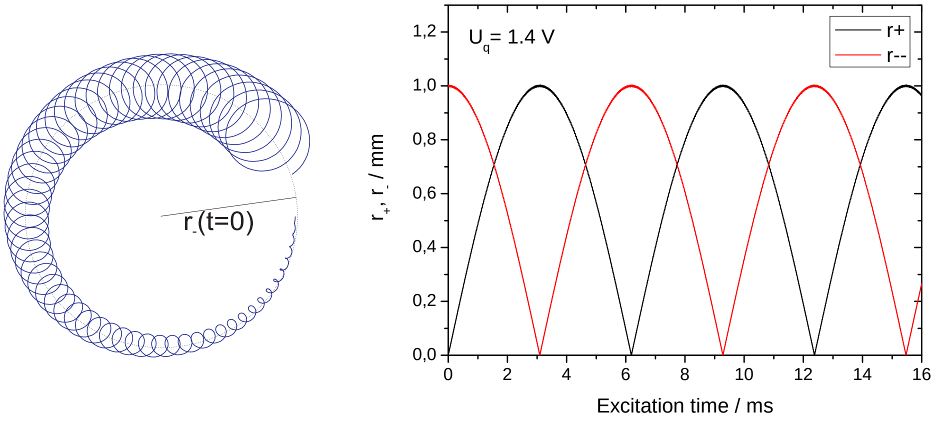

Figure 3.5: Conversion between the two radial motions under the quadrupolar excitation (ion motion in the radial plane (left) and evolution of the cyclotron and the magnetron radii (r_+ and r_-, respectively) with the excitation time (right)) [König1995].

From Eq. (3.35), it is evident that the two radial motions are continuously being converted into one another and the frequency of conversion from one radial motion to the other is ω_{conv}. Figure 3.5 shows this conversion between the two radial motions. If the time of excitation t is equal to π/ω_{conv} for a particular excitation strength, a full conversion from one motion into the other is attained.

3.3.3 Time-of-flight cyclotron resonance

The time-of-flight cyclotron resonance technique for the detection of the cyclotron frequency of the ion mainly consists of two parts: quadrupolar excitation of the ion at its cyclotron frequency $\omega_c = \omega_+ + \omega_-$ in the Penning trap and interaction of the ion's magnetic moment with the gradient of a magnetic field after the ion's ejection from the Penning trap towards a detector. This method was first introduced by Gräff *et al.* in the field of precision mass spectrometry [Gräff1980].

The quadrupolar excitaton is preceded by a dipolar excitation at ω_- to increase the magnetron radius r_- of the ions to a defined value r_d. A quadrupolar excitation is then applied in the radial plane of the trap using the four segments of the ring electrode. When $\omega_q = \omega_c$, resonance occurs and the initial magnetron motion is fully converted to a cyclotron motion after a time $T_q = \pi/\omega_{conv}$. The ion then attains a cyclotron radius $r_+ = r_d$. This leads to an increase of the radial kinetic energy of an ion after the quadrupolar excitation:

$$\Delta E_r \propto \omega_+^2 r_d^2 - \omega_-^2 r_d^2 \approx \omega_+^2 r_d^2 \tag{3.36}$$

In the case of the non-resonant ions, the gain in the radial kinetic energy is less and in the case of the resonant ions, the gain is more. For a rectangular-shaped excitation signal, the final radial kinetic energy is given by [König1995]

$$E_r \propto \frac{sin^2(\omega_b T_q)}{\omega_b^2}, \tag{3.37}$$

where

$$\omega_b = \frac{1}{2}\sqrt{(\omega_q - \omega_c)^2 + (\omega_{conv}/2)^2}. \tag{3.38}$$

After the quadrupolar excitation, when the ions are ejected from the trap toward the detector, the ion travels through a magnetic field gradient. The radial motion of the ion interact with the magnetic field gradient giving rise to a force in the axial direction (along the trap and the detector):

$$\vec{F} = \mu(\vec{\nabla} \cdot B) = -\frac{E_r}{B}\frac{\partial B}{\partial z}\widehat{z}. \tag{3.39}$$

This results in the reduction of the time-of-flight for the resonant ions. The time-of-flight from the trap center at $z = 0$ to the detector at $z = z_1$ is given by [König1995]

$$T(\omega_q) = \int\limits_{z=0}^{z_1} \sqrt{\frac{m}{2[E_0 - qU(z) - E_r(\omega_q)B(z)/B]}}dz, \tag{3.40}$$

where E_0 is the axial kinetic energy of the ion after ejection from the trap, and $U(z)$ and $B(z)$ are the magnitudes of the electric and magnetic fields, respectively, along the axial direction.

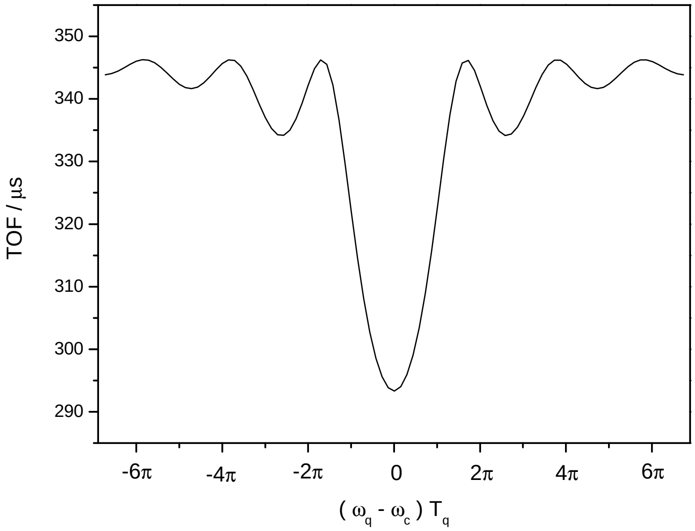

Figure 3.6: Theoretical line-shape of a time-of-flight cyclotron resonance for a Fourier-limited quadrupolar excitation signal.

In the experiment, the frequency of the quadrupolar excitation is scanned around the probable value of the cyclotron frequency $\nu_c = \omega_c/2\pi$ of the ion. At each frequency, the excitation signal is switched on for a time $T_{rf} = T_q$. For an excitation signal with a rectangular envelope, the line-shape of the resulting resonance is shown in Fig. 3.6. The line-shape of the resonance has been derived by König *et al.* [König1995].

The characteristic side-bands of the resonance are due to the Fourier-limited excitation signal. By fitting the experimental data points with the functional representation of the line-shape through the least-squares method, the cyclotron frequency ν_c of the ion is determined. Using the value of ν_c, and knowing the ion charge q and the magnetic field strength B, the mass of the ion can be calculated following Eq. (3.5).

3.3.4 Cooling of trapped ions

A buffer gas can be used for collisional cooling of the investigated ions. However, the collisions between the buffer-gas molecules and the investigated ions result in a loss of kinetic energy of the ions. This in turn results in a relatively slow increase of the magnetron radius and a very fast decrease of the cyclotron radius. The increase of the magnetron radius leads to a loss of ions after collision with the ring electrode's inner surface. To overcome this problem, a quadrupolar excitation can be used at the cyclotron frequency of the investigated ions in presence of the buffer gas, which will continuously convert the magnetron motion into the cyclotron motion [Savard1991]. As a result, the ions of interest get centered as shown in Fig. 3.7 (*right*). The magnetron radii of the other ion species, which remain uneffected by the excitation, continue to

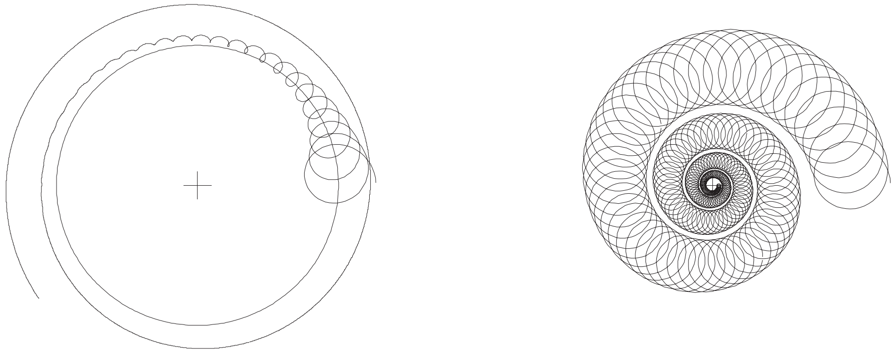

Figure 3.7: Trajectory of an ion under quadrupolar excitation in presence of a buffer gas. *left*: with the excitation applied at a frequency far away from the cyclotron frequency ν_c, *right*: with the excitation applied at the cyclotron frequency ν_c. Figure taken from [Savard1991].

increase resulting in the loss of those unwanted ions after hitting at the trap electrodes (*left*).

Since this technique is mass-selective, it is widely used for removing unwanted ion species from the trap.

Chapter 4

The ISOLTRAP experiment

4.1 The online isotope separator ISOLDE

Radioactive isotopes are produced in the Isotope Separator On-Line DEvelopment facility 'ISOLDE' at CERN, Geneva [Kugler2000]. More than 60 elements and about 600 isotopes can be produced in the facility. Figure 4.1 shows the layout of the ISOLDE hall. High-intensity proton pulses, accelerated by CERN's Linac and Proton Synchrotron Booster to 1 or 1.4 GeV energy, are delivered to the ISOLDE target every 1.2 second. Each pulse contains about 3×10^{13} protons. Radioactive nuclides are produced from the target by means of spallation, fission and fragmentation processes. The products diffuse out of the tube of the target material to the ion source, where they are ionized either by surface ionization, electron impact in hot plasma or resonant laser ionization process. The ions are then accelerated to an energy of 60 keV and sent to one of the mass-separators for removing unwanted ions from the beam. There are two magnetic mass-separators at ISOLDE. One is the so-called General Purpose Separator (GPS) with a single bending magnet. It has a resolving power up to 2400. The other one is the High Resolution Separator (HRS) consisting of two bending magnets with an elaborate ion-optical system. The HRS has a maximum resolving power of about 5000 [ISOLDE2008]. The ion beam from one of the mass-separators is then fed to the main beam-line and delivered to the various experiments such as ISOLTRAP in the experiment-hall.

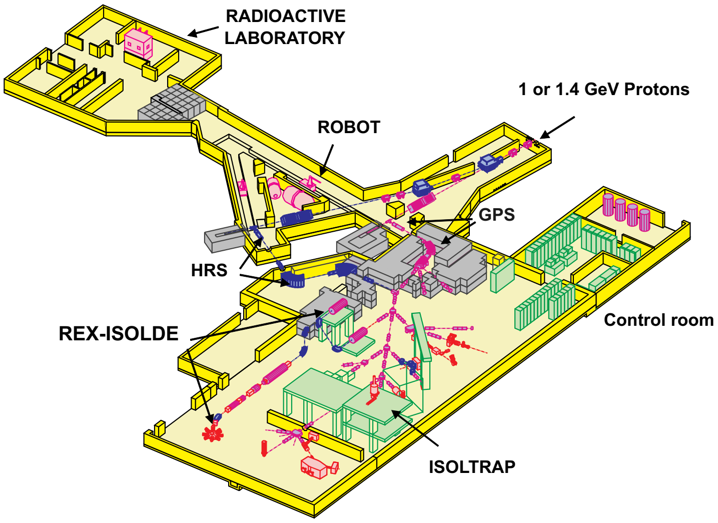

Figure 4.1: Sketch of the experiment-hall of the ISOLDE facility. The ISOLTRAP setup is located at the end of the central beam-line. (Figure taken from [ISOLDE2008].)

4.2 The ISOLTRAP setup

The ISOLTRAP experiment [Bollen1996, Mukherjee2008] installed at the on-line mass-separator facility ISOLDE is devoted to high-precision mass-measurements on short-lived nuclides. The principle of the mass measurement is based on the determination of the ion cyclotron frequency in a Penning trap.

The setup of the ISOLTRAP experiment consists of three main parts: a linear rf quadrupole for cooling and bunching the ion beam, a cylindrical Penning trap, referred to as the Preparation Penning trap, for cooling and preparing the ions of interest, and a hyperbolic Penning trap, referred to as the Precision Penning trap, for the cyclotron frequency measurement. A schematic diagram of the setup is shown in Fig. 4.2. In the following sections, the various components of the setup are described.

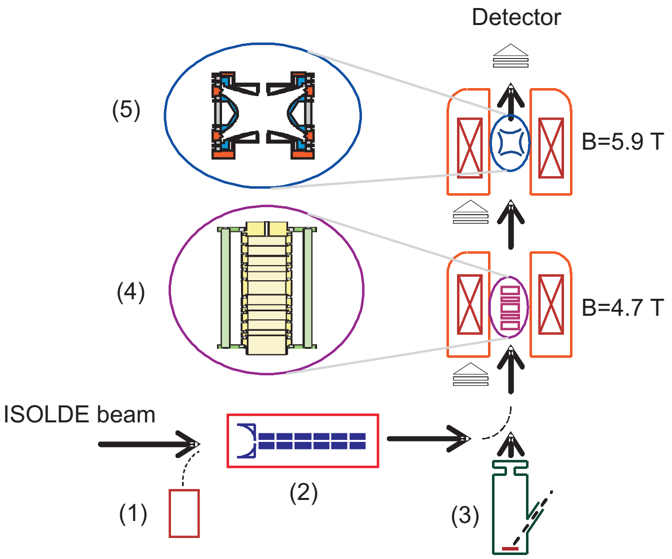

Figure 4.2: Sketch of the ISOLTRAP setup. The various components shown are: (1) the reference ion-source, (2) the RFQ cooler and buncher, (3) the carbon cluster ion-source, (4) the Preparation Penning trap and (5) the Precision Penning trap. The Preparation and the Precision Penning traps are located inside two superconducting magnets of field-strengths 4.7 T and 5.9 T, respectively. A Channeltron detector records the time-of-flights of the ions.

4.2.1 The reference ion-source

The reference ion-source produces alkali ions which are used as references in the cyclotron frequency measurement of the radioactive nuclides. The masses of these nuclides are known with a relative uncertainty of 10^{-9} or lower [Audi2003]. The ion-source is based on the surface ionization technique. A heated tungsten ionizer is used for the evaporation and ionization of ^{23}Na, ^{39,41}K, ^{85,87}Rb and ^{133}Cs atoms. The desired alkali element is kept in the form of a zeolite and is heated to about 1000^0 C. Small pieces of tungsten wires are immersed into the zeolite to increase the ionization efficiency.

The radioactive ion beam delivered from ISOLDE has a kinetic energy of 60 keV. In order to be able to use similar ion-optical settings for both the reference and the radioactive ion beams during an experiment, the reference ion-source is also kept at a 60-kV platform.

4.2.2 The RFQ cooler and buncher

The linear radio-frequency quadrupole (RFQ) [Herfurth2001], along with a special injection electrode called Egg-cup, cools, accumulates and bunches the 60-keV ion beam delivered either from ISOLDE or the reference source. The assembly of the RFQ and Eggcup is kept at a potential of 60 kV. The 60-keV incident beam is first decelerated to about 100 eV and then injected into the RFQ. The RFQ consists of four segmented rods. The rf voltage applied to the four rods produces a transverse focusing force and the dc voltages applied to the different segments of the four rods produce a potential minimum axially near the ejection electrode of the RFQ (Fig. 4.3).

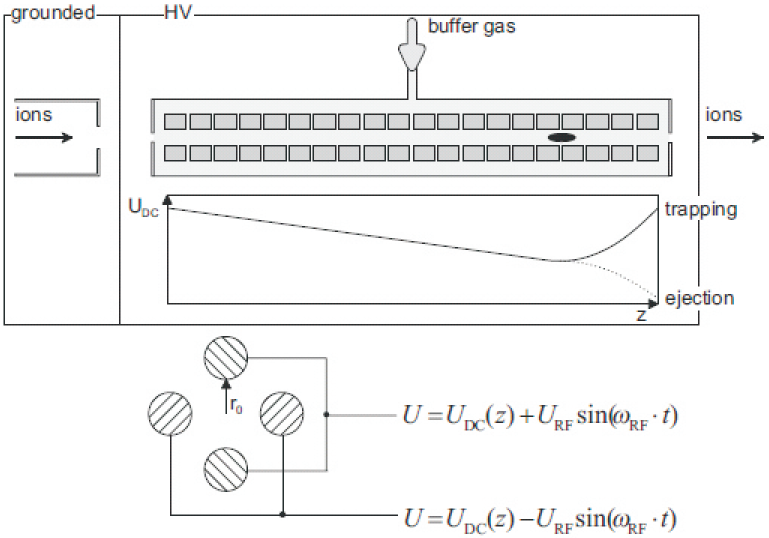
grounded
HV
buffer gas
ions
ions
U_{DC}
trapping
ejection
z
r_0
$U = U_{DC}(z) + U_{RF}\sin(\omega_{RF} \cdot t)$
$U = U_{DC}(z) - U_{RF}\sin(\omega_{RF} \cdot t)$

Figure 4.3: Sketch of the RFQ cooler and buncher. *Top*: longitudinal view of the RFQ. *Bottom*: transverse view of the four rods of the RFQ, and the applied rf and dc voltages. The ion beam is confined radially by the resulting rf field and cooled due to collisions with the buffer gas. The dc voltages applied to the different segments of the rods produce a potential minimum in the axial direction, where the ions are accumulated for a few ms before being ejected in bunch toward the Preparation Penning trap. (Figure taken from [Herfurth2001].)

The RFQ is operated in presence of a buffer gas, He, which takes out radial and longitudinal energy of the ions by means of collision. The buffer gas He is kept at a pressure of about 10^{-3} mbar. The ions, after loosing their kinetic energy, finally accumulate in the potential well, forming an ion bunch. The bunch is extracted by switching the potential of the last rod-segments after a cooling and accumulation time of a few milliseconds.

After leaving the high voltage platform of 60 kV, the ions again attain an energy of 60 keV. To prevent this, two pulsed drift tubes are used in succession after the RFQ. The first tube is initially kept at a potential of 57.3 kV. When the ions enter the tube, they have a kinetic energy of 2.7 keV. As they traverse through the field free region of the cavity, the potential of the tube is switched to ground. As a result, ions leave the tube with a kinetic energy of 2.7 keV. In a similar way, the second drift tube further lowers the ion kinetic energy to about 100 eV for efficient capture of the ions in the Preparation Penning trap.

4.2.3 The carbon cluster ion source

Since the unified atomic mass u is defined as 1/12 of the mass of ^{12}C, using carbon clusters as mass references, absolute mass measurements can be performed [Blaum2002]. Moreover, one can study the systematic uncertainties of the setup using different carbon clusters [Kellerbauer2003].

Investigation of the systematic uncertainties of the ISOLTRAP setup has been performed [Kellerbauer2003] by using the carbon cluster ion source. The different carbon clusters are produced via laser ionization of C_{60} fullerenes. The source consists of a sample-holder, an ion-optical system for focusing the ions and an extraction electrode. A frequency-doubled Nd-YAG pulsed laser with wavelength λ=532 nm and an average power of 15 mW is used. The ions are created at a potential so that their kinetic energy is similar to the ions coming from the RFQ (see Fig. 4.2). The sample-holder is being rotated during laser irradiation to ensure uniformity of the sample surface.

4.2.4 The Preparation Penning trap

The Preparation Penning trap is located in a magnetic field of 4.7 T, and is operated under a buffer gas, He, maintained at a pressure of $10^{-3} - 10^{-4}$ mbar. The functions of this trap are to clean the ion of interest from isobaric contaminants and to prepare a cold ion bunch to be delivered to the Precision Penning trap.

The trap consists of 13 electrodes creating a potential well [Hartmann1997] as shown in Fig. 4.4. The trap is 25 cm long and has a diameter of 35 mm. The ring electrode is segmented into eight equal parts in order to apply a quadrupolar or possibly an octupolar rf field in the radial plane. The ion bunches delivered by the RFQ are captured and trapped axially in the potential well. Due to the collisions of the ions with the buffer gas, the ions loose their energies related to their axial, cyclotron and magnetron motions. Cooling of the magnetron motion leads to an increase of the magnetron radius. In addition, a dipolar excitation is applied for about 100 ms at a frequency around the magnetron frequency of the ion of interest. Since the magnetron frequency is very loosely dependent on the mass of the ion, the magnetron radii of both the ion of interest and the ions of the isobaric contaminants increase due to the excitation. The amplitude of the dipolar excitation is chosen in such a way that the magnetron radii of the ions increase to a value larger than the aperture (≈ 3 mm in diameter) at the exit of the trap. A quadrupolar excitation is then applied at the cyclotron frequency of the ion of interest (typically for about 50 ms). This leads to the centering [Savard1991] of the corresponding ion species (see Section 3.3.4), while the other ion species are lost after collision with the inner surface of the ring electrode. The excitation time for the quadrupolar excitation depends on the amplitude of the

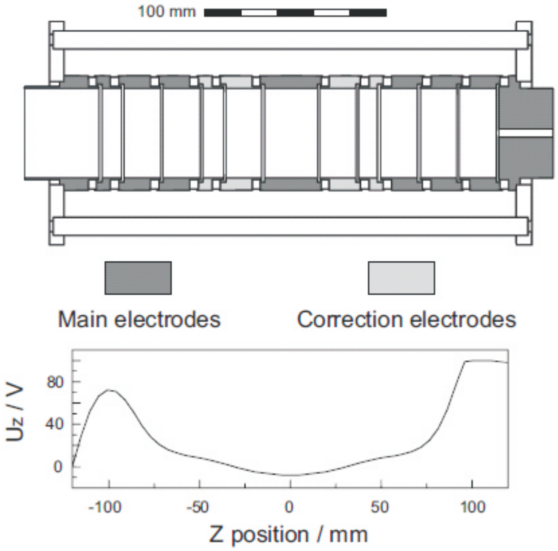

Figure 4.4: *Top*: Sketch of the Preparation Penning trap. This trap of cylindrical geometry is 25 cm long and its diameter is 35 mm. *Bottom*: Potential obtained by applying appropriate voltages to the electrode segments along the axial direction [Hartmann1997].

excitation as well as the helium buffer-gas pressure. The typical resolution[i] of this trap is of the order of $10^4 - 10^5$ [Hartmann1997], which is sufficient for removing isobaric contaminations of the ion of interest.

4.2.5 The Precision Penning trap

The Precision Penning trap is of hyperbolic geometry (Fig. 4.5) designed to ensure minimum electric and magnetic field imperfections [Bollen1996]. Correction electrodes are used in order to compensate for the deviations from the ideal quadrupolar field, and materials with low susceptibility values are used for the trap construction to minimize the magnetic field inhomogeneities induced by the trap material. The ring electrode is segmented into four equal parts in order to apply quadrupolar rf field in the radial plane.

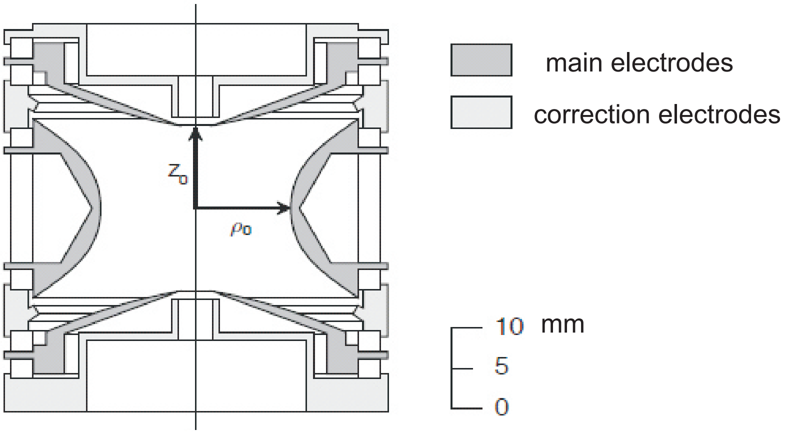

Figure 4.5: Sketch of the Precision Penning trap. This hyperbolical Penning trap has an inner diameter of 26 mm. The correction electrodes help reduce the deviation from the ideal quadrupolar field. (Figure taken from [Mukherjee2008].)

The trap is located in a 5.9 T magnetic field and is operated under high vacuum (few times 10^{-8} mbar). The ions coming from the Preparation Penning trap toward the Precision Penning trap are dynamically captured in the Precision trap by switching the voltage of the lower endcap. At the appropriate switching time, the axial energy of the captured ions are minimum, as both the trap center are kept at the same potential. In addition, the ions coming from the Preparation trap have very small radial-energy spread. After capture in the Precision trap, the cyclotron radius is almost zero and the magnetron radius is about 0.2 mm.

---

[i] The resolving power depends mainly on the buffer gas pressure. Lower is the buffer gas pressure, higher is the resolving power. But this requires long cooling and excitation times [König1995].

Procedure for mass measurement

For the cyclotron frequency determination, the ion motion is excited in two steps. First, a dipolar excitation is applied in the radial plane at the magnetron frequency of the ion (for about 10ms) to increase the magnetron radius to a defined value. If an isobaric or isomeric contamination is present, a dipolar excitation at the cyclotron frequency of the contaminant ion can be applied. This results in an increase of the cyclotron radius of the contaminant ion and eventually leads to the loss of the ion. This cleaning procedure typically reaches a resolving power of 10^7 in an excitation time of 1 second.

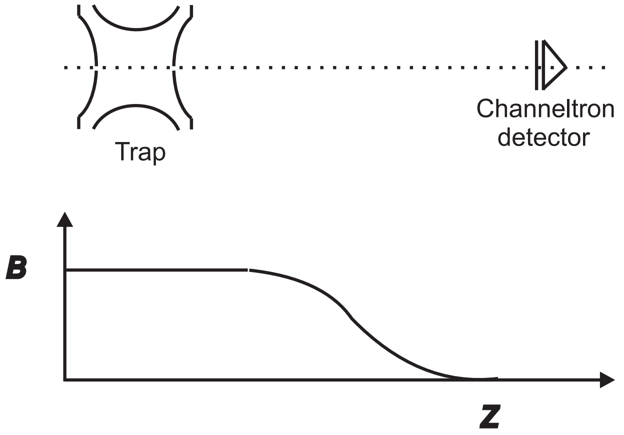

Figure 4.6: The spatial variation of the magnetic field between the Precision trap and the Channeltron detector. The magnetic field gradient along the axial direction gives rise to an axial force $\vec{F} = -\vec{\mu}(\vec{\nabla} \bullet \vec{B})$.

After removing the contaminant ion(s), a quadrupolar excitation is applied at the cyclotron frequency of the ion of interest (typically for 900 ms). If the excitation time and the amplitude are correct, a full conversion from the magnetron motion to the

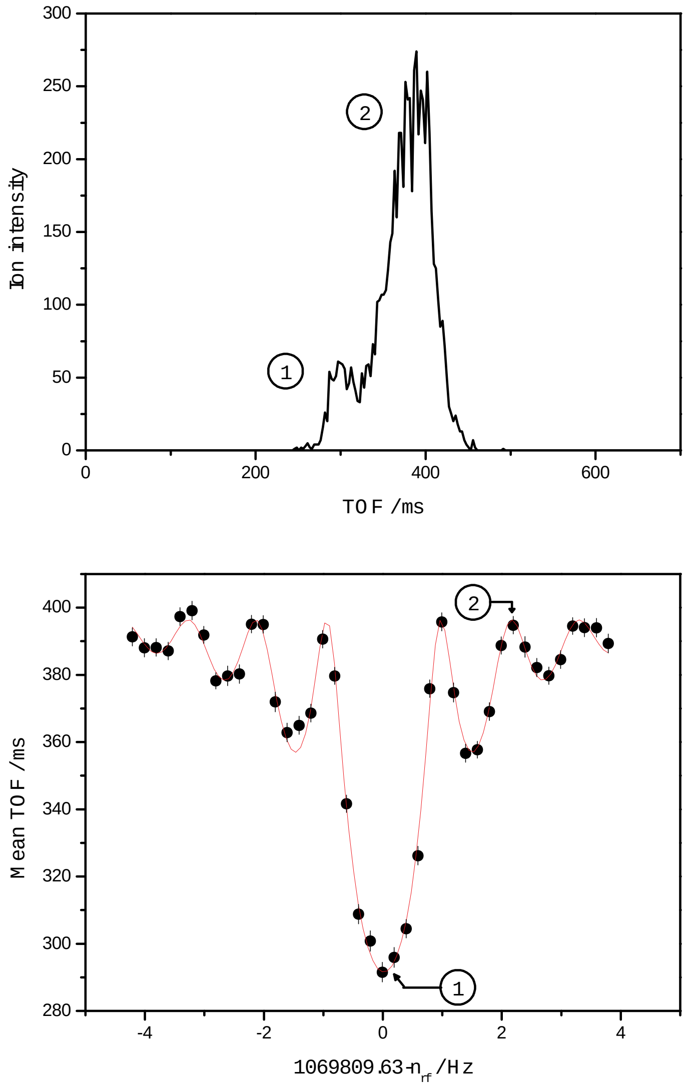

Figure 4.7: The ion TOF signal for $^{85}Rb^{+}$ (*top*) and the corresponding resonance with a fit (*bottom*). The excitation time-duration for this resonance spectrum is 900 ms and a resolving power of $\nu/(\delta\nu)_{FWHM} \approx 8.2 \times 10^{5}$ has been achieved.

cyclotron motion is achieved, which results in the maximum gain in radial energy (see Eq. (3.36)). After ejection of the ion from the trap toward the Channeltron detector, which is located about 1.2 m away from the Precision trap, the ion travels through a magnetic field gradient (Fig. 4.6). Due to interaction of the ion's magnetic moment with the magnetic field gradient, the ion experiences an axial force toward the detector. This results in a shorter time-of-flight for the resonant ion than the non-resonant ion (Eqs. (3.39-3.40)).

Figure 4.7 shows a typical TOF signal for ^{85}Rb and the corresponding resonance with a theoretical fit [König1995]. The mass of the ion is calculated by using the value of the measured cyclotron frequency obtained from the fit. The determination of the magnetic field to calculate the mass value is done by using a stable reference ion whose mass is already known with a high precision.

The line-width of the resonance curve depends on the excitation time (T_{rf}) of the quadrupolar excitation, and it is given by [König1995]

$$\delta\nu(FWHM) \approx \frac{0.9}{T_{rf}}. \tag{4.1}$$

This indicates that the mass resolution strongly depends on the time of quadrupolar excitation.

Chapter 5

Simulation of octupolar excitation

Mass measurement in the Penning trap is performed by determining the cyclotron frequency, $\omega_c = (qB)/m$, using an azimuthal rf quadrupolar field as explained in Chapter 3. When the frequency of the exciting rf field matches with the cyclotron frequency, the ion motion undergoes a conversion between the magnetron and the cyclotron motions. When the frequency of the rf field is scanned around ω_c with a specific time of excitation, the typical cyclotron resonance curve is obtained; the width of the central peak being approximately equal to the reciprocal of the excitation time.

Since the mass resolution by this technique is directly proportional to the time of the exciting quadrupolar field, the resolution for the very short-lived nuclides ($T_{1/2} \leq 50ms$) is very poor. Therefore, it is of great interest to explore the possibility for employing a new excitation technique to determine the cyclotron frequency with a better resolution. There exists several possibilities in order to increase the mass resolution, the first being the use of a higher magnetic field. Secondly, one can increase the charge state of the ions in the Penning trap. Thirdly it may be possible to achieve an improvement in the resolving power by exciting the ion at a higher harmonic of the cyclotron frequency. Applying an excitation field at $2\omega_c$, for example, requires an octupolar field [Ringle2007, Eliseev2007]. The present chapter gives an account of a numerical study on the application of an rf octupolar field for the detection of the ion cyclotron frequency.

5.1 Simulation of the octupolar excitation

There has been no analytical derivation of the equation of ion motion under the octupolar excitation in a Penning trap so far. The numerical simulation presented here are based on a fourth-order Runge-Kutta routine and the simulation is performed in the IDL environment on a 2 GHz Windows PC. Only one ion has been used for the simulation and different possible conditions for the excitation are considered to imitate a measurement.

Method of simulation

The radial components of the electric field produced by an rf octupolar field can be written as

$$E_x = \frac{U_o}{r_0^4}(y^3 - 3x^2y)sin(\omega_{rf}t + \phi_{rf}) \tag{5.1}$$

and

$$E_y = -\frac{U_o}{r_0^4}(x^3 - 3y^2x)sin(\omega_{rf}t + \phi_{rf}). \tag{5.2}$$

Although it is not possible to directly derive the ion trajectories under the above electric field, it is possible to calculate the radii of the ion, r_+ and r_-, as a function of time. The ion position coordinates and the corresponding velocities are calculated at each timestep with an interval of 1×10^{-8} second in the simulation. The radii can then be calculated back from the position coordinates and the corresponding velocities against the time of excitation.

An ion of mass 720 u is considered which gives the possibility for a future experimental investigation with C_{60} in the ClusterTrap experiment [Schweikhard2003]. The trap diameter used is 2 cm and the magnetic field is 5 Tesla.

The configuration of the eight segments of the ring electrode for applying the octupolar excitation is shown in Fig. 5.1.

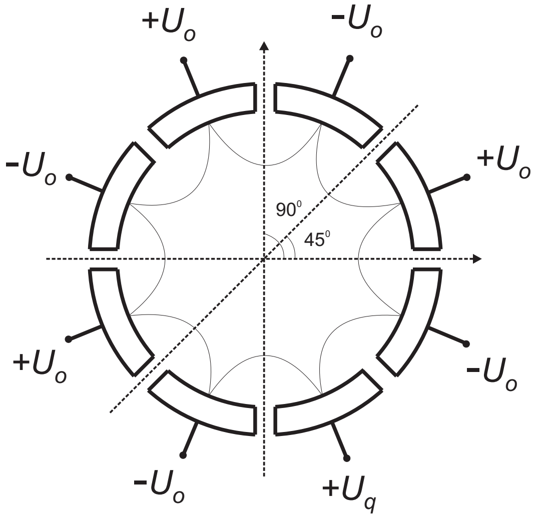

Figure 5.1: Configuration of the eight segments of the ring electrode for applying octupolar excitation.

5.2 Results and discussion

5.2.1 Influence of octupolar excitation on the ion motion

Figure 5.2 shows the evolution of the magnetron and cyclotron radii with the time of excitation at an excitation phase $\phi_{rf} = 0$ degree. The ion initially has a pure magnetron motion i.e. $r_{+,0} = 0$ when the excitation is applied. A periodic beating is observed which resembles the structure of a square wave. The periodic beating structure seems to have dependence on the phase of the excitation and also on the phase of the initial magnetron motion. At 0^0 and 180^0 of the excitation phase, the time-period of beating is seen to be the minimum, while at 90^0 and 270^0 of the excitation phase, the time-period of the beating is maximum. It can be noted here that the case of the quadrupolar excitation, the time-period of beating is constant for any excitation phase variation. In case of the octupolar excitation, another effect observed is that the time of first conversion is not equal to the half of the beating time-period unlike in the case of quadrupolar excitation. At excitation phase 90^0 and 270^0, the difference between time of first conversion and the beating time-period is maximum, while at 0^0 and 180^0, it is found to be minimum.

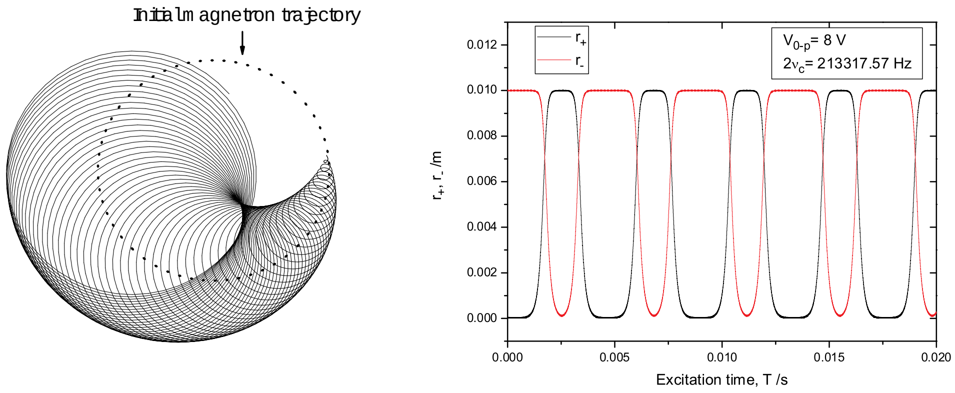

Figure 5.2: Conversion between the two radial motions of an ion under the octupolar excitation in the radial plane (left); evolution of the magnetron and the cyclotron radii with the time duration of the excitation (right).

In the case of quadrupolar excitation, the beat frequency ν_B is directly proportional to the excitation amplitude V_0 and does not depend on any other parameter of the ion. In case of octupolar excitation, ν_B has been found to be dependent both on the initial magnetron radius ($r_{-,0}$) and the initial magnetron phase ($\phi_{-,0}$) in addition to the excitation amplitude (V_0). Figure 5.3(top) shows the dependence of the beat frequency on the initial magnetron radius for different initial magnetron phases $\phi_{-,0}$.

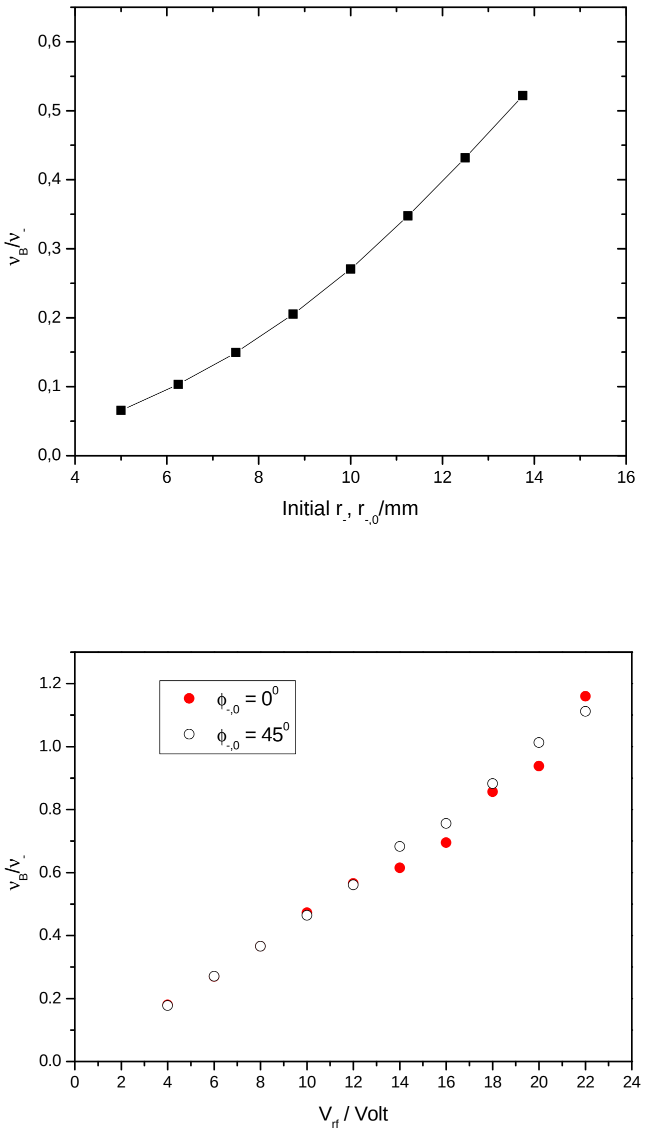

Figure 5.3: *Top*: The beat frequency against the initial magnetron radius. The magnetron phase of the excitation is kept constant at 0^0. The line joining the points is for visual guidance. *Bottom*: The time duration for the first conversion and the required amplitude of the octupolar excitation. The amplitude is inversely proportional to the time duration.

Keeping both $r_{-,0}$ and $\phi_{-,0}$ constant, the beat frequency is shown in the figure 5.3(bottom) against V_0 for different $\phi_{-,0}$. As seen in the figure, as the ratio ν_B/ν_- increases, the linearity the ratio and the amplitude of excitation ceases, and the data points look more and more scattered. Ringle et. al. [Ringle2007] have summed up the dependence of the beat frequency on the initial magnetron and cyclotron radii, amplitude of excitation and the phases of the ion motion as well as of the excitation as,

$$\nu_B \propto \alpha(r_{\pm,0}, \phi_{\pm,0}, \phi_{rf}) \cdot (r_{+,0}^2 + r_{-,0}^2) \cdot V_{rf}, \tag{5.3}$$

where α is a scaling factor depending on the initial parameters of the ion and of the excitation.

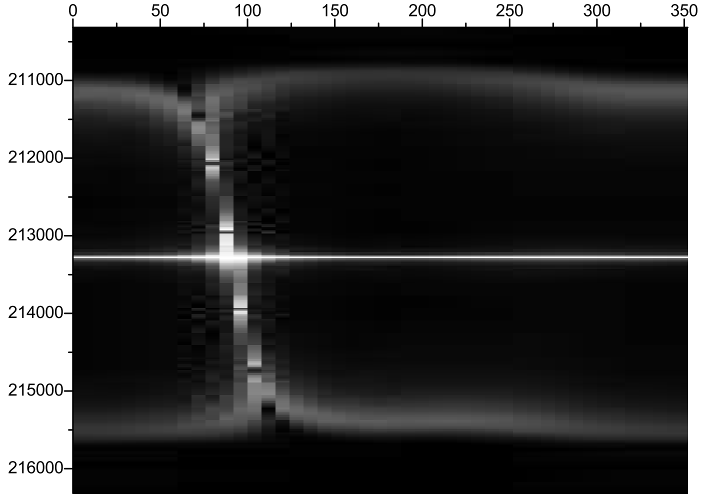

Figure 5.4: Cyclotron radius r_+ as a function of the frequency ν_{rf} and the phase ϕ_{rf} of the excitation field. The brightest (and the darkest) points indicate the maximum (and the minumum) magnitude of the cyclotron radius.

5.2.2 Octupolar resonance profile

The resonance profile with octupolar excitation is characterized by the fact that it is dependent on the phase of the excitation even if the ion has pure initial magnetron or cyclotron motion. In the case of the quadrupolar excitation, if the ion initially has only one type of motion, the shape of the resonance curve is independent of the phase of the

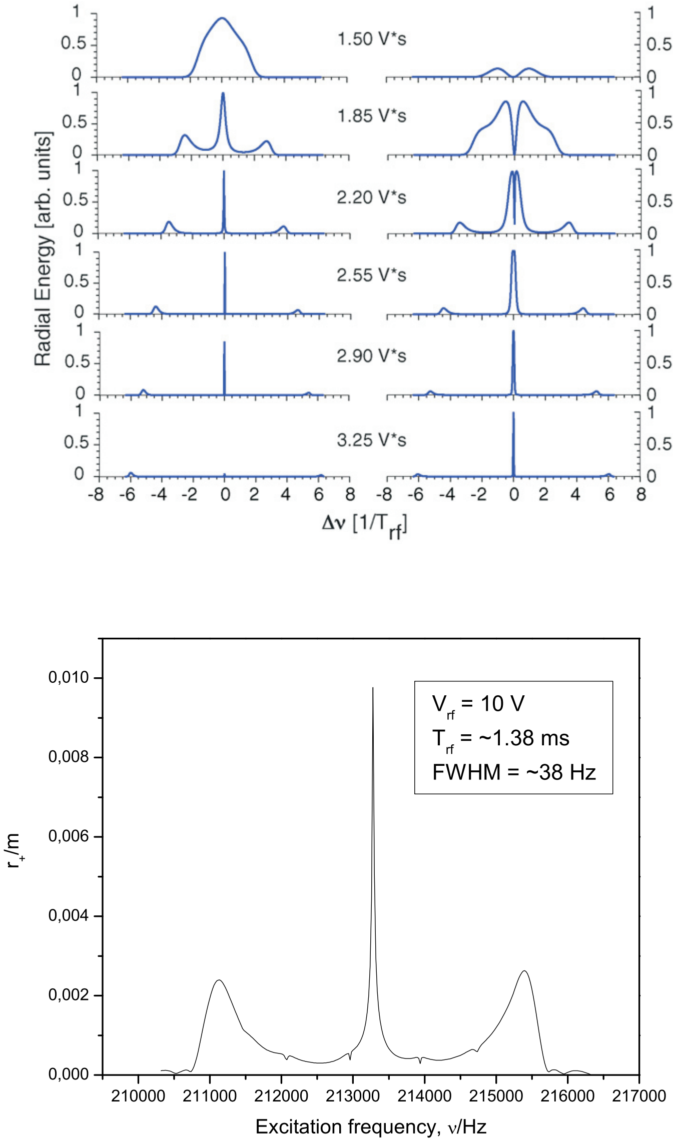

Figure 5.5: *Top*: Radial energy as a function of frequency detuning for various products of amplitude and duration of the excitation for the two cases: $\phi_{rf} = 0^0$ (left) and $\phi_{rf} = 22.5^0$ (right) [Ringle2006].*Bottom*: Cyclotron radius as a function of the excitation frequency averaged over the rf phases from 0 degree to 360 degree with an interval of 8 degree.

excitation. On the other hand, for the case of octupolar excitation the shape of the resonance varies considerably, producing either peak or a dip at the resonant frequency, $2\nu_C$.

Figure 5.4 shows the dependence of the resonance curves on the exciting phase. A transition of a peak across the span of the rf phases can be observed in addition to a constant peak at the resonant frequency $2\nu_c$. Typically, a resonance curve consists of a central peak along with an additional peak whose position depends on the phases of the excitation, provided the other parameters are kept constant, which is evident from the plot.

Depending on the product of the amplitude and the time-duration of the excitation ($V_{rf} \times T_{rf}$), the shape of the resonances can be seen to vary significantly producing either a peak or a dip at the center of the resonance [Ringle2006], keeping the other parameters constant. In figure 5.5(top), the radial energy can be seen against the detuning of the excitation frequency from $2\nu_c$ for two initial magnetron phases, 0^0 and 22.5^0. As evident from the plot, in order to use the octupolar excitation, application of the proper parameters will be a crucial factor so as to have the FWHM of the resonance as small as possible. For the case of $\phi_{rf} = 22.5^0$, the FWHM of the resonance at the bottom of Fig. 5.5(top) is less than $1/(100 \times T_{rf})$ [Ringle2006]. This will correspond to a 200-fold increase in the resolving power of the cyclotron frequency with the octupolar excitation over the quadrupolar excitation.

Phase-averaged resonance profile

Although the FWHM of the octupolar resonance at certain conditions of the ion and excitation is less than that with the quadrupolar excitation, the techniques for achieving those conditions in experiment have not yet been feasible. Even for an assemble of trapped ions with a defined magnetron radius and negligible cyclotron radius, there will be a distribution of the magnetron phases. Unlike the quadrupolar excitation, this distribution of the initial magnetron phases will result in different shapes of resonances. Alternatively, keeping the magnetron phase constant and changing the rf phase, this effect can be observed. Figure 5.5(bottom) shows an average profile of the resonances, averaged over the phases of excitation. For this particular case, the resolving power corresponds to a 20-fold increase over the quadrupolar case for the same time duration of excitation.

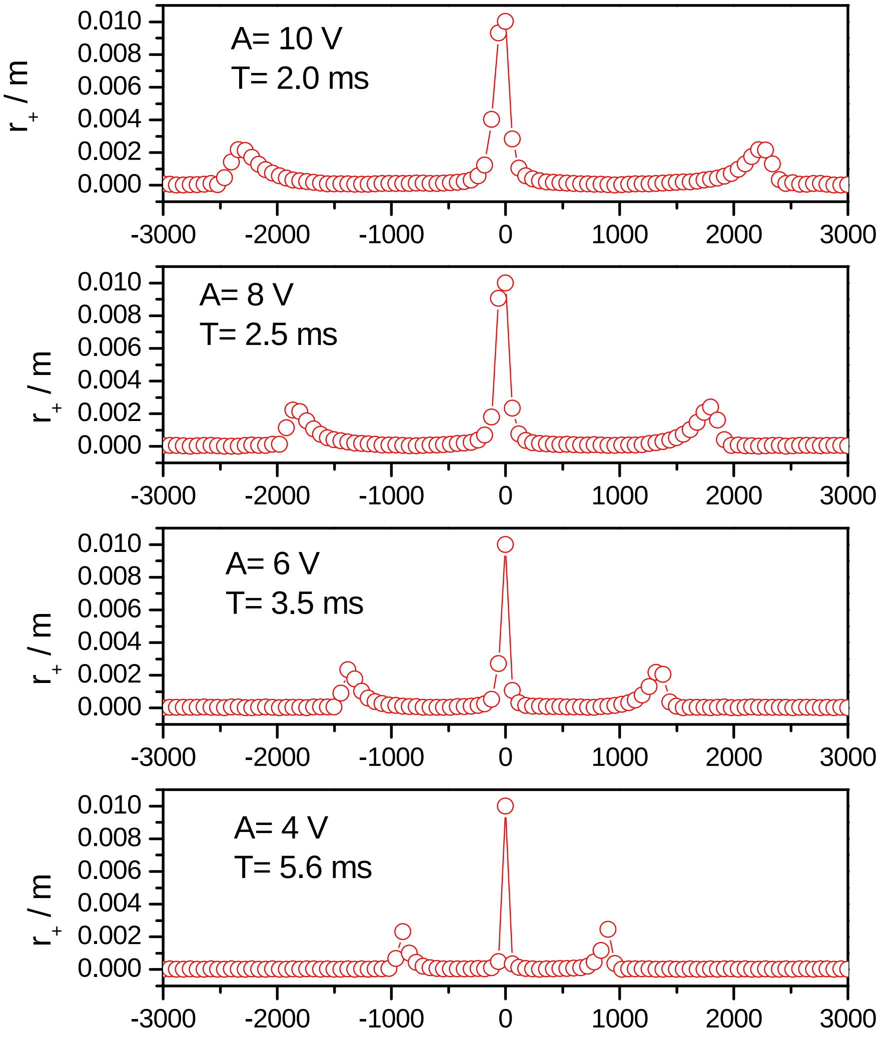

Figure 5.6: Cyclotron radius as a function of the detuning from $2\nu_c$ for different excitation times. The FWHM ($\Delta\nu$) of the central peaks are found to vary inversely with the excitation time-duration with the proportionality constant being 0.25.

5.2.3 Line-shape and FWHM of the resonance profile

The line-shape of the octupolar resonance depends crucially on the ion's initial parameters. For example, at a magnetron phase of 90^0, when the excitation is applied with an rf phase of 0^0, the line-shape consists of a central peak both side of which are two secondary peaks. As the phase of excitation is scanned, it is observed that an additional secondary peak starts moving from one side of the resonance to the other as evident from the contor plot. The shape and size of the central peak is also effected by change of excitation phase, hence the FWHM changes from phase to phase. In Fig. 5.5(bottom) is shown the average plot of the resonances taken at various phases ranging from 0^0 to 360^0at equal interval of phase. The average profile is seen to be symmetric and has two secondary peaks equidistant from the central peak. For this particular case of 10 volt excitation, the FWHM of the central peak has been found to be about 38 Hz, for an excitation time of 1.38 ms. In the case of the quadrupolar excitation, this time of excitation would result in a FWHM of about 725 Hz. This indicates that an improvement of resolution by a factor of about 20 can be expected.

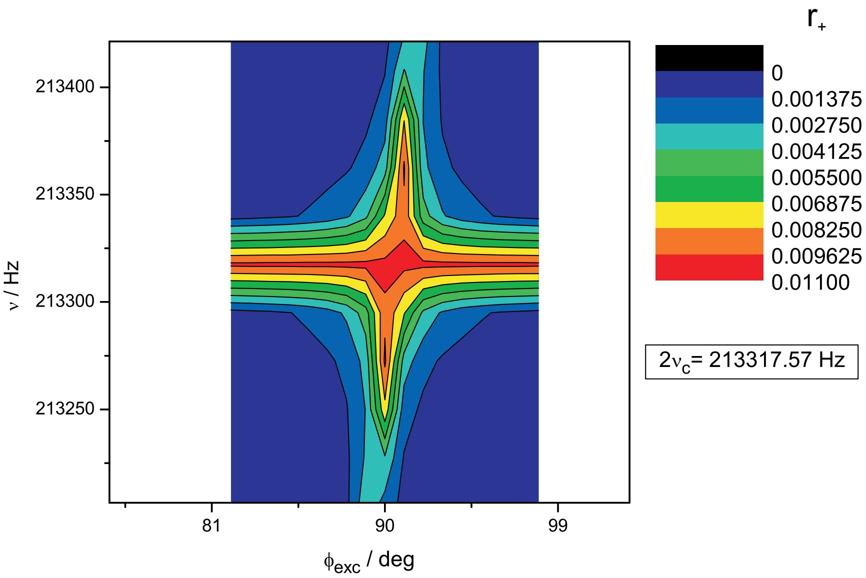

Figure 5.7: Contor plot of the cyclotron radius r_+ as a function of the frequency ν_{exc} and the phase ϕ_{exc} of the excitation.

Figure 5.6 shows the movement of the secondary peaks when the amplitude of excitation is changed. When the amplitude is decreased, the two peaks gradually come closer to the central peak. The dependence is linear and the two peaks would merge with the central peak in the case of zero excitation amplitude. The FWHM of the central peaks too are found to decrease with the increase of the excitation time or decrease of the excitation amplitude. For this particular excitation phase of 90^0, the FWHM of the central peaks are found to vary inversely with the excitation time-duration with the proportionality constant being 0.25. In Fig. 5.7, the same movement of the secondary peaks can be seen around the central peak against change of phase, keeping the amplitude and time of excitation constant. Moreover, appearance of an additional secondary peak is realized.

5.3 Outlook

The application of octupolar excitation crucially depends on the initial ion parameters. This suggests that the preparation of the ions for the excitation will be very important. Although more work, both in the fields of simulation and theoretical calculations, is required, the application of octupolar excitation in future ion-trap experiments looks promising, specially with very short-lived radio-nuclides.

Chapter 6

Mass measurements of neutron-rich Zn isotopes

The mass measurements of the neutron-rich Zn isotopes from $A = 71$ to 81 were performed in October 2005 at ISOLTRAP which lasted for about one week. The masses were measured with a relative uncertainty $\delta m/m$ of the order of 10^{-8}. The mass of one of the crucial r-process waiting-points, ^{80}Zn, was measured for the first time with such a high precision. Also, the mass of the isotope ^{81}Zn was measured for the first time.

This chapter presents the details of the measurements and explains the analysis procedures of the experimental data. Also, the new mass values are compared with their predicted values from different mass models.

6.1 Production of the Zn isotopes

The neutron-rich Zn isotopes, $^{71-81}$Zn, were produced at the ISOLDE/CERN facility [Kugler2000] via fission reactions as a result of the bombardment of a ^{238}UCx target with neutrons having energy in the MeV range [Catherall2003]. The neutrons required for the fission reactions were obtained from spallation reactions caused by impingement of a 1.4 GeV proton beam on a tungsten rod placed in front of the ^{238}UCx target. The tungsten rod used for producing the neutrons is known as the neutron-converter. The neutron-converter is used primarily for the following reason: if the energetic proton beam is directly impinged on the uranium target, the resulting spallation reactions will contribute heavily, producing neutron-deficient nuclides, instead of the neutron-rich nuclides [Bernas2003].

The 20 cm-long target in the form of a tube contained natural uranium of thickness 50 g/cm^2 and graphite of thickness 10 g/cm^2. The protons bombarding on the tungsten rod had an energy of 1.4 GeV and an intensity up to 4 μA. Protons with such energy and intensity typically produce 10^{13} fission-spallation products per second when bombarding directly the ^{238}UCx target in absence of the neutron-converter.

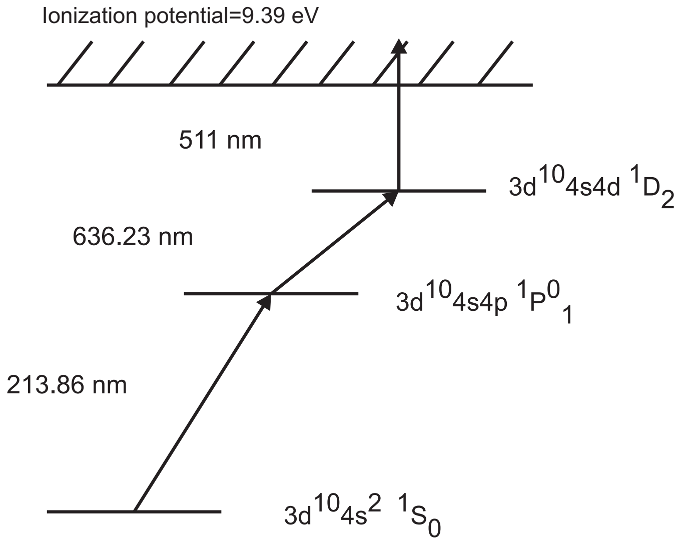
Ionization potential=9.39 eV
511 nm
3d^{10}4s4d ^{1}D$_2$
636.23 nm
3d^{10}4s4p ^{1}P$^0_1$
213.86 nm
3d^{10}4s^2 ^{1}S$_0$

Figure 6.1: Excitation scheme for resonant laser ionization of Zn [Köster2005].

The *release* of an isotope involves its diffusion and desorption from the target material and effusion to the ion source. After its release from the target material, the atom of an isotope passes through a transfer tube made of quartz glass. It is usually referred to as the quartz transfer line. The quartz transfer line is chemically selective in the sense that it allows only a particular element to diffuse into the ion source. This is possible because the transfer line is kept at a temperature which is just sufficient to allow transfer of that element, while retaining most of the other elements by condensation on the inner surface of the tube. The Group 12 elements of the periodic table (Zn, Cd etc.) have high volatility compared to the neighboring elements because of their closed atomic configuration ($d^{10}s^2$). So only the Zn isotopes could diffuse into the ion source while the radio-isotopes of other less volatile elements would condense on the surface of the transfer tube for a longer time and would undergo nuclear decay. In this process, most of the isobars of the Zn nuclides (Ga, Ge, Cu, Ni etc.) were prevented from diffusing through the transfer line.

Although a relatively clean Zn beam was obtained by using the temperature-controlled transfer tube, it was not free from bromine and krypton isobars. To get rid of these remaining impurities, the Resonance Ionization Laser Ion Source (RILIS) [Fedoseyev2000] was used. The principle of this technique is that an atom can overcome its ionization threshold as a result of resonant absorption of laser radiation quanta. The ionization is done in a hot cavity in the form of a tube of diameter 3 mm. It is kept at about 1950^0 C and is connected to the target container where the nuclides are produced. For resonant laser ionization of Zn, a previously developed 3-step ionization scheme was used. The scheme, as shown in Fig. 6.1, uses a first transition with wavelength 213.86 nm, achieved via frequency-tripling of the dye laser, from the 3d^{10}4s^2 ^{1}S$_0$ ground state to the 3d^{10}4s4p ^{1}P$_1^0$ excited state. The second resonant transition with 636.23 nm to the 3d^{10}4s4d ^{1}D$_2$ state is followed by a non-resonant transition to the continuum with the green copper vapor laser light at 511 nm.

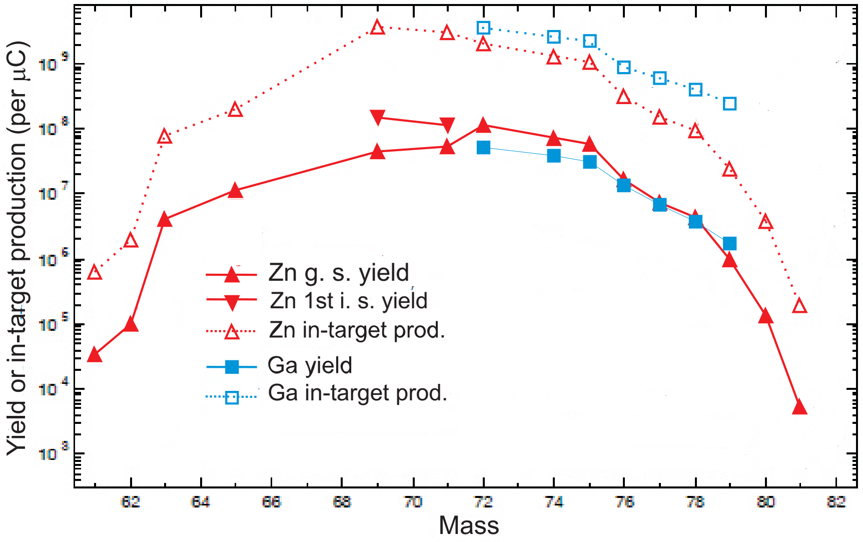

Figure 6.2: Yields (filled symbols) and estimated in-target production rates (open symbols) of Zn and Ga isotopes. In the cases of ^{69}Zn and ^{71}Zn, the yields of the first excited states were higher than the yields of the ground states. (Figure adopted from [Köster2005].)

The *yields* of various isotopes, defined as the corresponding beam intensity normalized to 1 μC of the incident proton beam, were measured using a Faraday cup. Yield of an isotope indicates the available beam intensity of that isotope for any experiment. The *in-target production rate* for an isotope indicates the estimated limit of the beam intensity of that isotope that could be reached with an ideal target (no decay losses) of the same thickness and dimensions [Köster2003]. Figure 6.2 shows the yields and in-target production rates of Zn and Ga isotopes. Note that in the cases of ^{69}Zn and ^{71}Zn, the first excited (isomeric) states were found to have higher yields than the ground states.

6.2 The method for data analysis

6.2.1 Atomic Mass Evaluation

The atomic mass of a nuclide is usually expressed in terms of the mass-excess

$$\mathrm{ME} = m - A\,u, \tag{6.1}$$

where m is the atomic mass of the nuclide with the mass number A, and u is the unified atomic mass unit. The atomic masses of the nuclides along with their mass-excess values and other properties are published and maintained in the Atomic Mass Evaluation [Audi1993, Audi1995, Audi2003]. Every few years, the database is updated with any new or improved value of atomic mass. The most recent version of the AME was published in 2003 [Audi2003]. At ISOLTRAP, the mass of the investigated nuclide m is determined by measuring the cyclotron frequencies of that nuclide as well as of a standard nuclide, called the *reference*, whose mass m_{ref} is already known with a high precision. Assuming that all the ions have the same charge $q = +e$, the atomic mass of the investigated nuclide can be obtained[i] from

$$m = \frac{\nu_c^{ref}}{\nu_c}\left(m_{ref} - m_e\right) + m_e, \tag{6.2}$$

where m_e is the electron mass.

The uncertainty σ_m of m given by

$$\sigma_m^2 = \left(r \cdot \sigma_{m,ref}\right)^2 + \left(m_{ref} - m_e\right)^2 \cdot \sigma_r^2, \tag{6.3}$$

---

[i] The electron binding energies (≈ eV) can be neglected for a mass uncertainty above 1 keV.

where $r = \nu_c^{ref}/\nu_c$, and σ_r and $\sigma_{m,ref}$ are the uncertainties of r and m_{ref}, respectively. By this way, one incorporates an additional uncertainty arising from the reference mass's uncertainty, which is subject to change. To avoid this problem, the ISOLTRAP values are always expressed in terms of the frequency ratio r. In order to be used in the AME as input data, the frequency ratios are needed to be expressed in linear mass relations as described in [Ames1999]. The linear equations are then used for the general adjustment calculation, which takes into account all previous measurements on the relevant nuclides.

6.2.2 Data analysis procedure

As described in Chapter 4, the time of flight of the ion of interest from the precision Penning trap to the detector is recorded after the ion is subjected to an azimuthal quadrupolar excitation in the trap for a particular time duration. The frequency of the quadrupolar excitation is scanned around the expected cyclotron frequency of the trapped ion and for each excitation frequency, the time of flight of the ion is recorded. A typical plot for such a data set, often called the resonance plot, is shown in Fig. 4.7 along with the theoretically expected line-shape. The experimental data of the resonance are fitted with the theoretical line-shape using the ISOLTRAP evaluation program *Eva*. The fitting is performed by minimization of χ^2 using the Levenberg-Marquardt method [Press1992]. The cyclotron frequency of the investigated ion along with its uncertainty is obtained from the fit. The data analysis procedure is described below.

Z-class analysis

There are two ways to fit the experimental data-points with the theoretical line-shape. In the first case, the fit is performed considering all the investigated ions at a time. In the second case, ions recorded with different counts per cycle are grouped into a few equally populated groups or *classes* and each of the classes are treated individually for fitting. This class-wise analysis is often referred to as the *Z-class analysis* [Kellerbauer2003] and is performed when isobaric or isomeric contaminations are present along with the ion of interest in the Precision Penning Trap during measurement, which can considerably shift the resonance frequency of the ion of interest depending on the number of ions inside the trap [Bollen1992].

In the experiment, the number of ions x_j hitting the detector in each measurement cycle and the corresponding time-of-flight t_j are recorded against the frequency of quadrupolar excitation. Every time the detector records any ion(s), it is referred to as an *event*. Usually, the frequency of excitation is scanned from an initial value ν_i to a final value ν_f around the probable cyclotron frequency of the ion in equal steps and for each step, the x_j and t_j are recorded with respect to the excitation frequency ν_j. This is repeated until a statistically sufficient number of data is collected (usually about 3000 ion counts).

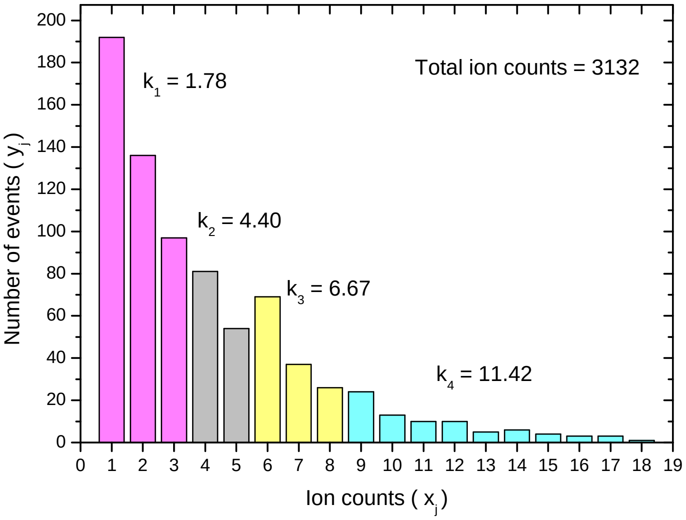

Figure 6.3: Histogram showing the number of events (y_j) with respect to the corresponding ion counts (x_j) for the resonance measurement of $^{76}\mathrm{Zn}^+$. Different colors represent different classes, and for each class, the average ion count (k) is shown.

Figure 6.3 shows the distribution of the number of events (y_j) with respect to the corresponding ion counts (x_j). For example, there were 81 events recording 4 ions each. This distribution can be divided into m sets or *classes* so that for each class, $\sum x_j y_j$ is (almost) equal.

The total number of events in a class will be $\sum y_j$, where the summation is over the class. The weight w_j for each ion count x_j in that class will be $w_j = y_j / \sum y_j$, where y_j is the number of events corresponding to the ion count x_j. Thus, in each class, the average ion count (*i.e.*, ion count per event) will be $k = \sum x_j w_j$.

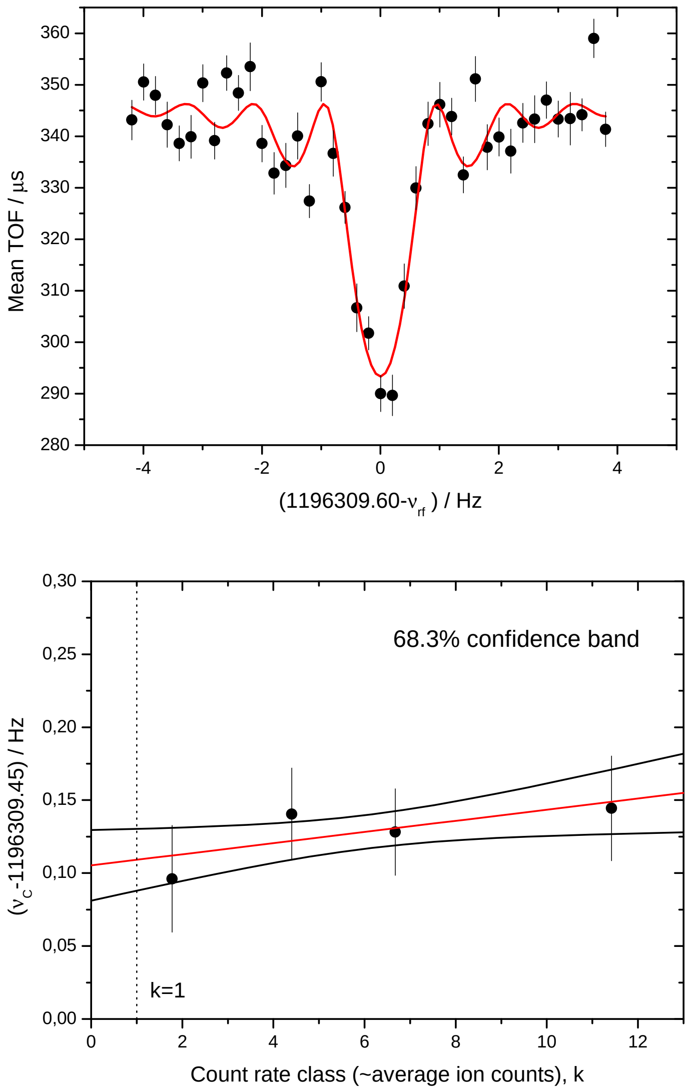

Figure 6.4: Top: A typical time-of-flight cyclotron resonance curve for ^{76}Zn$^+$. The solid line is a fit for the expected line-shape to the data points. The excitation time-duration for this resonance is 900 ms and the resolving power $(\nu/(\delta\nu)_{FWHM})$ obtained is $\approx 1.0 \times 10^6$. Bottom: Count-rate class analysis for the ^{76}Zn$^+$ resonance spectrum with 4 ion classes. The center frequency obtained from each class is fitted linearly against the ion classes (average ion counts). The average center frequency is determined by extrapolating the linear fit to the average ion count unity and the corresponding uncertainty is calculated from the 1σ confidence band of the linear fit.

For each class, the cyclotron frequency ν_c is determined by fitting the TOF vs. excitation frequency data corresponding to that class with the theoretical line-shape. Plotting ν_c with respect to k for each of the classes, one would expect a straight line with zero slope for ideal conditions. But due to the effects of contaminations, for the higher values of k, ν_c can be shifted [Bollen1992].

A linear least-squares fit is then applied to the data points with a 68.3% confidence band corresponding to the 1σ standard deviation of the normal distribution (See Appendix A). Assuming the detection efficiency of the Channeltron detector to be almost 100%, the cyclotron frequency for a single ion is determined by extrapolating the linear fit to the average ion count unity.

Figure 6.4(bottom) shows a count-rate class analysis for the ^{76}Zn^{+} resonance spectrum with 4 ion classes. In case of these neutron-rich Zn isotopes, however, the level of contamination is very low (mostly Ga isotopes) and a shift of the cyclotron frequency has not been observed in most of the cases.

6.3 Results and discussion

The mass of the neutron-rich zinc nuclides $^{71-81}$Zn were measured in a beam-time in October 2005 covering about one week. For all the nuclides, three or more resonances were recorded (see Appendix B), each with more than 3000 ion counts. For the nuclide ^{71}Zn, the mass of the first excited state was measured as it was more populated. An excitation time (T_{rf}) of 900 ms was used for most of the measurements.

The reference measurements were performed with ^{85}Rb delivered from the stable-ion source integrated to ISOLTRAP. The reference measurements were carried out before and after each measurement of the nuclide of interest to minimize the uncertainty resulting from the magnetic field fluctuations [Kellerbauer2003]. The time of excitation for all the reference measurements was 900 ms.

In order to check for the presence of any significant systematic effect due to unknown sources, mass of ^{87}Rb was measured with respect to ^{85}Rb. The measured mass value of ^{87}Rb was found to be 86.9091811(13) u, while the literature value is 86.909180527(13) u [Audi2003], indicating that the literature value is within the uncertainty of the measured value. Such measurements were carried out every 6 hours during the experiment.

Table 6.1 compiles the mass of the investigated nuclides expressed in the unified atomic mass unit and also the cyclotron frequency ratios between the reference and

Table 6.1: The cyclotron frequency ratios $r = \nu_c^{ref}/\nu_c$ of the reference nuclide (^{85}Rb) and the Zn nuclides, and the corresponding masses m of the Zn nuclides. The relative uncertainties of the nuclides are of the order of 10^{-8}. The half-lives $T_{1/2}$ of the nuclides range from 46.5 h down to 290 ms. T_{rf} here refers to the longest excitation time used for a particular nuclide.

Nucl.	$T_{1/2}$	T_{rf} (ms)	r	m (u)	$\delta m/m$
^{71m}Zn	3.96 h	1500	0.835311546(30)	70.9278887(26)	3.7×10^{-8}
^{72}Zn	46.5 h	900	0.847076232(27)	71.9268428(23)	3.2×10^{-8}
^{73}Zn	23.5 s	900	0.858885502(24)	72.9295825(20)	2.7×10^{-8}
^{74}Zn	95.6 s	900	0.870660440(31)	73.9294072(27)	3.7×10^{-8}
^{75}Zn	10.2 s	900	0.882477875(25)	74.9328402(21)	2.8×10^{-8}
^{76}Zn	5.7 s	900	0.894258121(23)	75.9331155(20)	2.6×10^{-8}
^{77}Zn	2.08 s	900	0.906079544(29)	76.9368872(24)	3.1×10^{-8}
^{78}Zn	1.47 s	900	0.917873056(35)	77.9382890(30)	3.9×10^{-8}
^{79}Zn	995 ms	900	0.929701243(49)	78.9426350(42)	5.3×10^{-8}
^{80}Zn	545 ms	600	0.941500837(35)	79.9445532(30)	3.8×10^{-8}
^{81}Zn	290 ms	400	0.953346729(63)	80.9504026(54)	6.7×10^{-8}

the investigated nuclides ($r = \nu_c^{ref}/\nu_c$). The mass uncertainty values include both the statistical and the systematic uncertainties. The systematic uncertainty of the setup has been estimated to be 8×10^{-9} [Kellerbauer2003], while the statistical uncertainty is a few times 10^{-8}. Therefore the total uncertainty is mainly determined by the statistical uncertainty. In the following, a brief treatment is given for each of the investigated nuclides in the light of their literature values.

6.3.1 Mass measurements on the n-rich Zn nuclides

^{71}Zn

The mass of ^{71}Zn, as reported in the AME 2003, was determined by using the ground state Q-value of the $^{70}Zn(d,p)^{71}Zn$ reaction measured at the Argonne National Laboratory by D. Von Ehrenstein *et al.* along with the mass of ^{70}Zn [Ehrenstein1967]. 85.9% isotopically enriched ^{70}Zn metal target with a thickness of about 0.5 mg/cm^2 was bombarded with a 10-MeV deuteron beam from the Argonne Tandem Van de

Graaff accelerator. For detection, refrigerated surface-barrier Si detectors of thickness 2000 micron with a typical resolution of about 50 keV were used, covering a solid angle of 10^{-3} sr. ^{71}Zn has a ground state with spin $\frac{1}{2}^-$ ($T_{1/2} = 2.45$ min), and a metastable state with spin $\frac{9}{2}^+$ ($T_{1/2} = 3.96$ h). Measurement of the ground state Q-value of the $^{70}Zn(d,p)^{71}Zn$ was first reported in this work.

At ISOLTRAP, the mass of the isomeric state ^{71m}Zn has been measured, from which the mass of ^{71}Zn is calculated using the excitation energy of ^{71m}Zn from [Audi2003]. The ISOLTRAP value of -67328.9 ± 2.8 keV is found to be in good agreement with the AME2003 value of -67327 ± 10 keV obtained from the above work as shown in Fig. 6.5.

^{72}Zn

The AME 2003 value for the mass of ^{72}Zn has been derived from the work of T. T. Thwaites on the investigation of the decay process of ^{72}Zn [Thwaites1963]. Samples prepared from thorium (Th) foil exposed to 22-MeV proton beam of the ORNL cyclotron for about 20 μA h and from tantalum (Ta) foil exposed to a 450-MeV proton beam of the Carnegie Institute of Technology synchrotron for about 3 μA h were used for the investigation. The first sample contained about 1 μC of ^{72}Zn and the second sample contained about 3 μC of ^{72}Zn. The radiation produced by the samples were studied using the standard scintillation counter technique. The work reports gamma rays corresponding to 3 isomeric states of ^{72}Ga at 51 ± 3, 143 ± 2 and 192 ± 4 keV as well as a β-ray group at 296 ± 6 keV from ^{72}Zn to ^{72}Ga. The β sources were prepared by evaporation of active material on Mylar films of thickness 0.00025 inch whereas the second sample mentioned above provided for the Zn source. Anthracene crystal of 16 % (^{137}Cs) resolution was used for taking the β-spectra. The Q-value for the β-decay reaction $^{72}Zn(\beta^-)^{72}Ga$ was derived from this work to be 458 ± 6 keV, which is used to determine the mass of ^{72}Zn in AME 2003.

The value of the mass-excess obtained from this work and adopted in AME2003 is -68131 ± 6 keV. At ISOLTRAP, the mass-excess value has been found to be -68145.5 ± 2.1 keV, which is about 2 standard-deviation away from the AME2003 value.

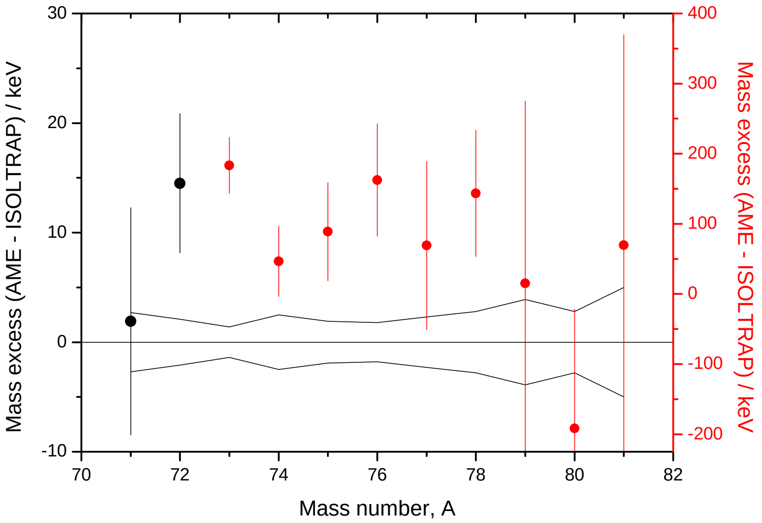

Figure 6.5: Comparison of the measured mass-excess values (ISOLTRAP) with the AME 2003 values [Audi2003]. The data-points and the lines in black correspond to the scale on the left, while the data-points in red correspond to the scale on the right. The line through $y = 0$ represents the ISOLTRAP values of the Zn nuclides from A=71 to 81. The uncertainties of the ISOLTRAP values are indicated by the band covering the $y = 0$ line.

^{73}Zn

Mass of ^{73}Zn was derived from the $^{76}Ge(^{14}C,^{17}O)^{73}Zn$ reaction reported by M. Bernas *et al.* in 1984 [Bernas1984]. A germanium target of thickness 130 $\mu g/cm^2$ was bombarded with a 72-MeV ^{14}C beam of 20 pnA from the Orsay MP Tandem. The target was then evaporated on a 30 $\mu g/cm^2$ backing of ^{12}C. A double-focusing spectrometer was used to analyze the emitted particles. Two resistive-wire position-sensitive proportional counters (PSPC) recorded the magnetic rigidity (momentum per unit charge) and the trajectory angles of the emitted particles. An ionization chamber was used to identify the particles.

The mass-excess value of ^{73}Zn adopted in AME 2003 from the above experiment was -65410 ± 40 keV. The value from the ISOLTRAP measurement has been found to be -65593.4 ± 1.4 keV, which is about 5 standard-deviation off the AME2003 value. A comparison of these mass-excess values with those predicted by 3 major mass models, namely, KTUY [Koura2005], HFB-14 [Goriely2007] and FRDM [Möller1995] are shown in Fig. 6.6. The uncertainty of the ISOLTRAP value is about 30 times smaller than that of the AME value, and the ISOLTRAP value is also closer to the mass-excess values predicted by the different mass models indicating its precision. The reason behind the discrepancy between the ISOLTRAP and the AME values has not yet been found.

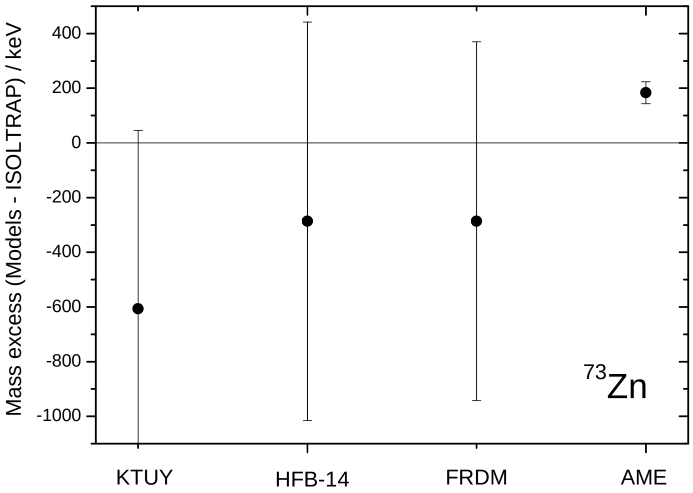

Figure 6.6: Mass-excess values of ^{73}Zn obtained from AME 2003 and different mass models in comparison to the ISOLTRAP value. The line through $y = 0$ represents the ISOLTRAP value. The uncertainty of the ISOLTRAP mass-excess (1.4 keV) is not visible in the plot.

^{74}Zn

The AME value for the mass of ^{74}Zn is due to two contributions, one by M. Bernas *et al.* [Bernas1984] and the other by R. Haupt *et al.* [Haupt1984] both published in 1984. In the first work the mass excess value of ^{74}Zn was derived to be -65620 ± 40 keV by using the reaction $^{76}Ge(^{14}C,^{16}O)^{74}Zn$ as described before in the case of ^{73}Zn. The work of R. Haupt *et al.* reports the calculation of the mass excess of ^{74}Zn from the Q-value of the reaction $^{76}Ge(^{18}O,^{20}Ne)^{74}Zn$ measured with the Q3D magnetic spectrograph at the MP-tandem. A 84-MeV ^{18}O beam was bombarded on a isotopically-enriched ^{76}Ge target of 73.9 % purity. The target was then evaporated on a ^{12}C foil. The products from the reaction were momentum-analysed with the Q3D magnetic spectrograph and afterwards detected by a $\Delta E - E$ counter. The mass excess from the Q-value of the reaction was determined to be -65735 ± 21 keV.

The mass-excess value adopted in the AME 2003 is −65710 ± 50 keV. The ISOLTRAP value −65756.7 ± 2.5 keV thus differs from the AME value by about 1 standard-deviation.

^{75}Zn

In the AME 2003, ^{75}Zn is connected to two nuclides- ^{76}Ge and ^{75}Ga in the *diagram of connections for input data* [Audi2003]. Ph. Dessagne reported the Q-value of the complex transfer reaction $^{76}Ge(^{14}C,^{15}O)^{75}Zn$ in 1984 [Dessagne1984]. A 72-MeV ^{14}C beam of 20 pnA from the Orsay MP tandem was bombarded on a target prepared by evaporation of isotopically-enriched ^{76}Ge foil. Two position-sensitive proportional counters were used for tracing the ion trajectories. The ion identification was done by a $\Delta E_1 - \Delta E_2 - E$ ionization chamber. The mass excess of ^{75}Zn calculated from the reaction was reported to be -62700 ± 150 keV.

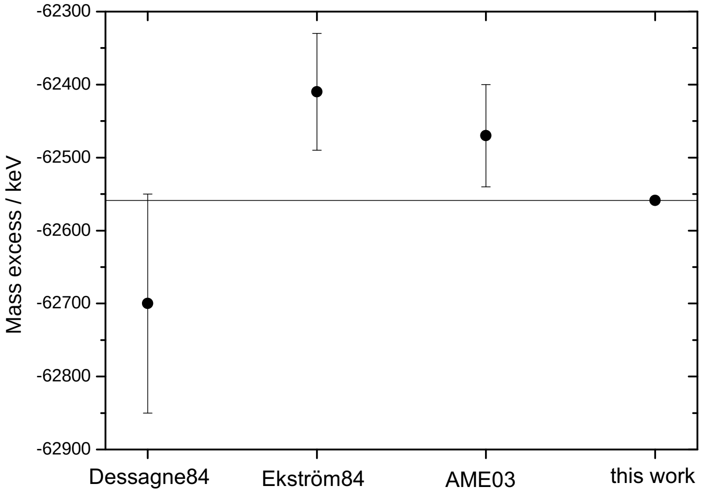

Figure 6.7: Comparison of the mass-excess values from previous measurements with the ISOLTRAP result for ^{75}Zn. The precision of the mass excess has been improved by a factor of 35 compared to the AME 2003 value.

The other work by B. Ekström *et al.* [Ekström1986] used the $^{75}Zn(\beta^-)^{75}Ga$ reaction. Isotope-separated fission products at the OSIRIS ISOL facility at Studsvik provided the ^{75}Zn isotopes. The isobaric beam was collected on a tape of Al-coated Mylar, after which the collected sample was transported to shielded chamber for measurements. The total β-decay energy was measured by means of $\beta\gamma$-coincidence measurement. A standard coaxial HPGe-detector with a 8 mm thick Al absorber to suppress β-particle counting was used for detection of the γ-rays and a planar HPGe detector was used for detection of the β-particles. This work reported the mass-excess value for ^{75}Zn to be -62410 ± 80 keV.

The adopted mass-excess value in the AME 2003 is -62470 ± 70 keV. At ISOLTRAP, the mass-excess for the nucleus has been determined to be -62558.9 ± 1.9 keV, which is within the 2 standard-deviation of the AME value.

^{76}Zn

The nuclide ^{76}Zn is linked to ^{76}Ga in the diagram of connections for input data of AME 2003. The mass of ^{76}Zn in the AME 2003 was derived from the work of B. Ekström *et al.* on the decay properties of neutron-rich Zn isotopes published in 1986 [Ekström1986]. The method has already been described in the case of ^{75}Zn. The work reported the Q-value of $^{76}Zn(\beta^-)^{76}Ga$ to be 4.16 ± 0.08 MeV. The mass-excess value adopted in the AME 2003 from this work is -62140 ± 80 keV. The ISOLTRAP value -62302.5 ± 1.8 keV is about 2 standard-deviation away from the AME 2003 value.

^{77}Zn

The mass value of ^{77}Zn in the AME 2003 has been derived from the work of B. Ekström *et al.* [Ekström1986] in which the Q-value of $^{77}Zn(\beta^-)^{77}Ga$ has been determined to be 7.27 ± 0.12 MeV. The AME 2003 value of mass-excess extracted from the above work is -58720 ± 120 keV. The ISOLTRAP value -58789.1 ± 2.3 keV is within the 1 standard-deviation of the AME value.

^{78}Zn

The mass of the nuclide ^{78}Zn in the AME was first reported by B. Ekström *et al.* based on the measurement of the β-decay Q-value of $^{78}Zn(\beta^-)^{78}Ga$ [Ekström1986]. The main procedure of the work has been described above. The data has been replaced by a later work of the same group [Audi2003]. The ISOLTRAP value -57483.4 ± 2.8 keV differs by about 1 standard-deviation from the adopted value of -57340 ± 90 keV in the AME 2003.

^{79}Zn

Mass of ^{79}Zn is determined not from purely experimental data but partly from a systematic trend [Audi2003, Stoitsov2006]. The work of B. Ekström *et al.* [Ekström1986] reports the Q-value of the β-decay of $^{79}Zn(\beta^-)^{79}Ga$ to be 8.55 ± 0.24 MeV. On the other hand, the systematic trend suggests a huge difference resulting in the adjustment of the Q-value to 9.09 ± 0.24 MeV. The adopted mass-excess value in AME 2003 -53420 ± 260 keV is in good agreement with the ISOLTRAP value of $-53435, 1 \pm 3.9$ keV.

^{80}Zn

The mass value of ^{80}Zn in the AME 2003 was contributed to by two experiments published in 1986. The mass was determined from the Q-value of the β-decay $^{80}Zn(\beta^-)^{80}Ga$ in both the experiments. The work of B. Ekström *et al.* [Ekström1986] reports a Q-value of 7.54 ± 0.20 MeV and the work of R. L. Gill *et al.* [Gill1986] reports 7.15 ± 0.15 MeV. The work of B. Ekström has been described earlier. The latter work was carried out at the mass separator TRISTAN at the high-flux reactor (HFBR) at Brookhaven National Laboratory. Thermal neutrons were impinged on a ^{235}U target located inside a plasma ion source at a high temperature. The fission products were mass-separated and implanted on a Al-coated Mylar tape. A hyper-pure Ge detector of thickness 10 mm with a 12 μm Ti window was used in order to measure the β-decay end point via $\beta - \gamma$ coincidence measurement. This work also reports the measurement of half-life for ^{80}Zn.

The mass-excess value adopted in the AME 2003 is -51840 ± 170 keV. The ISOLTRAP value -51648.3 ± 2.8 keV is slightly off the 1 standard-deviation of the AME value.

^{81}Zn

^{81}Zn is a secondary nuclide whose mass is determined only from the systematic trend in the AME 2003. Its mass excess has been derived to be -46130 ± 300 keV. The ISOLTRAP experiment has been the first to access this nuclide and perform a mass measurement. The mass-excess value -46199.6 ± 5.0 keV found from this measurement is within 1σ uncertainty of the AME value.

Table 6.2: Mass-excess values of the nuclides $^{71-81}$Zn from the final evaluation. The second column shows the final values of the mass excess ME$_{new}$ from the evaluation, and the third column shows literature values ME$_{AME}$ [Audi2003]. The difference between the new values and the literature values are shown in the fourth column.

Nuclides	ME$_{new}$ (keV)	ME$_{AME}$ (kev)	ME$_{new}$-ME$_{AME}$ (keV)
^{71}Zn	-67328.9(2.8)	-67327(10)	-2
^{72}Zn	-68145.5(2.1)	-68131(6)	-15
^{73}Zn	-65593.4(1.9)	-65410(40)	-183
^{74}Zn	-65756.7(2.5)	-65710(50)	-47
^{75}Zn	-62558.9(2.0)	-62470(70)	-89
^{76}Zn	-62302.5(1.9)	-62140(80)	-163
^{77}Zn	-58789.1(2.2)	-58720(120)	-69
^{78}Zn	-57483.5(2.8)	-57340(90)	-143
^{79}Zn	-53435.1(3.9)	-53420(260)	-15
^{80}Zn	-51648.3(2.8)	-51840(170)	192
^{81}Zn	-46199.7(5.0)	-46130(300)	-70

6.3.2 Final results of the evaluation

Usually, in the Atomic Mass Evaluation of a nuclide, results from all the previous measurements are taken into account along with the present data, and a least-squares adjustment is performed as explained in [Audi1986]. In the case of the Zn nuclides, the uncertainty of the previous measurements have been improved quite significantly with this work, and so the results from the ISOLTRAP measurements fully determine the final mass values from the evaluation.

The results are shown in Table 6.2 in terms of mass excess. The mass-excess values from the final evaluation are shown in the second column, and the corresponding literature values [Audi2003] are shown in the third column. The difference between the final results and the literature values are shown in the fourth column.

6.3.3 Discussion of the results

Comparison with mass models

For the region far from stability, experimental data is still very rare and one has to rely on theoretical models for mass values. So, it is important to compare the mass models with the available experimental data for their further improvement. For comparison with our experimental data, four leading nuclear mass models have been chosen: the Finite-Range Droplet Model (FRDM) [Möller1995], the Hartree-Fock Bogoliubov model (HFB-14) [Goriely2007], the Koura-Tachibana-Uno-Yamada (KTUY) model [Koura2005], and the Duflo and Zuker model [Duflo1995].

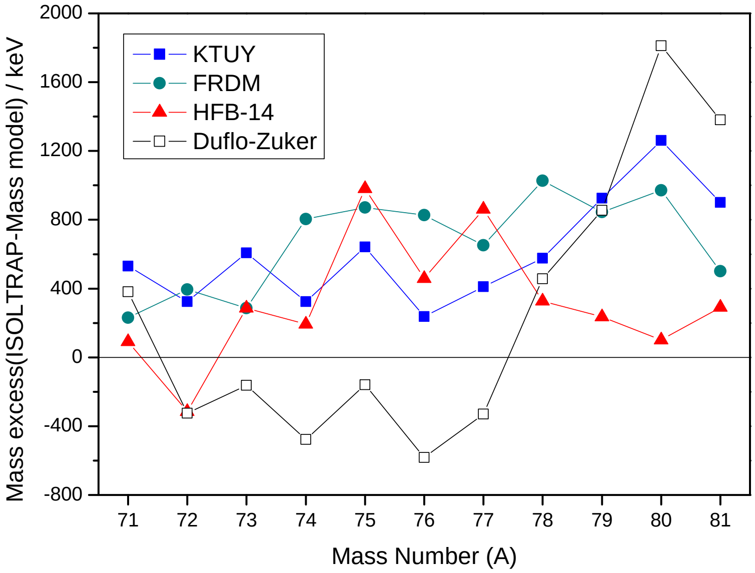

Figure 6.8: Comparison of the mass-excess values of $^{71-81}Zn$ nuclides measured at ISOLTRAP with those predicted by different mass models [Möller1995, Goriely2007, Koura2005, Duflo1995]. The line through $y = 0$ represent the ISOLTRAP values, while the different symbols represent the values predicted by the various models. The rms deviation is the least for the HFB-14 model and the highest for the Duflo-Zuker model in this range of nuclides.

The Finite-Range Droplet Model (FRDM) is composed of a macroscopic term based on the liquid-drop model and a microscopic term arising from the consideration of the single-particle Yukawa potential. The mass excess values from this model are in relatively good agreement with the experimental values as shown in Fig. 6.8.

The Hartree-Fock Bogoliubov model (HFB-14) is based on the effective two-body interaction between nucleons. The mass excess values from this model have the least rms deviation from the experimental values in the mass range under investigation.

The KTUY model consists of both macroscopic and microscopic terms. The macroscopic term represents nuclear masses as a smooth function of Z, N, and A based on the liquid-drop model. The microscopic part includes the intrinsic shell energy obtained by using spherical single-particle potentials and the average deformation energy of a deformed nucleus by treating the deformed nucleus as a superposition of spherical nuclei. The mass excess values from this model are in reasonably good agreement with the experimental values.

The Duflo and Zuker mass model assumes that there exists a pseudo-potential smooth enough to do Hartree-Fock calculations. The effective Hamiltonian is composed of two parts: a monopole part and a multipole part. The calculation with the monopole part is based on the single particle properties and is HF-type. The calculation with the multipole part acts as a residual interaction to the calculation with the monopole part, and it goes beyond HF. The mass excess values from this model agree with the experimental values in the lower neutron-number region. But as the neutron number increases, the predicted mass excess values differ significantly from the experimental values.

Neutron separation energies

The effect of the shell structure is best displayed through two-neutron separation energy (S_{2n}). The two-neutron separation energy is defined as

$$S_{2n}(N,Z) = B(N,Z) - B(N-2,Z), \tag{6.4}$$

where B represents the nuclear binding energy.

In general, the two-neutron separation energy decreases smoothly for a nuclide as a function of the neutron number, and the nuclear shell structure effects appear as abrupt changes in the slope. Figure 6.9 displays the two-neutron separation energies of the $^{71-81}Zn$ isotopes derived from their masses measured at ISOLTRAP along with those of the neutron-rich Ga, Ge and As isotopes as given in the literature [Audi2003]. The ISOLTRAP values of S_{2n} of the Zn isotopes are in good agreement with the literature values. For ^{79}Zn and ^{81}Zn, the literature values were derived from theoretical

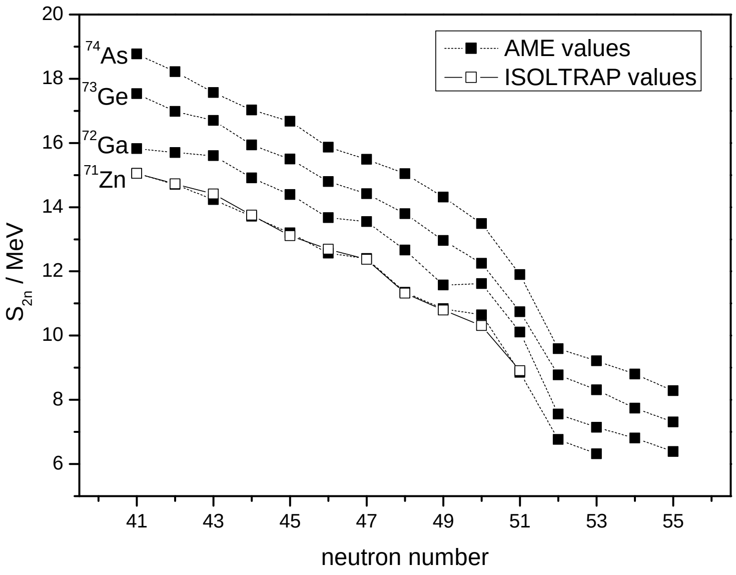

Figure 6.9: Comparison of the two-neutron separation energies S_{2n} of the Zn isotopes with the AME 2003 values. The shell-closure effect at N=50 can be seen clearly. The AME values of S_{2n} for the Ga, Ge and As isotopes are also shown.

calculations, and they have now been complimented by the ISOLTRAP values.

The nuclear shell-closure effect is clearly visible in Fig. 6.9. The steep decrease of S_{2n} at N=50 reflects the main shell closure at that neutron number.

Chapter 7

Conclusion and outlook

In this work the masses of the neutron-rich Zn nuclides with $A = 71 - 81$ have been measured. The mass of ^{81}Zn has been measured for the first time. The accuracy of the nuclides $^{71-80}$Zn have been increased considerably by the new measurements. The old mass values were derived mainly from the Q-value measurement of nuclear reactions and the Penning trap mass-measurement has been performed on them for the first time.

The immediate impact of the new mass values will be realized in the astrophysical r-process calculation. Since mainly the r-process is responsible for the production of the heavier elements in the universe, comparison of the abundance pattern calculated by the existing r-process theory with the experimental evidences may give rise to a fresh look at the r-process theory. The mass of the ^{80}Zn is particularly important since it is one of the crucial *waiting-point* nuclides of the r-process.

The possibility of further increasing the resolving power of the Penning trap mass-spectrometer has been investigated by simulating a new scheme of excitation for the determination of the ion cyclotron frequency. This *octupolar* excitation, in principle, is expected to increase the resolving power in the cyclotron frequency determination since the resonance between the ion motion and the excitation rf field occurs at $2\nu_c$, while in the case of the quadrupolar excitation, the resonance occurs at ν_c. In the numerical simulation done by use of IDL, although a resonance effect has been seen at $2\nu_c$, the pattern of the resonances has been observed to change considerably for even a slight change of one of the initial ion parameters indicating a non-linear effect of the ion motion. This limits the use of this excitation for ions which have a distribution of the initial position and velocity values. This excitation, however, can be fruitful in near future if the initial parameters of the trapped ions can be well-defined.

Appendix A

Calculation of confidence band for linear regression

For a given data set with n data-points, let us assume that each data-point $(x_i,\, y_i)$ has an error σ_i associated with y_i. In case of linear regression, the set of data-points are fitted to a straight line model:

$$y_i = a + bx_i + \epsilon_i, \tag{A.1}$$

where, ϵ_i is a random error term and each ϵ_i is assumed to come from a population that has a normal distribution with mean 0 and standard deviation σ_i such that if a measurement at x_i is repeated several times, then the values of ϵ_i would be normally distributed with mean 0 and standard deviation σ_i [Press1992, Wolberg2006].

The least squares estimators of a and b, denoted by $\widehat{a}$ and $\widehat{b}$, respectively, are obtained by minimizing

$$\chi^2 = \sum_{i=1}^{n} \left[\frac{y_i - (a + bx_i)}{\sigma_i} \right]^2 = \sum_{i=1}^{n} w_i \left[y_i - (a + bx_i) \right]^2, \tag{A.2}$$

where, n is the number of data-points and $w_i = 1/\sigma_i^2$ are the weights of the data-points. Using calculus, the estimators $\widehat{a}$ and $\widehat{b}$ can be derived as

$$\widehat{b} = \frac{\sum\limits_{i=1}^{n} w_i (x_i - \overline{x})(y_i - \overline{y})}{\sum\limits_{i=1}^{n} w_i (x_i - \overline{x})^2} \tag{A.3}$$

and

$$\widehat{a} = \overline{y} - \widehat{b}\overline{x} = \overline{y} - \left[\frac{\sum\limits_{i=1}^{n} w_i(x_i - \overline{x})(y_i - \overline{y})}{\sum\limits_{i=1}^{n} w_i(x_i - \overline{x})^2}\right]\overline{x}, \tag{A.4}$$

where,

$$\overline{x} = \sum_{i=1}^{n} w_i x_i / w_t,\ \overline{y} = \sum_{i=1}^{n} w_i y_i / w_t \text{ and } w_t = \sum_{i=1}^{n} w_i.$$

The mean of y at any specified value of x, denoted by $\mu_{y|x}$, is given by

$$\mu_{y|x} = a + bx. \tag{A.5}$$

The corresponding estimator $\widehat{\mu}_{y|x}$ is a normal random variable with mean $a + bx$, and its estimated variance can be expressed as [Baglivo2005]:

$$\sigma^2_{\widehat{\mu}_{y|x}} = s^2\left[\frac{1}{w_t} + \frac{(x - \overline{x})^2}{S_{xx}}\right], \tag{A.6}$$

where, s is the estimated standard deviation of the linear regression given by

$$s = \left[\frac{\sum\limits_{i=1}^{n} w_i\left[y_i - (a + bx_i)\right]^2}{\psi}\right]^{1/2}, \tag{A.7}$$

with $\psi = n - 2$, the degrees of freedom, and

$$S_{xx} = \sum_{i=1}^{n} w_i(x_i - \overline{x})^2. \tag{A.8}$$

Let us construct a ratio z as

$$z = \frac{\widehat{\mu}_{y|x} - \mu}{\sigma_{\widehat{\mu}_{y|x}}} = \frac{\widehat{\mu}_{y|x} - \mu}{s\left[\frac{1}{w_t} + \frac{(x-\overline{x})^2}{S_{xx}}\right]^{1/2}} = \frac{\widehat{\mu}_{y|x} - \mu}{sR}, \tag{A.9}$$

where,

$$R = \left[\frac{1}{w_t} + \frac{(x - \overline{x})^2}{S_{xx}} \right]^{1/2} , \tag{A.10}$$

and μ is the population mean at a specified x whose estimate is $\widehat{\mu}_{y|x}$ from the linear regression.

The ratio z follows a distribution called the Student t distribution or simply the t distribution [Baglivo2005]. The t distribution is similar to the normal distribution in the sense that it is symmetric and bell-shaped, but it has fatter tails than the normal distribution as shown in Fig. A.1. With the degrees of freedom ψ approaching ∞, the t distribution approaches the normal distribution.

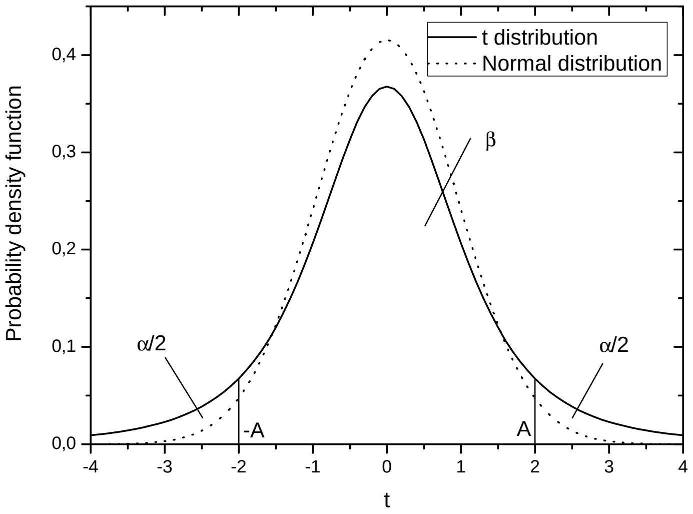

Figure A.1: Probability density curve of the t distribution for the degrees of freedom $\psi = 3$. For higher values of ψ, the t distribution approaches the normal distribution. The area β under the curve of the t distribution enclosed by the lines at $t = -A$ and $t = A$ is the probability that t will lie in the interval $[-A, A]$.

The probability density function of the t distribution is given by

$$f(t) = \frac{\Gamma\left(\frac{\psi+1}{2}\right)}{\sqrt{\psi\pi}\,\Gamma\left(\frac{\psi}{2}\right)} \left(1 + \frac{t^2}{\psi}\right)^{-\left(\frac{\psi+1}{2}\right)} \quad , \quad (-\infty \leq t \geq \infty) \; ; \tag{A.11}$$

where, ψ is the degrees of freedom.

For a given value of ψ, it is possible to find an interval $(-A, A)$ from the distribution where the random variable t can lie with a probability β:

$$Pr\left(-A < t < A\right) = \beta. \tag{A.12}$$

The points $-A$ and A, as shown in Fig. A.1, correspond to the lower and the upper limits on t that covers an area β around $t = 0$, leaving an area $\alpha/2$ on both sides of the probability density curve so that

$$\beta + 2 \times \frac{\alpha}{2} = 1. \tag{A.13}$$

It is customary to denote A as $t_{(\alpha/2,\psi)}$, where $\beta = 1 - \alpha$ is the probability and ψ is the degrees of freedom. The value of $t_{(\alpha/2,\psi)}$ can be found from the distribution for a given set of α and ψ.

Since z, from Eq. (A.9), follows the t distribution, we can write

$$\begin{aligned} & Pr\left(-A < z < A\right) = \beta \\ & \Rightarrow Pr\left(-t_{(\alpha/2,\psi)} < \frac{\widehat{\mu}_{y|x} - \mu}{sR} < t_{(\alpha/2,\psi)}\right) = \beta \\ & \Rightarrow Pr\left(\widehat{\mu}_{y|x} - t_{(\alpha/2,\psi)} sR < \mu < \widehat{\mu}_{y|x} + t_{(\alpha/2,\psi)} sR\right) = \beta \\ & \Rightarrow Pr\left(a + bx - t_{(\alpha/2,\psi)} sR < \mu < a + bx + t_{(\alpha/2,\psi)} sR\right) = \beta. \end{aligned} \tag{A.14}$$

Equation (A.14) represents that the probability of the population mean μ having a value in the interval $\left(a + bx - t_{(\alpha/2,\psi)} sR,\ \ a + bx + t_{(\alpha/2,\psi)} sR\right)$ is $\beta = 1 - \alpha$. This interval is referred to as the $(1 - \alpha) \times 100\%$ confidence interval for μ at a particular value of x.

The loci of the points $a + bx - t_{(\alpha/2,\psi)} sR$ and $a + bx + t_{(\alpha/2,\psi)} sR$ for all possible values of x of the linear regression constitute a band, called the $(1 - \alpha) \times 100\%$ confidence band of the linear regression. It is evident that the band is narrower when $x = \overline{x}$ and becomes wider as x deviates from $\overline{x}$.

Figure A.2 shows the 1σ ($\approx 68.3\%$) confidence band for the linear regression of a set of data-points (k_i, ν_c^i), where k_i is the average ion counts (count rate class) and ν_c^i is the corresponding cyclotron frequency. Considering the detector efficiency to be 100%, the cyclotron frequency ν_c for a single ion can be estimated by extrapolating the regression line to $k = 1$, and its uncertainty $\sigma(\nu_c)$ can be calculated from the corresponding confidence interval as shown in the figure.

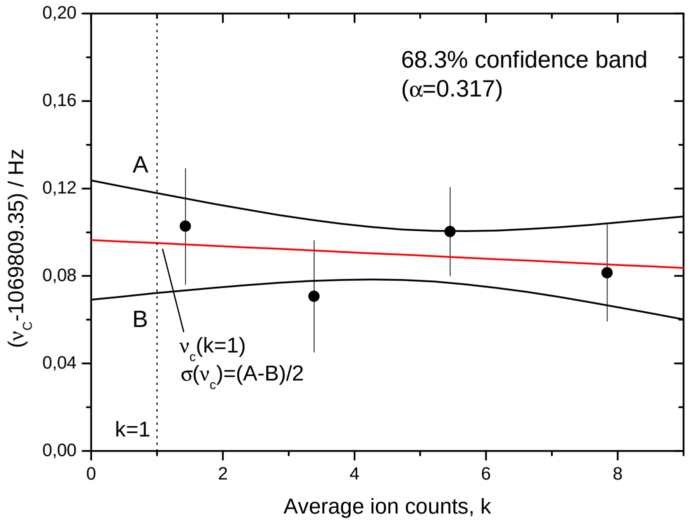

Figure A.2: 1σ confidence band for the linear regression of a set of cyclotron frequency (ν_c) vs. average ion counts (k) data for $^{85}\mathrm{Rb}^+$. The cyclotron frequency ν_c at $k = 1$ is found by extrapolating the regression line to $k = 1$. The uncertainty $\sigma(\nu_c)$ is obtained from the corresponding confidence interval.

Appendix B

Cyclotron resonances of the Zn nuclides (^{71}Zn to ^{81}Zn)

Cyclotron resonances of singly-ionized $^{71-81}$Zn nuclides have been presented along with their fits. The RF excitation times for recording the resonances ranged from 1.5 s down to 100 ms. About 3000 ion counts were detected for each cyclotron resonance. The reference measurements were performed with ^{85}Rb, and the time of excitation for all the reference measurements was 900 ms.

In case of ^{71}Zn, the mass of the first isomeric state, ^{71m}Zn, was measured as it was more populated. In all other cases, the ground-state masses were measured. The contamination of the ion beam delivered from ISOLDE was negligible for all the nuclides of interest.

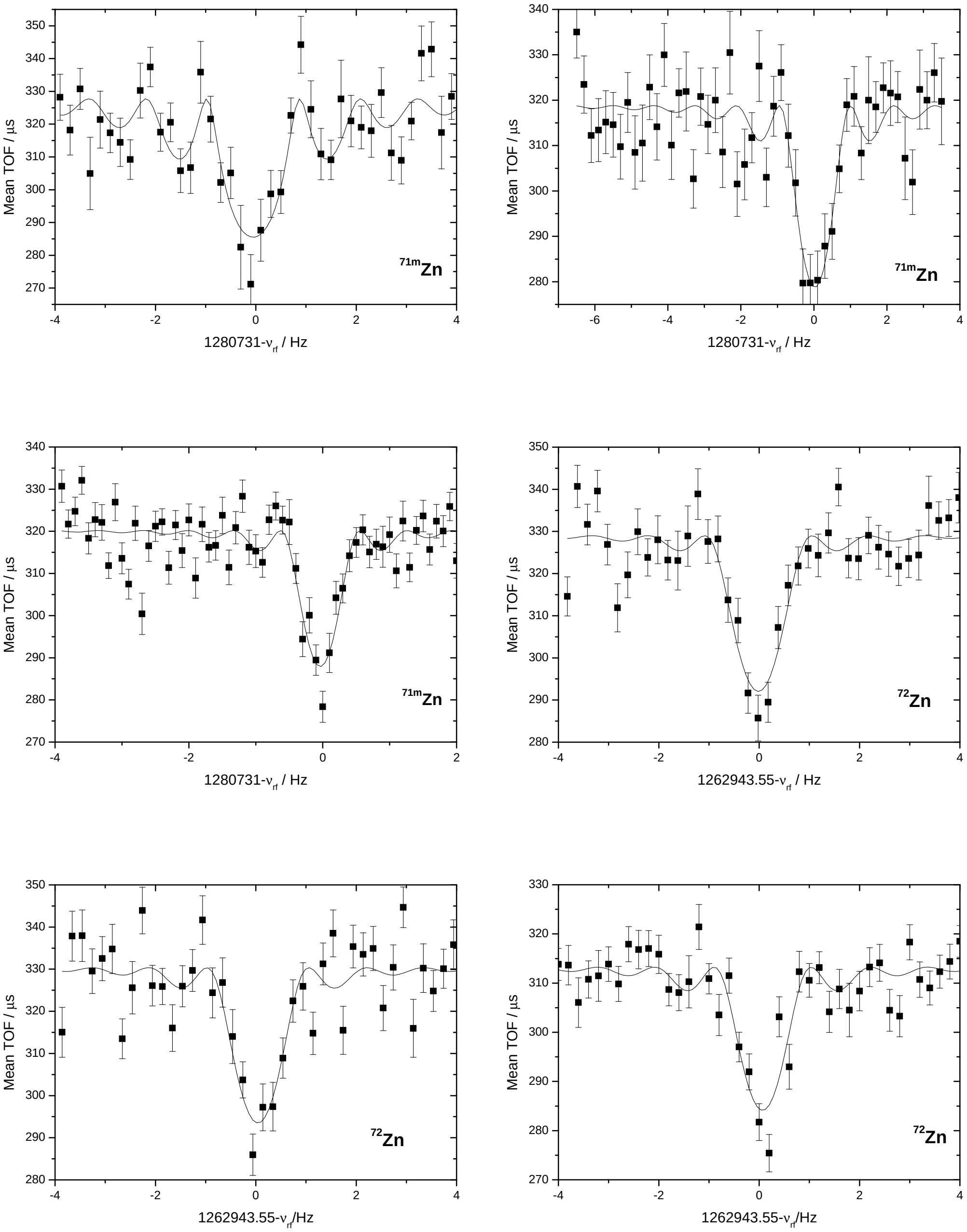

Figure B.1: Cyclotron resonances of ^{71}Zn and ^{72}Zn. Note that the resonances of ^{71}Zn are for its first isomeric state (^{71m}Zn).

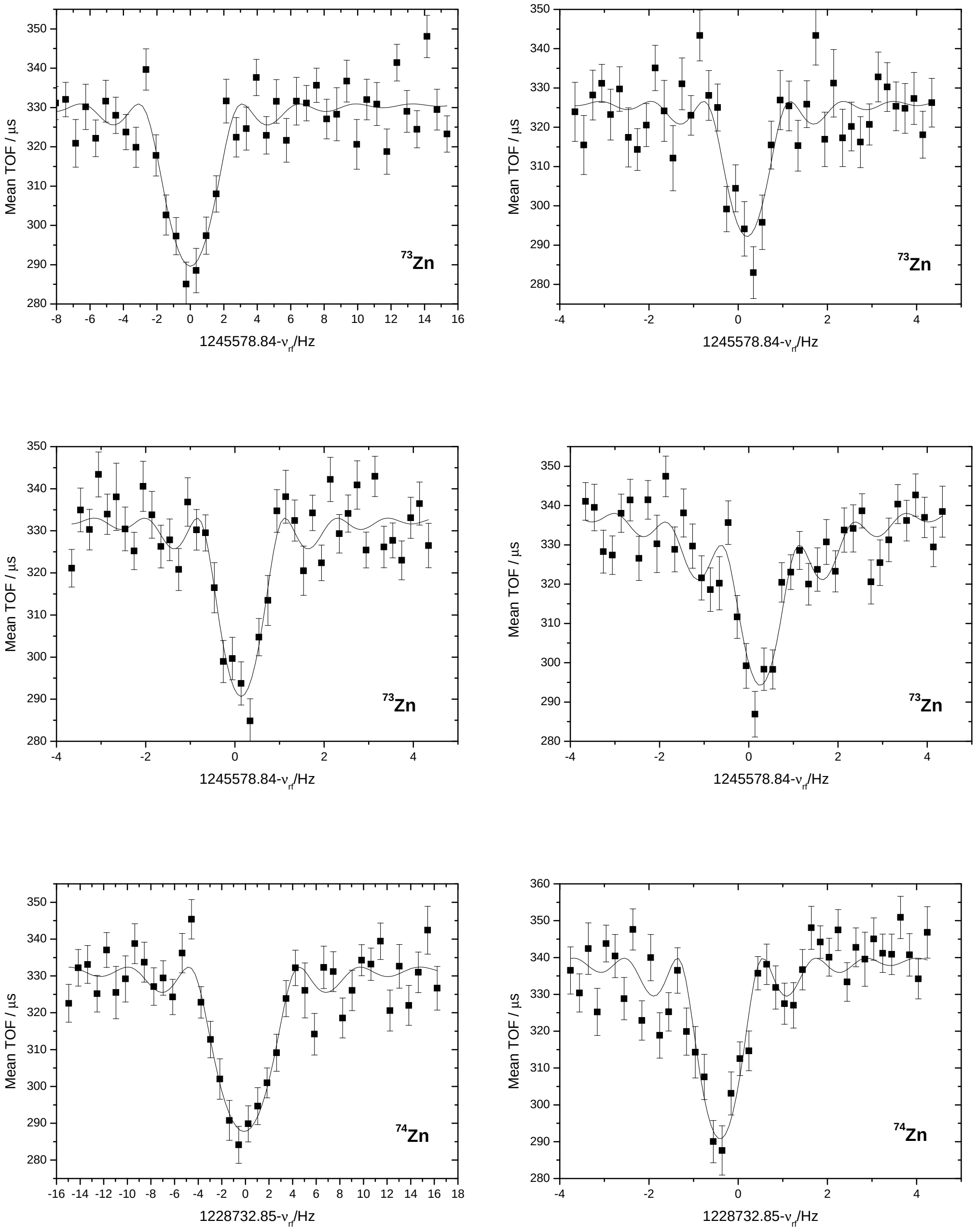

Figure B.2: Cyclotron resonances of ^{73}Zn and ^{74}Zn.

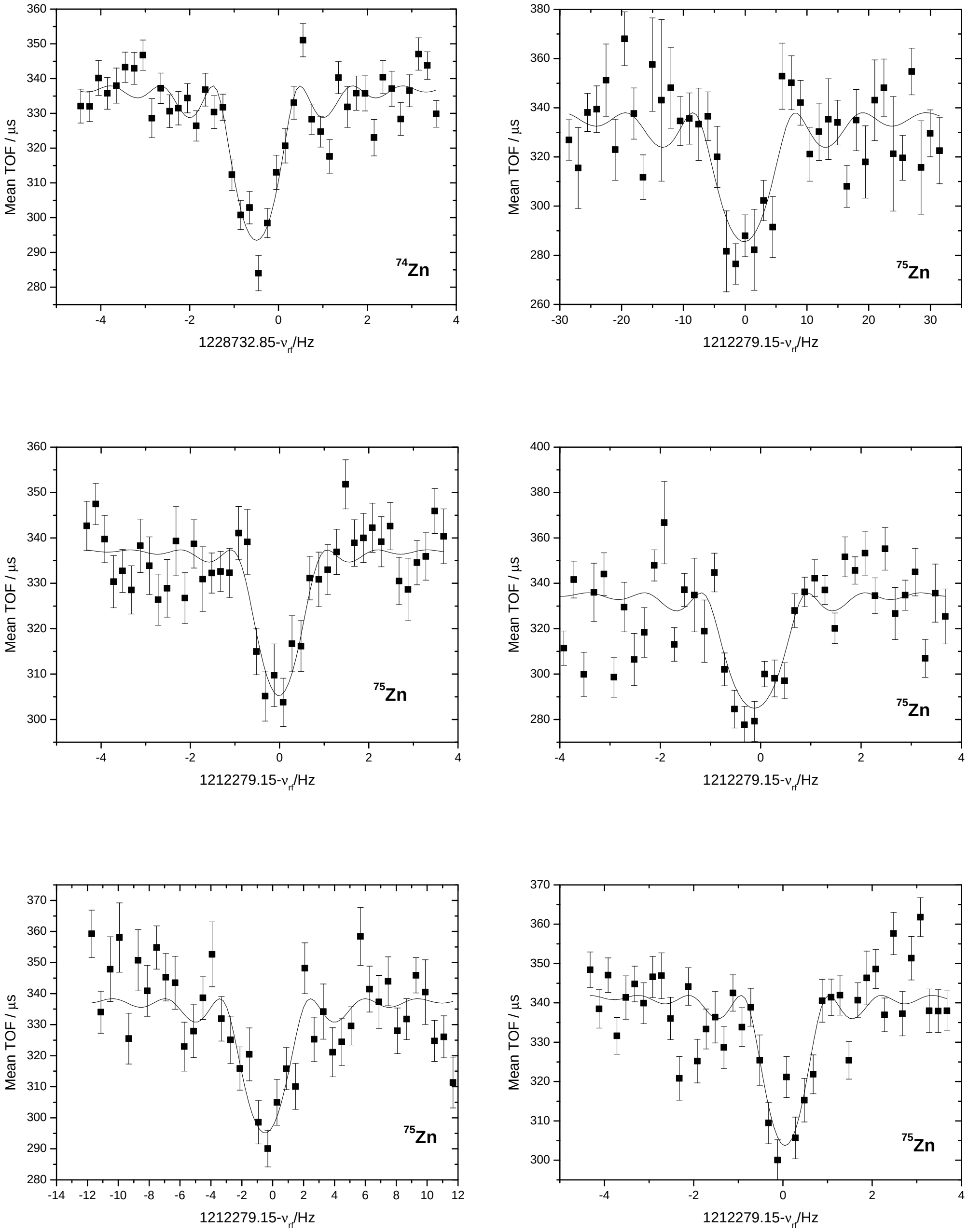

Figure B.3: Cyclotron resonances of ^{74}Zn (cont.) and ^{75}Zn.

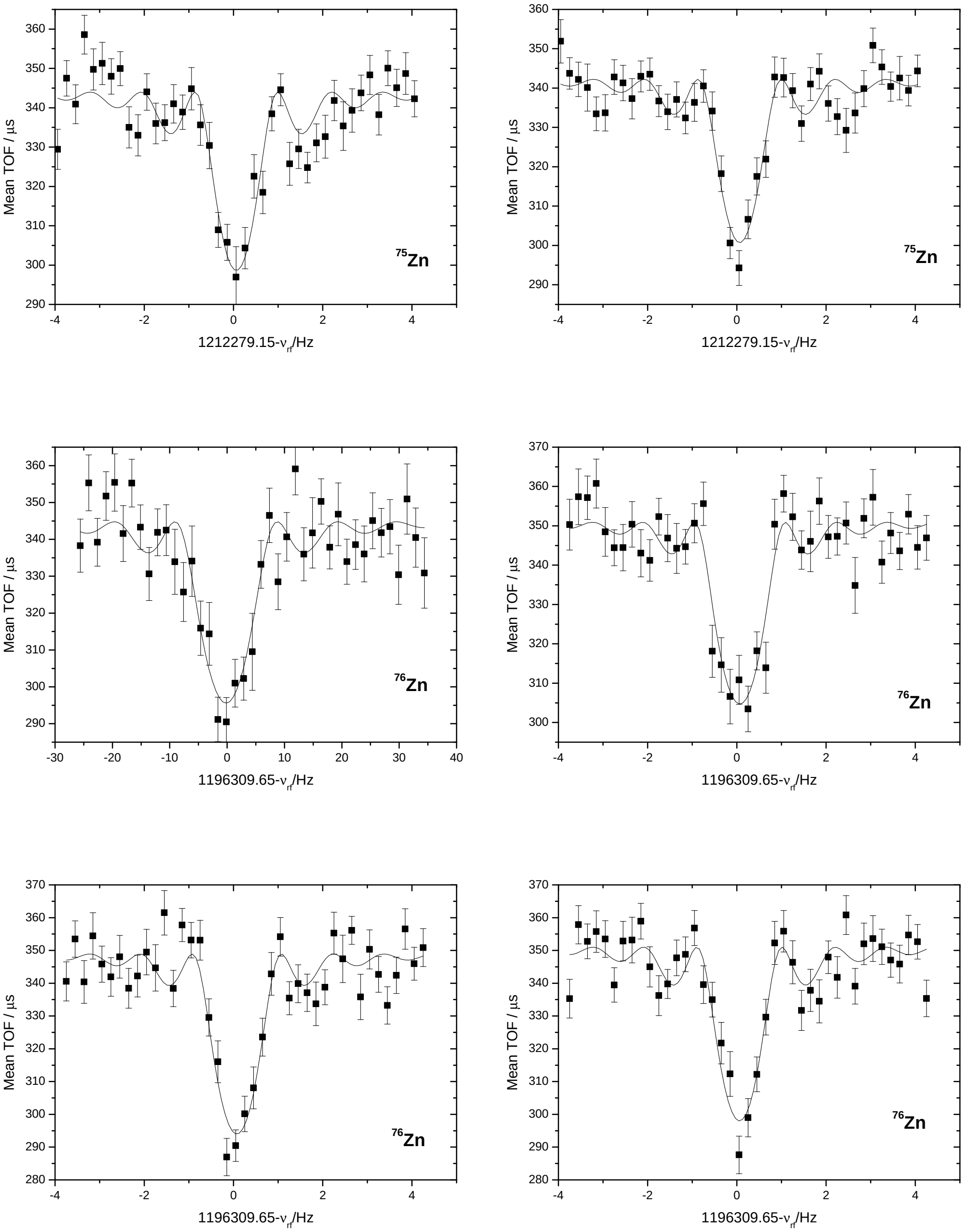

Figure B.4: Cyclotron resonances of ^{75}Zn (cont.) and ^{76}Zn.

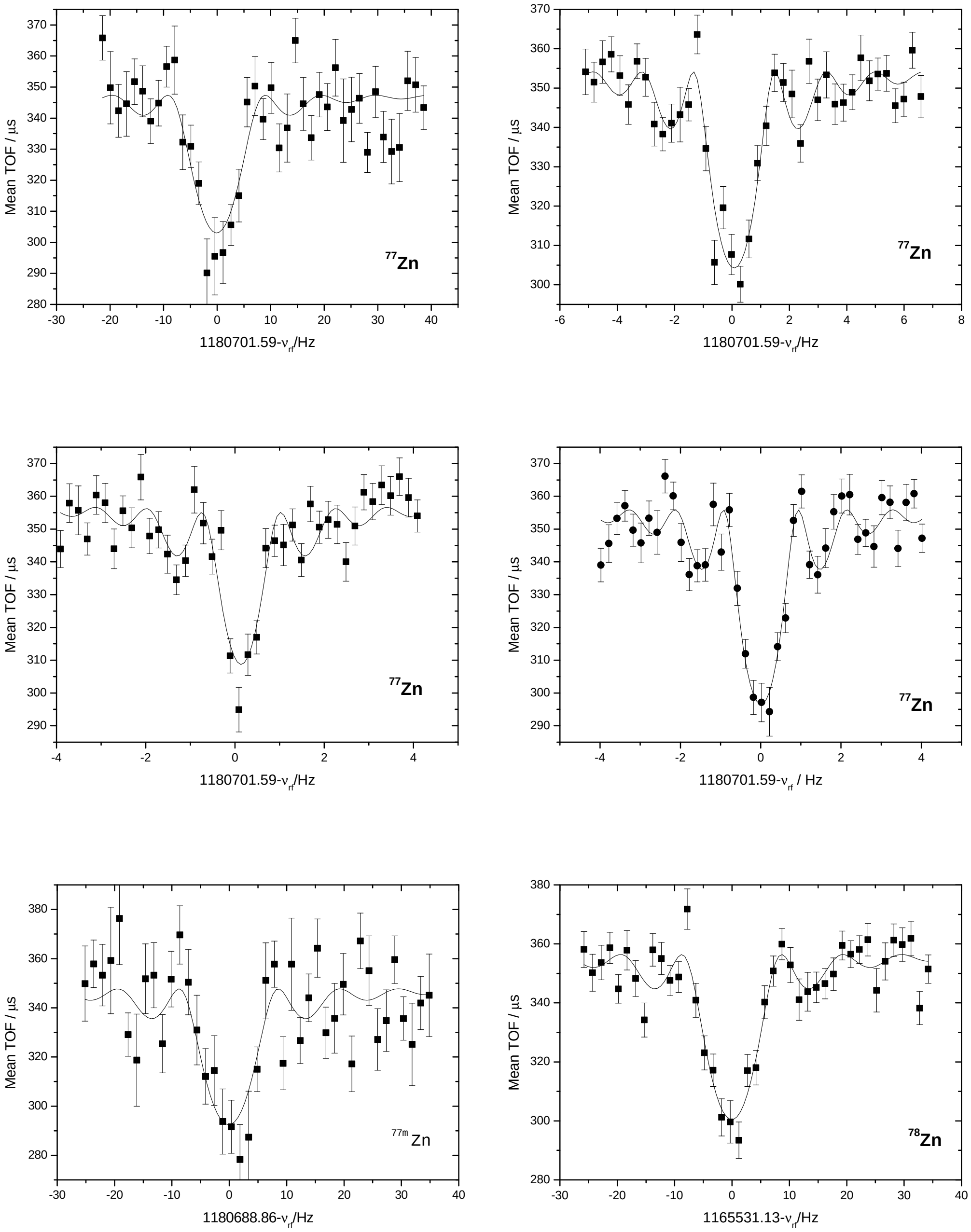

Figure B.5: Cyclotron resonances of ^{77}Zn and ^{78}Zn. Note the resonance of the isomer ^{77m}Zn.

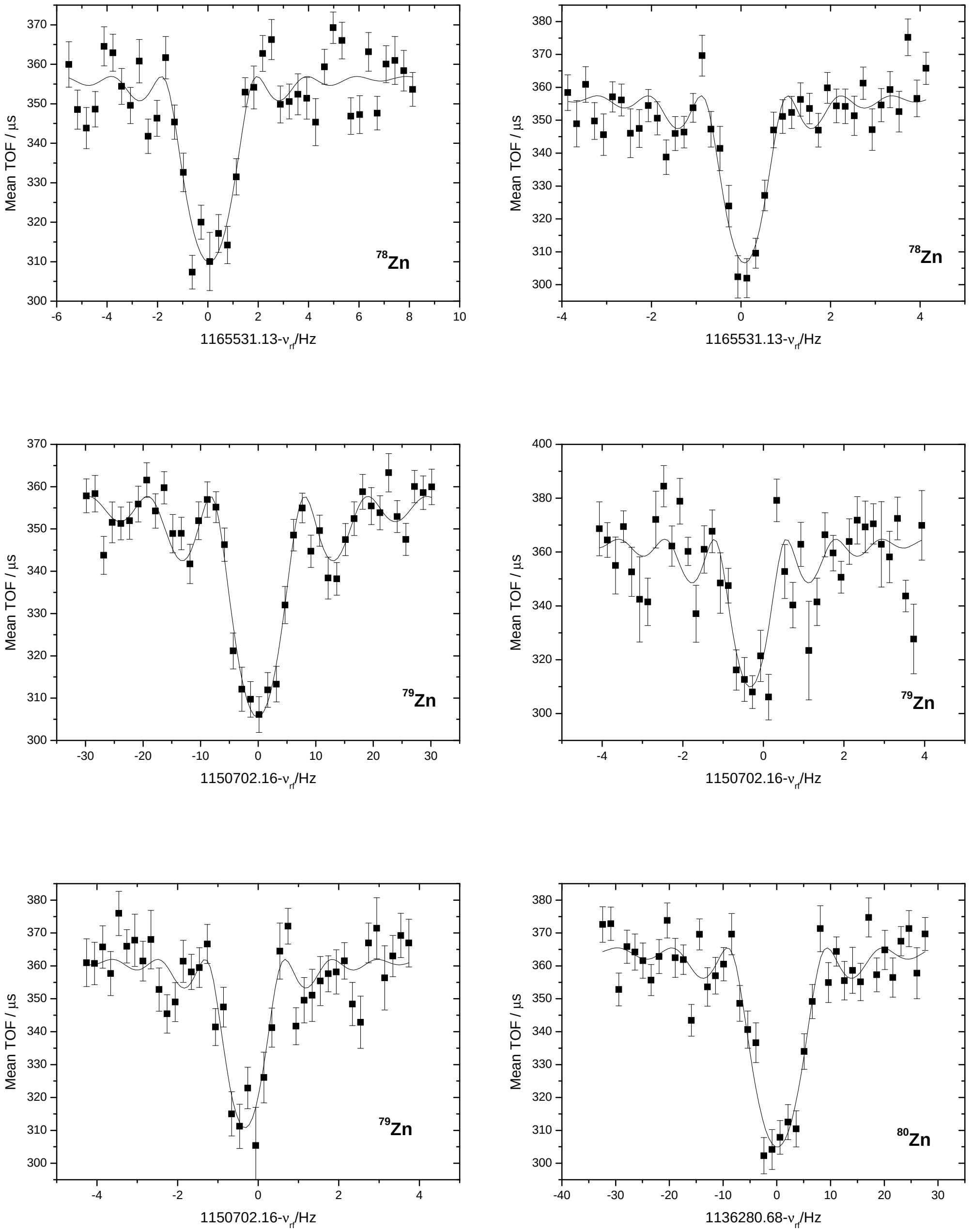

Figure B.6: Cyclotron resonances of ^{78}Zn (cont.), ^{79}Zn and ^{80}Zn.

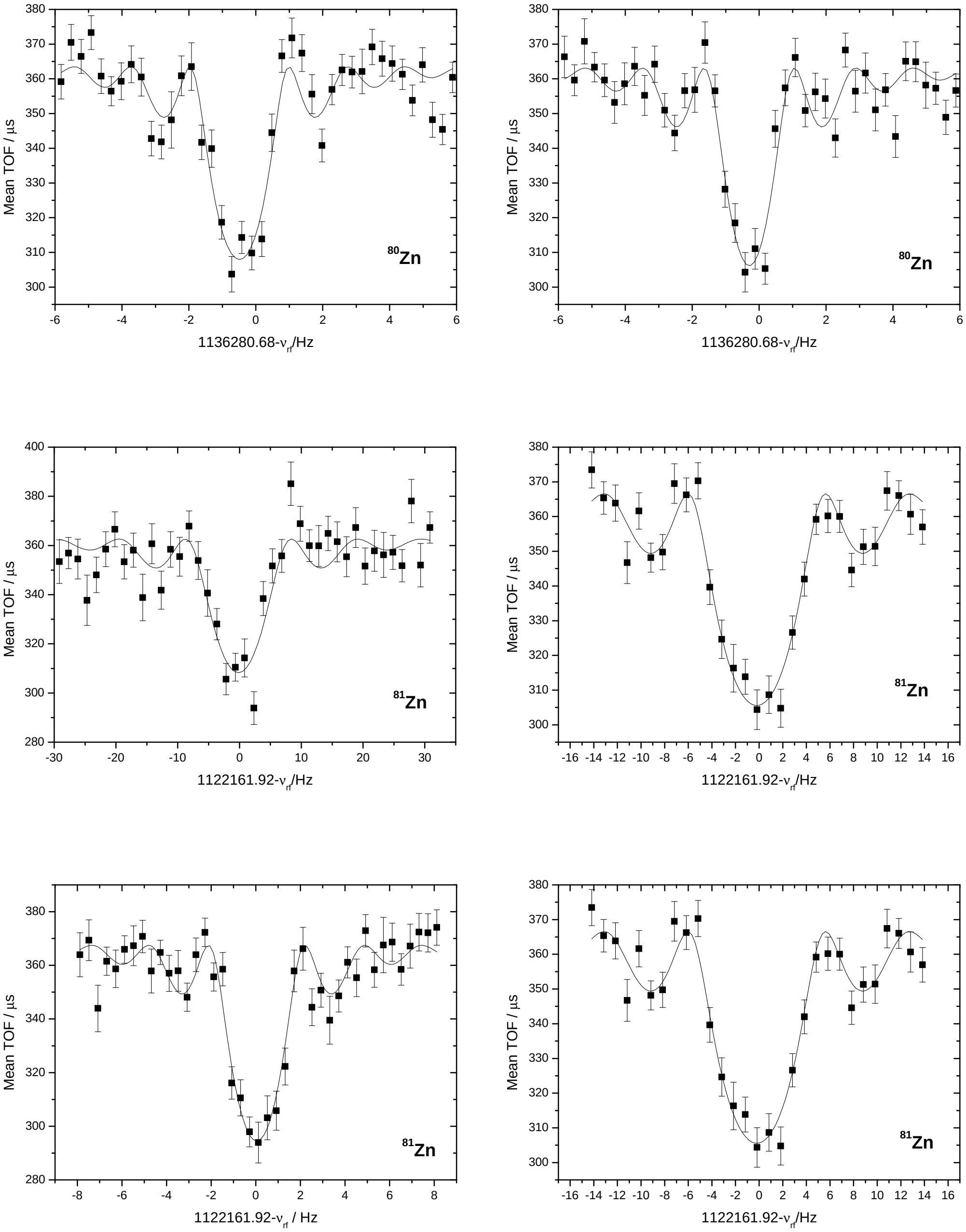

Figure B.7: Cyclotron resonances of ^{80}Zn (cont.) and ^{81}Zn.

Bibliography

[Ames1999] F. Ames, G. Audi, D. Beck, G. Bollen, M. de Saint Simon, R. Jertz, H.-J. Kluge, A. Kohl, M. König, D. Lunney, I. Martel, R.B. Moore, T. Otto, Z. Patyk, H. Raimbault-Hartmann, G. Rouleau, G. Savard, E. Schark, S. Schwarz, L. Schweikhard, H. Stolzenberg, J. Szerypo and The ISOLDE Collaboration. *High-accuracy mass determination of unstable cesium and barium isotopes*. Nucl. Phys. A **651**, 3 (1999).

[Anders1989] E. Anders and N. Grevesse. *Abundances of the elements: Meteoritic and solar*. Geochim. Cosmochim. Acta **53**, 197 (1989).

[Audi1986] G. Audi, W. G. Davies and G. E. Lee-Whiting. *A method of determining the relative importance of particular data on selected parameters in the least-squares analysis of experimental data*. Nucl. Instrum. Methods in Phys. Research A **249**, 443 (1986).

[Audi1993] G. Audi and A. H. Wapstra. *The 1993 Atomic Mass Evaluation*. Nucl. Phys. A **565**, 1 (1993).

[Audi1995] G. Audi and A. H. Wapstra. *The 1995 Update to the Atomic Mass Evaluation*. Nucl. Phys. A **595**, 409 (1995).

[Audi2003] G. Audi, A. H. Wapstra and C. Thibault. *The AME2003 Atomic Mass Evaluation (II): Tables, graphs and references*. Nucl. Phys. A **729**, 337 (2003).

[Baglivo2005] J. A. Baglivo. *Mathematica laboratories for mathematical statistics*. Publisher: SIAM, USA (2005).

[Basdevant2005] J.-L. Basdevant, J. Rich and M. Spiro. *Fundamentals in nuclear physics*. Publisher: Springer, Germany (2005).

[Benenson1979] W. Benenson and E. Kashy. *Isobaric quartets in nuclei.* Rev. Mod. Phys. **51**, 527 (1979).

[Bernas1984] M. Bernas, Ph. Dessagne, M. Langevin, J. Payet, F. Pougheon, P. Roussel, W. -D. Schmidt-Ott, P. Tidemand-Petersson and M. Girod. *Mass and excited levels of the neutron-rich nuclei* ^{73}Zn *and* ^{74}Zn *studied with the* $^{76}Ge(^{14}C,^{17}O)$ *and* $^{76}Ge(^{14}C,^{16}O)$ *reactions.* Nucl. Phys. **A413**, 363 (1984).

[Bernas2003] M. Bernas, P. Armbruster, J. Benlliure, A. Boudard, E. Casarejos, S. Czajkowski, T. Enqvist, R. Legraind, S. Leray, B. Mustapha, P. Napolitani, J. Pereira, F. Rejmund, M.-V. Ricciardi, K.-H. Schmidt, C. Stéphana, J. Taieb, L. Tassan-Got and C. Volant. *Fission-residues produced in the spallation reaction* $^{238}U + p$ *at 1 A GeV.* Nucl. Phys. A **725**, 213 (2003).

[Bianchi1989] L. Bianchi, B. Fernandez, J. Gastebois, A. Gillibert,W. Mittig, J. Barrette. *SPEG: An energy loss spectrometer for GANIL.* Nucl. Instr. and Meth. A **276**, 509 (1989).

[Blaum2002] K. Blaum, G. Bollen, F. Herfurth, A. Kellerbauer, H.-J. Kluge, M. Kuckein, E. Sauvan, C. Scheidenberger and L. Schweikhard. *Carbon clusters for absolute mass measurements at ISOLTRAP.* Eur. Phys. J. A **15**, 245 (2002).

[Blaum2003] K. Blaum, G. Bollen, F. Herfurth, A. Kellerbauer, H.-J. Kluge, M. Kuckein, S. Heinz, P. Schmidt and L Schweikhard. *Recent developments at ISOLTRAP: Towards a relative mass accuracy of exotic nuclei below* 10^{-8}. J. Phys. B **36**, 921 (2003).

[Blaum2006] K. Blaum. *High-accuracy mass spectrometry with stored ions.* Phys. Rep. **425**, 1 (2006).

[Bollen1990] G. Bollen, R. B. Moore, G. Savard and H. Stolzenberg. *The accuracy of heavy ion mass measurements using time of flight-ion cyclotron resonance in a Penning trap.* J. Appl. Phys. **68**, 4355 (1990).

[Bollen1992] G. Bollen, H.-J. Kluge, M. König, T. Otto, G. Savard, H. Stolzenberg, R. B. Moore, G. Rouleau, G. Audi and the ISOLDE Collaboration. *Resolution of nuclear ground and isomeric states by a Penning trap mass spectrometer.* Phys. Rev. C **46**, R2140–3 (1992).

[Bollen1996] G. Bollen, S. Becker, H.-J. Kluge, M. König, R. B. Moore, T. Otto, H. Raimbault-Hartmann, G. Savard, L. Schweikhard, H. Stolzenberg and the ISOLDE Collaboration. *ISOLTRAP: A tandem Penning trap system for accurate on-line mass determination of short-lived isotopes.* Nucl. Instrum. Methods A **368**, 675 (1996).

[Bollen2001] G. Bollen. *Mass measurements of short-lived nuclides with ion traps.* Nucl. Phys. A **693**, 3 (2001).

[Bollen2004] G. Bollen, S. Schwarz, D. Davies, P. Lofy, D. Morrissey, R. Ringle, P. Schury, T. Sun and L.Weissman. *Beam cooling at the low-energy-beam and ion-trap facility at NSCL/MSU.* Nucl. Instr. and Meth. A **532**, 203 (2004).

[Borge1987] M. J. G. Borge, P. Dessagne, G. T. Ewan, P. G. Hansen, A. Huck, B. Jonson, G. Klotz, A. Knipper, S. Mattsson, G. Nyman, C. Richard-Serre, K. Riisager, G. Walter and the ISOLDE Collaboration. *Study of the giant Gamow-Teller resonance in nuclear beta decay: The case of* ^{33}Ar. Physica Scripta **36-2**, 218 (1987).

[Bouquelle1996] V. Bouquelle, N. Cerf, M. Arnould, T. Tachibana and S. Goriely. *Single and multi-event canonical r-process: Astrophysics and nuclear physics considerations.* Astron. Astrophys. **305**, 1005 (1996).

[Britz1998] J. Britz, A. Pape and M.S. Antony. *Coefficients of the isobaric mass equation and their correlations with various nuclear parameters.* At. Data Nucl. Data Tables **69**, 125 (1998).

[Brown1986] L. S. Brown and G. Gabrielse. *Geonium theory: Physics of a single electron or ion in a Penning trap.* Rev. Mod. Phys. **58(1)**, 233 (1986).

[Burbidge1957] E. M. Burbidge, G. R. Burbidge, W. A. Fowler and F. Hoyle. *Synthesis of the elements in stars.* Rev. Mod. Phys. **29**, 547 (1957).

[Cameron1957] A. G. W. Cameron. *Elemental and nuclidic abundances in the solar system.* Chalk River Report **41** (1957).

[Cameron1983] A. G. W. Cameron, J. J.Cowan and J. W. Truran. *The waiting point approximation in r-process calculations.* Astrophys. and Space Sc. **91-2**, 235 (1983).

[Catherall2003] R. Catherall, J. Lettry, S. Gilardoni, U. Köster and the ISOLDE Collaboration. *Radioactive ion beams produced by neutron-induced fission at ISOLDE.* Nucl. Instrum. Methods Phys. Res. B **204**, 235 (2003).

[Clark2005] Jason Allan Clark. *Investigating the astrophysical rp-process through atomic mass measurements.* PhD thesis, University of Manitoba (Canada), 2005.

[Clayton1968] D. D. Clayton. *Principles of stellar evolution and nucleosynthesis.* Publisher: McGraw-Hill, USA (1983).

[Cowan1983] J. J. Cowan, A. G. W. Cameron and J. W. Truran. *Explosive helium burning in supernovae - A source of r-process elements.* Astrophys. J. **265**, 429 (1983).

[Cowan1991] J. Cowan, Friedrich-Karl Thielemann and J. W. Truran. *The r-process and nucleochronology.* Phys. Rep. **208**, 267 (1991).

[Dawson1976] P.H. Dawson. *Quadrupole mass spectrometry.* Publisher: Elsevier, Netherlands (1976).

[Dessagne1984] Ph. Dessagne, M. Bernas, M. Langevin, G. C. Morrison, J. Payet, F. Pougheon and P. Roussal. *The complex transfer reaction* $(^{14}C,^{15}O)$ *on Ni, Zn and Ge targets: Existance and mass of* ^{69}Ni. Nucl. Phys. A **426**, 399 (1984).

[Dilling2003] J. Dilling, P. Bricault, M. Smith, H.-J. Kluge and TITAN Collaboration. *The proposed TITAN facility at ISAC for very precise mass measurements on highly charged short-lived isotopes.* Nucl. Instr. and Meth. B **204**, 492 (2003).

[Domon2006] B. Domon and R. Aebersold. *Mass spectrometry and protein analysis.* Science **312**, 212 (2006).

[Duflo1995] J. Duflo and A. P. Zuker. *Microscopic mass formulas.* Phys. Rev. C **52**, R23 (1995).

[Ehrenstein1967] D. von Ehrenstein and J. P. Schiffer. *Study of the (d,p) reactions on* $Zn^{64,66,68,70}$. Phys. Rev. **164(4)**, 1374 (1967).

[Ekström1986] B. Ekström, B. Fogelberg, P. Hoff, E. Lund and A. Sangariyavanish. *Decay properties of* $^{75-80}Zn$ *and* Q_{β}*-values of neutron-rich Zn and Ga isotopes.* Physica Scripta **34**, 614 (1986).

[Eliseev2007] S. Eliseev, M. Block, A. Chaudhuri, F. Herfurth, H.-J. Kluge, A. Martin, C. Rauth, G. Vorobjev *Octupolar excitation of ions stored in a Penning trap mass spectrometer—A study performed at SHIPTRAP*. Int. J. Mass Spectrom. **262**, 45 (2007).

[Erdal1972] B. R. Erdal, L. Westgaard, J. Zylicz and E. Roeckl. *New isotopes 73Zn and 74Zn*. Nucl. Phys. A **194**, 449 (1972).

[Farhan1995] A. R. Farhan. *Nuclear data sheets update for $A = 74$*. Nucl. Data Sheets **74(4)**, 529 (1995).

[Fedoseyev2000] V. N. Fedoseyev, G. Huber, U. Köster, J. Lettry, V. I. Mishin, H. Ravn, V. Sebastian and the ISOLDE Collaboration. *The ISOLDE laser ion source for exotic nuclei*. Hyp. Int. **127**, 409 (2000).

[Fewell1995] M. P. Fewell. *The atomic nuclide with the highest mean binding energy*. Am. J. Phys. **63-7**, 653 (1995).

[Freiburghaus1999] C. Freiburghaus, J.-F. Rembges, T. Rauscher, E. Kolbe, F.-K. Thielemann, K.-L. Kratz, B. Pfeiffer and J. J. Cowan. *The astrophysical r-process: A comparison of calculations following adiabatic expansion with classical calculations based on neutron densities and temperatures*. Astrophys. J. **516**, 381 (1999).

[Freund2003] R. J. Freund and W. J. Wilson. *Statistical methods*. Publisher: Academic Press, USA (2003).

[Gill1986] R. L. Gill, R. F. Casten, D. D. Warner, A. Piotrowski, H. Mach, J. C. Hill, F. K. Wohn, J. A. Winger and R. Moreh. *Half-life of ^{80}Zn: The first measurement for an r-process waiting-point nucleus*. Phys. Rev. Lett. **56(17)**, 1874 (1986).

[Goriely1992] S. Goriely and M. Arnould. *The r-process in the light of microscopic model for nuclear masses*. Astron. Astrophys. **262**, 73 (1992).

[Goriely2002] S. Goriely, M. Samyn, P.-H. Heenen, J. M. Pearson and F. Tondeur. *Hartree-Fock mass formulas and extrapolation to new mass data*. Phys. Rev. C **66**, 024326 (2002).

[Goriely2007] S. Goriely, M. Samyn and J. M. Pearson. *Further explorations of Skyrme-Hartree-Fock-Bogoliubov mass formulas VII: Simultaneous fits to masses and fission barriers*. Phys. Rev. C **75**, 064312 (2007).

[Gräff1980] G. Gräff, H. Kalinowsky and J. Traut. *A direct determination of the proton electron mass ratio.* Z. Phys. A **297**, 35 (1980).

[Hartmann1997] H. R. Hartmann, D. Beck, G. Bollen, M. König, H.-J. Kluge, E. Schark, J. Stein, S. Schwarz and J. Szerypo. *A cylindrical Penning trap for capture, mass selective cooling, and bunching of radioactive ion beams.* Nucl. Instrum. Methods B **126**, 382 (1997).

[Haupt1984] R. Haupt, C. -A. Wiedner, G. J. Wagner, K. Wannebo, T. S. Bhatia, H. Hafner, R. Maschuw, W. Saathoff and S. T. Thornton. *Mass excesses of* $^{60,62}Fe$*,* ^{68}Ni*,* ^{69}Cu*,* ^{74}Zn*,* $^{73,75}Ga$*.* Z. Phys. A **317**, 193 (1984).

[Henley1969] E.M. Henley and C.E. Lacy. *Simple model for corrections to the isobaric multiplet mass equation.* Phys. Rev. **184**, 1228 (1969).

[Herfurth2001] F. Herfurth, J. Dilling, A. Kellerbauer, G. Bollen, S. Henry, H.-J. Kluge, E. Lamour, D. Lunney, R. B. Moore, C. Scheidenberger, S. Schwarz, G. Sikler and J. Szerypo. *A linear radiofrequency ion trap for accumulation, bunching and emittance improvement of radioactive ion beams.* Nucl. Instrum. Methods A **469**, 254 (2001).

[Herfurth2002] F. Herfurth, A. Kellerbauer, F. Ames, G. Audi, D. Beck, K. Blaum, G. Bollen, O. Engels, H.-J. Kluge, D. Lunney, R. B. Moore, M. Oinonen, E. Sauvan, C. Scheidenberger, S. Schwarz, G. Sikler, C. Weber and the ISOLDE Collaboration. *Accurate mass measurements of very short-lived nuclei: Prerequisites for high-accuracy investigations of superallowed* β *Decays.* Eur. Phys. J. A **15**, 17 (2002).

[Herlert2006] A. Herlert, S. Baruah, K. Blaum, P. Delahaye, M. Dworschak, S. George, C. Guénaut, U. Hager, F. Herfurth, A. Kellerbauer, M. Marie-Jeanne, S. Schwarz, L. Schweikhard and C. Yazidjian. *Towards high-accuracy mass spectrometry of highly charged short-lived ions at ISOLTRAP.* Int. J. Mass Spectrom. **251**, 131 (2006).

[Iliadis2007] C. Iliadis. *Nuclear physics of stars.* Publisher: Wiley-VCH, Germany (2007).

[ISOLDE2008] ISOLDE Homepage *http://isolde.web.cern.ch/ISOLDE/.*

[Käppeler1989] F. Käppeler, H. Beer and K. Wisshak. *s-process nucleosynthesis - nuclear physics and the classical model.* Rep. Prog. Phys. **52**, 945 (1989).

[Kelic2006] A. Kelic and K.-H. Schmidt. *Assessment of saddle-point-mass predictions for astrophysical applications*. Phys. Lett. B **634**, 362 (2006).

[Kellerbauer2001] A. Kellerbauer, T. Kim, R. B. Moore and P. Varfalvy. *Buffer gas cooling of ion beams*. Nucl. Instrum. Methods A **469**, 276 (2001).

[Kellerbauer2002] A. Kellerbauer, F. Herfurth, E. Sauvan, K. Blaum, H.-J. Kluge, C. Scheidenberger, G. Bollen, M. Kuckein and L. Schweikhard. *Carbon cluster ions for a study of the accuracy of ISOLTRAP*. Hyp. Int. **146/147**, 307 (2003).

[Kellerbauer2003] A. Kellerbauer, K. Blaum, G. Bollen, F. Herfurth, H.-J. Kluge, M. Kuckein, E. Sauvan, C. Scheidenberger and L. Schweikhard. *From direct to absolute mass measurements: A study of the accuracy of ISOLTRAP*. Eur. Phys. J. D **22**, 53 (2003).

[Kolhinen2004] V.S. Kolhinen, S. Kopecky, T. Eronen, U. Hager, J. Hakala, J. Huikari, A. Jokinen, A. Nieminen, S. Rinta-Antila, J. Szerypo and J. Äystö. *JYFLTRAP: A cylindrical Penning trap for isobaric beam purification at IGISOL*. Nucl. Instr. and Meth. A **528**, 776 (2004).

[Koura2000] H. Koura, M. Uno, T. Tachibana and M. Yamada. *Nuclear mass formula with shell energies calculated by a new method*. Nucl. Phys. A **674**, 47 (2000).

[Koura2005] H. Koura, T. Tachibana, M. Uno and M. Yamada. *Nuclidic mass formula on a spherical basis with an improved even-odd term*. Progress of Theoretical Phys. **113-2**, 305 (2005).

[König1995] M. König, G. Bollen, H.-J. Kluge, T. Otto and J. Szerypo. *Quadrupole excitation of stored ion motion at the true cyclotron frequency*. Int. J. Mass Spectrom. Ion Processes. **142**, 95 (1995).

[Köster2002] U. Köster. *Intense radioactive-ion beams produced with the ISOL method*. Eur. Phys. J. A. **15**, 255 (2002).

[Köster2003] U. Köster and ISOLDE Collaborations *On-line yields obtained with the ISOLDE RILIS*. Nucl. Instrum. Meth. Phys. Res. B **204**, 347 (2003).

[Köster2005] U. Köster. *ISOLDE beams of neutron-rich zinc isotopes: Yields, release, decay spectroscopy*. AIP Proceedings- *Nuclear fission and fission-product spectroscopy*. Cadarache, France. **798**, 315 (2005).

[Kratz1986] K.-L. Kratz, H. Gabelmann, W. Hillebrandt, B. Pfeiffer, K. Schlösser and F.-K. Thielemann. *The Beta-decay half-life of* $^{130}_{48}Cd_{82}$ *and its importance for astrophysical r-process scenerios*. Z. Phys. A **325**, 489 (1986).

[Kratz1988] K.-L. Kratz, F.-K. Thielemann, W. Hillebrandt, P. Möller, V. Harms, A. Wöhr and J. W. Truran. *Constraints on r-process conditions from beta-decay properties far off stability and r-abundances*. J. Phys. G **14**, S331 (1988).

[Kratz1993] K.-L. Kratz, J.-P. Bitouzet, F.-K. Thielemann, P. Möller and B. Pfeiffer *Isotopic r-process abundances and nuclear structure far from stability: Implications for the r-process mechanism*. Astrophys. J. **403**, 216 (1993).

[Kratz1998] K. L. Kratz, B. Pfeiffer and F. K. Thielemann. *Nuclear-structure input to r-process calculations*. Nucl. Phys. A **630**, 352c (1998).

[Kratz1999] K.-L. Kratz, P. Moller, B. Pfeiffer and F.-K. Thielemann. *The astrophysical r-process*. Proceedings of the American Chemical Society Symposium- *Origin of elements in the solar system: Implications of post 1957 observations*. New Orleans, USA. 119 (1999).

[Kratz2004] K.-L. Kratz, B. Pfeiffer, J.J. Cowan and C. Sneden. *r-process chronometers*. New Astronomy Reviews **48**, 105 (2004).

[Kretzschmar1990] Martin Kretzschmar. *Single paricle motion in a Penning trap: Description in the classical canonical formalism*. Physica Scripta **46**, 544 (1990).

[Kugler2000] E. Kugler. *The ISOLDE facility*. Hyp. Int. **129**, 23 (2000).

[Lambert1992] D. L. Lambert. *The p-nuclei: Abundances and origins*. Astron. Astrophys. Rev. **3**, 201 (1992).

[Lang1999] K. R. Lang and J. DeWalt. *Astrophysical Formulae : Volume I*. Radiation, gas processes and high energy astrophysics. Publisher: Springer, Germany (1999).

[Lettry1997] J. Lettry, R. Catherall, P. Drumm, P. van Duppen, A.H.M. Evensen, G.J. Focker, A. Jokinen, O.C. Jonsson, E. Kugler, H.L. Ravn and the ISOLDE Collaboration. *Pulse shape of the ISOLDE radioactive ion beams*. Nucl. Instrum. Methods **B126**, 130 (1997).

[Lhersonneau1999] G. Lhersonneau, B. Pfeiffer and K.-L. Kratz. *About the reliability of extrapolation of nuclear structure data.* Proceedings of the American Chemical Society Symposium- *Origin of elements in the solar system: Implications of post 1957 observations.* New Orleans, USA. 111 (1999).

[Lunney2000] D. Lunney and G. Bollen. *Extending and refining the nuclear mass surface with ISOLTRAP and MISTRAL.* Hyp. Int. **129**, 249 (2000).

[Lunney2003] D. Lunney, J. M. Pearson and C. Thibault. *Recent trends in the determination of nuclear masses.* Rev. Mod. Phys. **75**, 1021 (2003).

[Mattauch1965] J. H. E. Mattauch, W. Thiele and A. H. Wapstra. *The 1995 update to the Atomic Mass Evaluation.* Nucl. Phys. **67**, 1 (1965).

[Meyer1994] B. S. Meyer. *The r-, s- and p-processes in nucleosynthesis.* Annu. Rev. Astron. Astrophys. **32**, 153 (1994).

[Mohr1991] P. J. Mohr and B. N. Taylor. *CODATA recommended values of the fundamental physical constants: 1998.* J. Phys. Chem. Ref. Data **28**, 1713 (1999).

[Möller1995] P. Möller, J. R. Nix, W. D. Myers and W. J. Swiatecki. *Nuclear ground-state masses and deformations.* At. Data Nucl. Data Tables **59**, 185 (1995).

[Mukherjee2008] M. Mukherjee, D. Beck, K. Blaum, G. Bollen, J. Dilling, S. George, F. Herfurth, A. Herlert, A. Kellerbauer, H.-J. Kluge, S. Schwarz, L. Schweikhard and C. Yazidjian. *ISOLTRAP: An on-line Penning trap for mass spectrometry on short-lived nuclides.* Eur. Phys. J. A **35**, 1 (2008).

[Norman1979] E. B. Norman and D. N. Schramm. *On the conditions required for the r-process.* Astrophys. J. **228**, 881 (1979).

[NuPECC1993] Report of the Nuclear Physics European Collaboration Committee (NuPECC). *European radioactive beam facilities.* Publisher: NuPECC (1993).

[Oberheide1997] J. Oberheide, P. Wilhelms and M. Zimmer. *New results on the absolute ion detection efficiency of a microchannel plate.* Meas. Sci. Technol. **8**, 351 (1997).

[Panov2005] I. V. Panov, E. Kolbe, B. Pfeiffer, T. Rauscher, K.-L. Kratz and F.-K. Thielemann. *Calculations of fission rates for r-process nucleosynthesis.* Nucl. Phys. A **747**, 633 (2005).

[Press1992] W. H. Press, B. P. Flannery, S. A. Teukolsky and W. T. Vetterling. *Numerical recipes in C: The art of scientific computing.* Publisher: Cambridge University Press, UK (1992).

[Qian2003] Y.-Z. Qian. *The origin of the heavy elements: Recent progress in the understanding of the r-process.* Prog. Part. Nucl. Phys. **50**, 153 (2003).

[Qian2005] Y.-Z. Qian. *Nuclear physics and astrophysics of the r-process.* Nucl. Phys. A **752**, 550c (2005).

[Radon2000] T. Radon, H. Geissel, G. Münzenberg, B. Franzke, Th. Kerscher, F. Nolden, Yu.N. Novikov, Z. Patyk, C. Scheidenberger, F. Attallah, K. Beckert, T. Beha, F. Bosch, H. Eickhoff, M. Falch,Y. Fujita, M. Hausmann, F. Herfurth, H. Irnich, H.C. Jung, O. Klepper, C. Kozhuharov, Yu.A. Litvinov, K.E.G. Löbner, F. Nickel, H. Reich, W. Schwab, B. Schlitt, M. Steck, K. Sümmerer, T. Winkler and H. Wollnik. *Schottky mass measurements of stored and cooled neutron-deficient projectile fragments in the element range of* $57 \leq Z \leq 84$. Nucl. Phys. A **677**, 75 (2000).

[Rainville2005] S. Rainville, J. K Thompson, E. G. Meyers, J. M. Brown, M. S. Dewey, E. G. Kessler Jr., R. D. Deslattes, H. G. Börner, M. Jentschel, P Mutti and D. E. Pritchard. *A direct test of* $E = mc^2$. Nature **438**, 1096 (2005).

[Ravn1994] H. L. Ravn, P. Bricault, G. Ciavola, P. Drumm, B. Fogelberg, E. Hagebo, M. Huyse, R. Kirchner, W. Mittig, A. Mueller, H. Nifenecker and E. Roeckl. *Comparison of radioactive ion-beam intensities produced by means of thick targets bombarded with neutrons, protons and heavy ions.* Nucl. Instrum. Methods Phys. Res. B **88**, 441 (1994).

[Ringle2007] R. Ringle, G. Bollen, P. Schury, S. Schwarz and T. Sun. *Octupolar excitation of ion motion in a Penning trap—A study performed at LEBIT.* Int. J. Mass Spectrom. **262**, 33 (2007).

[Savard1991] G. Savard, S. Becker, G. Bollen, H.-J. Kluge, R. B. Moore, T. Otto, L. Schweikhard, H. Stolenzenberg and U. Wiess. *A new cooling technique for heavy ions in a penning trap.* Phys. Lett. A, **158**, 247 (1991).

[Savard2001] G. Savard, R.C. Barber, C. Boudreau, F. Buchinger, J. Caggiano, J. Clark, J.E. Crawford, H. Fukutani, S. Gulick, J.C. Hardy, A. Heinz, J.K.P. Lee, R.B. Moore, K.S. Sharma, J. Schwartz, D. Seweryniak, G.D. Sprouse and J. Vaz. *The Canadian Penning Trap Spectrometer at Argonne.* Hyperfine Interactions, **132**, 221 (2001).

[Schatz1998] H. Schatz, A. Aprahamian, J. Görres, M. Wiescher, T. Rauscher, J. F. Rembges, F.-K. Thielemann, B. Pfeiffer, P. Möller, K.-L. Kratz, H. Herndld, B. A. Brown and H. Rebel. *rp-process nucleosynthesis at extreme temperature and density conditions.* Phys. Rep. **294**, 167 (1998).

[Schatz2001] H. Schatz, A. Aprahamian, V. Barnard, L. Bildsten, A. Cumming, M. Ouellette, T. Rauscher, F.-K. Thielemann and M. Wiescher. *End-point of the rp-process on accreting neutron stars.* Phys. Rev. Lett. **86**, 3471 (2001).

[Schramm1976] D. N. Schramm and E. B. Norman. *Proc. 3rd Int. Conf. on Nuclei far from Stability, Cargese, France.* CERN Report **76-13**, 570 (1976).

[Schweikhard1993] L. Schweikhard and A. J. Marshall. *Excitation modes for Fourier transform-ion cyclotron resonance mass spectrometry.* J. Am. Soc. Mass Spectrom. **4**, 433 (1993).

[Schweikhard2003] L. Schweikhard, K. Hansen, A. Herlert, G. Marx, and M. Vogel. *New approaches to stored cluster ions.* Eur. Phys. J. D **24**, 137 (2003).

[Schweikhard2006] L. Schweikhard and G. Bollen (Eds.). *Ultra-accurate mass spectrometry and related topics.* Int. J. Mass Spectrom. **251(2-3)**, 85 (2006).

[Seeger1965] P. A. Seeger, W. A. Fowler and D. D. Clayton. *Nucleosynthesis of heavy elements by neutron capture.* Astrophys. J. Suppl. **11**, 121 (1965).

[Seifert1994] H. L. Seifert, J. M. Wouters, D. J. Vieira, H. Wollnik, X. G. Zhou, X. L. Tu, Z. Yo Zhou and G. W. Butler. *Mass measurement of neutron-rich isotopes from* ^{51}Ca *to* ^{72}Ni. Z. Phys. A **349**, 25 (1994).

[Sneden2003] C. Sneden and J. Cowan. *Genesis of the heaviest elements in the milkyway galaxy.* Science **299**, 70 (2003).

[Stadlmann2004] J. Stadlmann, M. Hausmann, F. Attallah, K. Beckert, P. Beller, F. Bosch, H. Eickhoff, M. Falch, B. Franczak, B. Franzke, H. Geissel, Th. Kerscher, O. Klepper, H.-J. Kluge, C. Kozhuharov, Yu.A. Litvinov, K.E.G. Löbner, M. Matoš,

G. Münzenberg, N. Nankova, F. Nolden, Yu.N. Novikov, T. Ohtsubo, T. Radon, H. Schatz, C. Scheidenberger, M. Steck, H. Weick and H. Wollnik. *Direct mass measurement of bare short-lived* ^{44}V, ^{48}Mn, ^{41}Ti *and* ^{45}Cr *ions with isochronous mass spectrometry*. Phys. Lett. B **586**, 27 (2004).

[Stoitsov2006] M.V. Stoitsov, J. Dobaczewski, W. Nazarewicz and P. Borycki. *Large-scale self-consistent nuclear mass calculations*. Int. J. Mass Spectrom. **251(2-3)**, 243 (2006).

[Stolzenberg1990] H. Stolzenberg, St. Becker, G. Bollen, F. Kern, H.-J. Kluge, Th. Otto, G. Savard and L. Schweikhard. *Accurate mass determination of short-lived isotopes by a tandem Penning-trap mass spectrometer*. Phys. Rev. Lett. **65**, 3104 (1990).

[Suess1957] H. E. Suess and H. C. Urey. *Abundances of the elements*. Rev. Mod. Phys. **28-1**, 53 (1956).

[Thielemann1983] F.-K. Thielemann, J. Metzinger and H.V. Klapdor. *Beta-delayed fission and neutron emission: Consequences for the astrophysical r-process and the age of the Galaxy*. Z. Phys. A **309**, 301 (1983).

[Thwaites1963] T. T. Thwaites. *Radioactive decay of* Zn^{72}. Phys. Rev. **129(4)**, 1778 (1963).

[Wallace1981] R. K. Wallace and S. E. Woosley. *Explosive hydrogen burning*. Astrophys. J. Suppl. **45**, 389 (1981).

[Wapstra1977] A. H. Wapstra and K. Bos. *The 1977 Atomic Mass Evaluation*. At. Data Nucl. Data Tables **19**, 175 (1977).

[Winger1987] J. A. Winger, J. C. Hill, F. K. Wohn, R. Moreh, R. L. Gill, R. F. Casten, D. D.Warner, A. Piotrowski and H. Mach. *Decay of* ^{80}Zn*: Implications for shell structure and r-process nucleosynthesis*. Phys. Rev. C, **36(2)**, 758 (1987).

[Wolberg2006] J. Wolberg. Data analysis using the method of least squares. Publisher: Springer, Germany (2006).

[Woosley1978] S. E. woosley and W. M. Howard *The p-process in supernovae*. Astrophys. J. Suppl. **36**, 285 (1978).

Curriculum Vitae

SUDARSHAN BARUAH

Contact Information

Institute for Physics
University of Greifswald
Felix-Hausdorff-Str. 6
17489 Greifswald, Germany

Phone: 0049-3834-8619756 (O)
Fax: 0049-3834-864701
E-mail: baruah@physik.uni-greifswald.de
http://www6.physik.uni-greifswald.de/ClusterTrap/shan

Research Interests

Precision mass-spectrometry, Atomic and nuclear physics

Education

Ernst Moritz Arndt University, Greifswald, Germany
Institute for Physics

Ph.D. Candidate (2003–present)

- Supervisor: Prof. Dr. Lutz Schweikhard

Indian Institute Of Technology Guwahati, India
Department of Physics

M.Sc., Physics (2000–2002)

- Specializations: Atomic and Nuclear Physics, Condensed matter Physics
- Master thesis: “Metal-insulator and ferromagnetic-paramegnetic transition in colossal magneto-resistance substance”
- Supervisor: Dr. S. Ravi
- Score: First Class

Cotton College, Guwahati, India
Department of Physics

B.Sc., Physics (1997–2000)

- Score: First Class

Computer Skills

- Statistical Packages: Origin, Mathematica
- Languages: C, IDL
- Applications: SIMION, CorelDraw, LaTeX, common Windows database, spreadsheet and presentation softwares

Honors and Awards

Merit Scholarship at Cotton College, Guwahati, India (1997–2000)
Merit Scholarship at Indian Institute of Technology Guwahati, India (2000–2002)

Personal details

Date of birth: February 1, 1980
Place of birth: Darrang, Assam, India
Marital status: Single

Others

Fellow of **International Max-Planck Research School**, Greifswald, Germany (2003–2006)
Member of the **German Physical Society** (Deutsche Physikalische Gesellschaft)

List of Publications

Publications

1. **Separated oscillatory fields in high-precision Penning trap mass spectrometry** *S. George, S. Baruah, B. Blank, K. Blaum, M. Breitenfeldt, U. Hager, F. Herfurth, A. Herlert, A. Kellerbauer, H.-J. Kluge, M. Kretzschmar, D. Lunney, R. Savreux, S. Schwarz, L. Schweikhard, C. Yazidjian*
Phys. Rev. Lett. 98, 162501 (2007)

2. **Towards high-accuracy mass spectrometry of highly charged short-lived ions at ISOLTRAP** *A. Herlert, S. Baruah, K. Blaum, P. Delahaye, M. Dworschak, S. George, C. Guénaut, U. Hager, F. Herfurth, A. Kellerbauer, M. Marie-Jeanne, S. Schwarz, L. Schweikhard, C. Yazidjian*
Int. J. Mass Spectrom. 251, 131-137 (2006)

3. **Spin-related aspects of mass determination of radionuclides** *A. Herlert, S. Baruah, K. Blaum, P. Delahaye, M. Dworschak, S. George, C. Guénaut, U. Hager, F. Herfurth, A. Kellerbauer, H.-J. Kluge, S. Schwarz, L. Schweikhard, C. Weber, C. Yazidjian*
Czech. J. Phys. 56, F287 (2006)

4. **High-precision mass measurements for reliable nuclear astrophysics calculations** *A. Herlert, S. Baruah, K. Blaum, M. Breitenfeldt, P. Delahaye, M. Dworschak, S. George, C. Guénaut, U. Hager, F. Herfurth, A. Kellerbauer, H.-J. Kluge, D. Lunney, M. Marie-Jeanne, R. Savreux, L. Schweikhard, C. Yazidjian*
International Symposium on Nuclear Astrophysics - Nuclei in the Cosmos - IX, CERN, Geneva, Switzerland 2006
Proceedings of Science, PoS(NIC-IX) 051 (2006)

5. **High-accuracy mass measurements on neutron deficient neon isotopes** *A. Herlert, S. Baruah, K. Blaum, P. Delahaye, S. George, C. Guénaut, F. Herfurth, H.-J. Kluge, D. Lunney, S. Schwarz, L. Schweikhard, C. Weber, C. Yazidjian*
FINUSTAR Conference, Kos, Greece 2005
AIP Conference Proceedings, 831, 152-156 (2006)

Talks

1. **Mass measurement of radioactive nuclei at ISOLTRAP, CERN**
International Max-Planck Research School on Bounded Plasmas: Graduate Colloquium (2003), Greifswald, Germany

2. **Simulation of ion motion in a Penning trap**
International Max-Planck Research School on Bounded Plasmas: Graduate Colloquium (2005), Greifswald, Germany

Posters

1. **Study of ion storage in a Paul trap**
S. Baruah, N. Walsh, M. Eritt, G. Marx, L. Schweikhard
General FANTOM and NIPNET/HITRAP/IONCATCHER Study Week on Trapping and Manipulating Atomic and Subatomic Particles 2003; Leuven, Belgium

2. **Simulations of a new excitation scheme for mass determination of exotic nuclides at ISOLTRAP**
S. Baruah, K. Blaum, A. Herlert, G. Marx, L. Schweikhard
Spring conference 2004, German Physical Society; Berlin, Germany

3. **Development of ion trapping techniques and application at ISOLTRAP/CERN**
S. Baruah, K. Blaum, A. Herlert, G. Marx, L. Schweikhard
Meeting 2004, International Max-Planck Research School on Bounded Plasmas; Greifswald, Germany

Acknowledgment

It is my pleasure to convey my gratitude to all those who have helped me in many different ways during my research work. First of all, I would like to thank Prof. Lutz Schweikhard for his supervision, advice and encouragement throughout my work. His guidance has enriched my growth as a student and a researcher. I gratefully acknowledge Prof. H.-Jürgen Kluge who arranged me the contacts to come to Germany. Many thanks goes to Dr. Alexander Herlert for his guidance and suggestions during my work. I am indebted to Dr. Klaus Blaum for his valuable suggestions from the very beginning of my work. Special thanks goes to Dr. Gerrit Marx for his help, suggestions and encouragement.

This work would not have been possible without the help of my colleagues of the ISOLTRAP team for which I am deeply indebted. The ISOLDE team needs a special mentioning for their grateful assistances during the beam-times.

Finally, I would like to express my gratitude to my colleagues and friends of the ClusterTrap group who have helped me in one way or another. I am thankful to Markus Eritt, Noelle Walsh, Ankur Chaudhuri, Martin Breitenfeldt and Franklin Martinez in particular for their help in various occasions and invaluable friendship.

Erklärung

Hiermit erkläre ich, daß diese Arbeit bisher von mir weder an der Mathematisch-Naturwissenschaftlichen Fakultät der Ernst-Moritz-Arndt-Universität Greifswald noch einer anderen wissenschaftlichen Einrichtung zum Zwecke der Promotion eingereicht wurde. Ferner erkläre ich, daß ich diese Arbeit selbständig verfaßt und keine anderen als die darin angegebenen Hilfsmittel benutzt habe.

Sudarshan Baruah